Dynamics of in-cloud turbulence and cloud-surface turbulent coupling in the Arctic Stratocumulus topped boundary layer

Rebecca Andreé Jansen

Submitted in accordance with the requirements for the degree of
Doctor of Philosophy

The University of Leeds
School of Earth and Environment

December 2018

The candidate confirms that the work submitted is her own, except where work which has formed part of jointly-authored publications has been included. The contribution of the candidate and the other authors to this work has been explicitly indicated below. The candidate confirms that appropriate credit has been given within the thesis where reference has been made to the work of others.

Work from this thesis has appeared in the publication Brooks et al. 2017 the work contributed by myself was that of the radiation modelling: The radiative heating data plotted in Figure 14a of the publication is my work and is featured in chapter 2 of this thesis.

Acknowledgements

Immeasurable thanks are given to my supervisor Prof Ian M Brooks who has been an invaluable source of wisdom, encouragement and support through this PhD. Thanks are also given to my co-supervisor Dr Stephen J Dobbie for his input into the LEM simulations and Dr Thomas Pleavin for the LEM setup and his guidance in installing and learning to run the model. Dr Alex Rap and Dr Cathryn Scott are thanked for their assistance in helping set up and run the Edwards-Slingo stand alone radiation code.

I would like to thank the National Environment Research Council (NERC) for funding this research project as part of the Aerosol cloud coupling and climate interactions in the Arctic (ACCACIA) project.

More personal thanks are due to my husband James Atkinson for his love, patience and support. To my mother and father Sue and Spencer for their help in enabling me to finish writing this thesis by looking after my newborn son while I typed. I would also like to thank my son Rufus for sleeping enough that I was able to get more work than expected done during the final few months of my PhD. Thank you as well to my awesome little brother Richard Jansen-Parkes for his help and hugs.

I would also like to acknowledge the medical and emotional help I received from Elaine Brown, Dr C Oldershaw and The Haldon Unit, without which I would not be here today to have completed this work.

Abstract

This thesis examined the behaviour of the cloud dynamics and mixed layer depth (MLD), the layer of turbulence mixed down into the boundary layer by in-cloud driven processes, in response to changes in the cloud's microphysical and turbulent structure, via both observational and model analysis.

The behaviour of the MLD was examined in observational data collected during the Arctic Summer Cloud Ocean Study (ASCOS) project's field campaign in late August 2008. The dissipation rate data enabled periods of decoupling between cloud and surface to be diagnosed and the MLD calculated. It was found that of all the cloud properties examined in the observational data available the MLD was most sensitive to variations in Liquid Water Path (LWP), most notably when the LWP <40 g m^{-2}. A LWP of 40 g m^{-2} being the point at which the cloud layers switch between grey- and black-body radiative states, pointing to the cause of the relationship being due to changes in the cloud layers adsorption and emission of LW radiation.

Radiation modelling using the Edwards-Slingo radiation code, in combination with the profiles of the gradient Richardson number, was conducted to examine the link between turbulent and radiative structure. The top third of the cloud layer during ASCOS, the portion above the base of the temperature inversion, was found to be non-turbulent even though LW cooling was occurring within the layer.

Idealised Large Eddy Model (LEM) runs were carried out based upon the ASOCS observations and the trend in LWP with MLD observed during ASCOS was seen in LEM simulations. Further LEM runs expanded upon the impact of cloud extending above the inversion on turbulence and cloud behaviour. The greater the extension of the cloud above the base of the temperature inversion, the weaker the cloud layer turbulence and shallower the MLD. LW cooling occurring within the inversion is found to primarily cause condensation rather than buoyancy driven turbulent motion, restricting LW cooling cloud driven turbulence.

Table of Contents

List of Tables

List of Figures

List of parameters

ε	Dissipation rate
ε_{min}	Dissipation rate threshold - 5×10^{-5} m^2 s^{-3}
A	Kolmogrov constant 0.5
g	Acceleration due to gravity
Ri	Richardson number
Ri_g	Gradient Richardson number
T	Temperature
T_{cb}	Cloud base temperature
T_{surf}	Surface temperature
u,v	Horizontal velocity
w	Vertical velocity
w_{max}	Maximum vertical velocity variance
$\overline{w'w'}$	Vertical velocity variance
z	Height
z_{ib}	Height of the base of the main temperature inversion
z_{LCL}	Height of the lifting condensation level
Γ_d	The dry Adiabatic lapse rate
Γ_m	The moist adiabatic lapse rate
θ	Potential temperature
θ_v	Virtual potential temperature

List of Abbreviations

AMPS	Arctic Mixed Phase Stratocumulus
ASCOS	Arctic Summer Cloud-Ocean Study
CCN	Cloud Condensation Nuclei
FRC	Fraction of Radiative Cooling
IN	Ice Nuclei
IPCC	International Panel on Climate Change
IWP	Ice Water Path
LCL	Lifting Condensation Level
LEM	Large Eddy Model
LW	Long Wave (radiation)
LWC	Liquid Water Content
LWP	Liquid Water Path
MetUM	Meteorological Office Unified Model
MLD	Cloud Mixed Layer Depth
MMCR	Millimetre Cloud Radar
MPACE	Mixed-Phase Arctic Cloud Experiment
NSIDC	National Snow and Ice Database Centre
SHEBA	Surface Heat Energy Budget of the Arctic
SML	Surface Mixed Layer
SW	Short Wave (radiation)
TKE	Turbulent Kinetic Energy
WBF	Wegener–Bergeron–Findeisen mechanism

Introduction

Climate is changing, with global mean temperatures rising. The Arctic is particularly sensitive to climate change, with the greatest observed and predicted temperature change of any latitude. In addition to having the greatest projected change in temperature of any region on earth, the changes predicted for the Arctic have the largest uncertainty.

Changing Arctic climate not only impacts the local environment, flora and fauna, but also those further afield. For example, locally increased sea ice melting due to warmer temperatures impacts the Polar Bear population as they rely on sea ice as a hunting platform, while further afield Arctic warming shifts surface pressure patterns resulting in changes to the mid-latitude storm tracks.

Cloud cover in the Arctic is extensive all year round, with decks of long-lived mixed-phase stratocumulus a persistent feature. This gives them a dominant role in the surface energy budget. The surface energy budget is the main regulator of processes such as sea ice melt and surface turbulence generation in the Arctic.

Due to the extensive and persistent nature of Arctic Stratocumulus, they are the source of the largest uncertainty in model predictions. It is essential that models accurately reproduce Arctic cloud cover and boundary layer structure. For example, simulations of the Arctic frequently fail to reproduce cloud free conditions and simulate cloud topped boundary layers that are too shallow, well mixed and too frequently coupled. The cloud and surface in the Arctic has been observed to be frequently decoupled (e.g. Sedlar et al., 2011), an atmospheric state that large scale model simulations (e.g. Tjernstrom et al., 2008 and Birch et al 2009) struggle to replicate. This thesis will focus on the expanding our knowledge of decoupled stratocumulus clouds in the Arctic as model simulations already replicate coupled conditions.

Work by Shupe et al., (2013) and Sotiropoulou et al., (2014) identify cloud mixing as the dominant influence over if the cloud and surface layers are coupled or decoupled, coupled being that mixing can occur between the

surface all the way to the cloud layer without impediment. Although it is hypothesised that the cloud driven turbulence is the controlling factor over cloud-surface coupling state this is not confirmed, nor are the factors that may influence cloud mixed layer depth in Arctic stratocumulus investigated. Using observational data from the Arctic that shows the turbulent structure we will investigate the controls over the depth turbulence from the cloud layer can reach down into the boundary layer.

As clouds are not explicitly simulated in regional or global scale models, cloud formation and microphysical processes are usually approximated and/or parameterised. Model representations of the Arctic are hampered by the paucity of observations within the region. This lack results in the use of parameterisations based upon cloud layers observed at lower latitudes. The use of these parameterisations leads to increased uncertainty in model outputs, as Arctic stratocumulus clouds and the boundary layers they top have been shown to differ from those at lower latitudes. The Arctic boundary layer is frequently topped by a humidity inversion where humidity increases above the temperature inversion, a feature not observed at lower latitudes. In mid-latitude stratocumulus, cloud top is usually at the base of the temperature inversion that tops the boundary layer. However, in Arctic stratocumulus cloud tops have been frequently observed to extend up into the temperature inversion. The extension of Arctic clouds into the temperature inversion has not been widely studied, and any impacts this extension has on the cloud layer are largely unknown.

Sedlar and Tjernström (2009) noted differences in the mean physical characteristics of clouds that were capped by the temperature inversion and clouds that had tops well within the inversion, the clouds that extended into the inversion much more likely to be mixed phase and have a longer lifetime than their inversion capped relatives. Sedlar et al., (2011) showed that for cases where cloud extended into the inversion the temperature inversion was typically deeper and stronger than the cases where the cloud layer had its top coincident with the inversion. The extension of cloud into the inversion was also associated with alterations to the clouds LW radiative profiles resulting in increased surface LW flux and increased outgoing LW flux by up to 10 W m^{-2} (Sedlar et al., (2011)). It is hypothesised that the extension of cloud layer into

the inversion may influence the distribution of turbulence within the cloud layer. Shupe et al. (2014) observed that the vertical motions within the top portion of the cloud layer behaved differently to those lower down in the cloud layer, potentially as a result of the top portion of the cloud extending up into the temperature inversion. As yet no study has examined in any detail the influence of the depth the cloud extends into the temperature inversion upon cloud dynamics, both in and under the temperature inversion. This thesis will carry out Large Eddy Model (LEM) simulations of mixed phase arctic stratocumulus with varying extensions of cloud top up into the temperature inversion to study the impact upon the cloud layer of the extension into the temperature inversion. There will be a key focus upon examining the impact of the extension upon the clouds ability to generate turbulence and the possible influence this will have upon the depth the cloud driven mixing may be able to reach down into the boundary layer. It is important to understand the impact of the extension of cloud top into the inversion as forecast and climate models are likely to find it difficult to directly resolve as the grid spacing used in such models is too coarse in the vertical. Improved understanding of the implications of extension of cloud into the temperature inversion will allow us to know if the omission of the process is likely to be a significant error in model simulations it cannot be resolved in and if future work on designing appropriate parameterisations is required.

In order to accurately simulate the Arctic environment in forecast and climate simulations, we must improve our understanding of the processes that occur within the Arctic Stratocumulus topped boundary layer. This project aims to improve our understanding of the controls on and behaviour of turbulence driven by in-cloud processes e.g. LW cooling, in Arctic mixed phase stratocumulus, and to characterise the response of the cloud to its extension into the temperature inversion. Improvement in our understanding of the controls on the depth of cloud driven turbulence, the cloud mixed layer, and the impact of the cloud layer extending into the temperature inversion, will enable a more accurate prediction of boundary layer turbulent structure.

This project will enhance our understanding of the dynamical behaviour of Arctic Stratocumulus by using observational data from the Arctic Summer Cloud Ocean Study (ASCOS) campaign and idealised simulations carried out

using the UK Meteorological Office Large Eddy Model (LEM).The project aims to answer the questions:

- What factors influence the depth that cloud driven mixing reaches down into the boundary layer in Arctic stratocumulus?
- How does the boundary layer radiative structure relate to its turbulent structure and the depth of the cloud mixed turbulent layer in Arctic stratocumulus topped boundary layers? Analysis will focus on decoupled conditions, where turbulent mixing is not continuous between the cloud and surface, as current model simulations already produce well mixed, coupled conditions.
- Does the extension of cloud top above the base of the temperature inversion and into the humidity inversion impact the turbulence generation within the cloud layer and the cloud mixed layer depth?

Chapter 1 covers the essential literature and information regarding Arctic climate change, the boundary layer, decoupling of the cloud layer from the surface, Arctic mixed-phase stratocumulus, their dynamics and their importance in terms of the Arctic climate. Chapter 2 examines the ASCOS observational data collected during an ice drift at 87°N during late summer 2008. Analysis focuses on data from the 25thAugust to the 1st September when the boundary layer was topped by a near continuous layer of mixed-phase stratocumulus. The range of instrumentation deployed during ASCOS provides extensive microphysical and dynamical profiles, with which the turbulent and microphysical structure of the boundary layer can is examined. The depth of the cloud mixed layer is derived and analysed in relation to the microphysical properties of the cloud layer. Chapter 3 builds upon the findings of Chapter 2 and explores the relationship between the ASCOS cloud mixed layer depth and its relationship with the radiative structure of the boundary layer. The turbulent structure of the boundary layer is examined in terms of the dissipation rate profiles and the Richardson number, which gives an indication of the turbulent state of the profiles. The radiative structure of the observed boundary layer is modelled in the LEM using the stand alone Edwards-Slingo radiation code. Idealised simulations of a decoupled mixed phase stratocumulus cloud are carried out in Chapter 4. A control simulation initialised using the observations of a decoupled cloud layer during ASCOS is

modified using variable IN concentrations to give a range of cloud layers with different liquid water paths (LWP). The response of the simulated cloud driven turbulence to variations in LWP is explored and the findings from the observational data expanded upon. In Chapter 5 LEM simulations are carried out to characterise the response of the cloud layer and the cloud mixed layer to variations in the extension of the cloud layer above the base of the temperature inversion and into the humidity inversion.

1 Literature review

1.1 The Arctic

The Arctic is classically defined as either the region north of the Arctic circle 66° 34' N, which is roughly the lowest latitude at which 24 hrs of light/dark occurs in the northern hemisphere, or as the region where the warmest summer temperatures do not exceed 10°C and the region north of the tree line (Figure 1.1).

The Arctic is made up of a region of water and sea ice, the Central Arctic Ocean, surrounded mostly by land which consists of a mix of snow and ice cover, bare rock and tundra. Transport of water into the Arctic Ocean from the Atlantic and Pacific Oceans occurs mainly via the Norwegian/Greenland sea's and Bering sea respectively. The Central Arctic Ocean is covered in semi-permanent sea ice which, currently, persists year round in some form at the pole. Sea ice cover in the central Arctic reaches its peak extent in March and minimum in September, with the majority of the ice cover being first year ice with thicker, longer lived, multi-year ice more prevalent near the coast of the Canadian Archipelago (Serezze and Stroeve, 2015). The Arctic experiences an extreme seasonal cycle with 24 hours of darkness during the winter and 24 hours a day of daylight during the summer with spring and autumn transition seasons where day length changes rapidly. Typical surface temperatures in the central arctic reach values below -20°C in the winter and are regularly under -30°C, increasing to 5°C in the summer (ACIA, 2004). A dominant feature of the Arctic atmosphere is the presence of extensive low level cloud cover. Low level cloud covers the Arctic Basin year round, cloud cover having been recorded as ~90% during the summer and ~70% during the winter by the Surface Heat Budget of the Arctic Ocean (SHEBA) experiment (Interi et al., 2002). Typically the clouds observed contain both ice and water droplets simultaneously (mixed phase) with stratocumulus the most prevalent observed cloud type

Figure 1.1 - Map of the Arctic showing different definitions of the Arctic boundary. Arctic circle is marked as dashed blue line, the 10°C isotherm as a solid red line and the tree line as a thinner solid dark green line. Reproduced from NSIDC (2018).

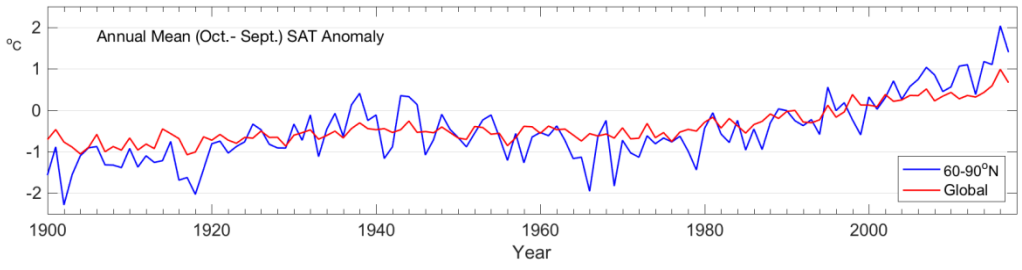

Figure 1.2 - Annual land surface temperature anomalies for the Arctic (blue) and global (Red) mean values, taken relative to the 1981-2010 values . Reproduced from Richter-Menge et al., (2017).

.

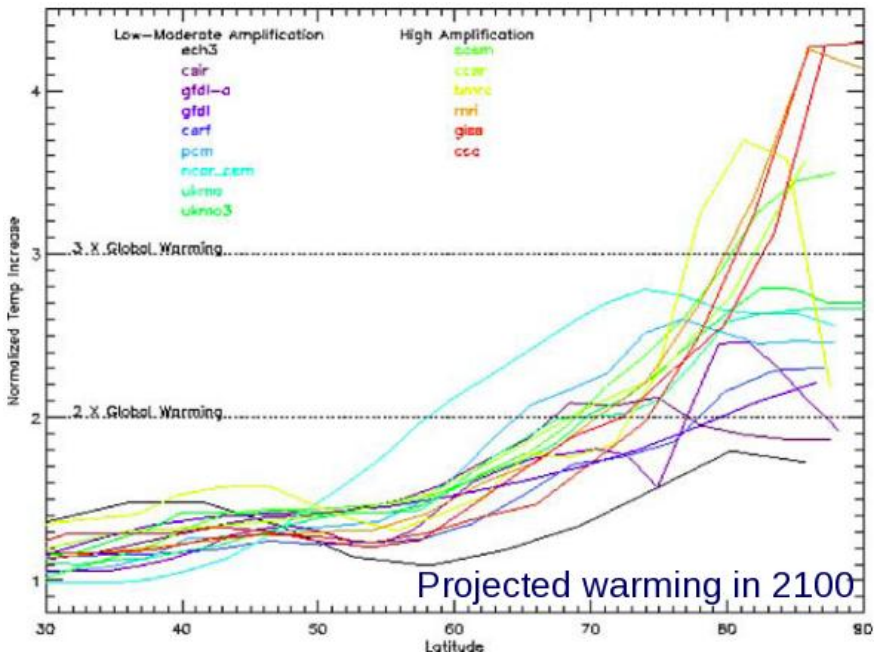

Figure 1.3 - Model simulations of the projected warming in 2100 demonstrating the enhanced predicted warming and intra-model spread in the Arctic compared to lower latitudes. The temperatures are zonal averaged and normalized by the average global 2xCO_2 air temperature increase. From Holland and Bitz, (2003).

In recent history Arctic climate has undergone a not insignificant change in mean temperatures, warming by an estimated 0.8 K since 1880 with the majority of that warming taking place since 1975 at approximately 0.15-0.2 K per decade (IPCC, 2013). Physical evidence of the warming is evident in the movement north of the 10°C isotherm with associated northward progression of the tree line (Zhang et al., 2013). Not only is the Arctic warming but it is observed to be warming at a faster rate than the rest of the globe with the current temperature anomaly of 60-90°N is double that of the global average warming (Richter-Menge et al., 2017). The recent warming of the Arctic shows no sign of abating, the land surface temperature anomaly in 2017 being the second highest on record since 1891 at +1.6 °C (Figure 1.2), with 2016 being the highest. The Arctic has been identified as one of the most sensitive regions on the globe too climate change (Hassol, 2005), with the predicted rate of change in the Arctic temperature the greatest of any latitude (IPCC, 2013); this is a consistent result across many different models (Figure 1.3, Holland and Bitz, 2003). Alongside the greatest predicted temperature change being seen in the Arctic the uncertainty in the prediction is also greater

than at lower latitudes, as demonstrated by the increase in intra-model spread in the projected surface temperature change towards the Arctic (Figure 1.3, Holland and Bitz, 2003). The wide range of the model values arises, in part, to a historical lack of observations in the Arctic with which to understand and parameterize processes unique to the Arctic environment. One of the most significant contributing factors in the large uncertainty of climate model predictions in general is the poor representation of clouds (IPCC, 2013). Clouds are not explicitly simulated in regional and global scale models and they, their microphysical processes, formation, and dissipation have to be parameterized. The lack of knowledge in terms of the processes occurring leads to errors in the parameterization or inappropriate parameterization choice and greater uncertainty in the final model output.

In the Arctic the general level of understanding regarding the complexity of the processes occurring within the clouds present is comparatively low compared to that at lower latitudes due to the scarcity of observations. The poor model representation of mixed-phase clouds is not only an Arctic issue but also occurs in the Southern hemisphere in the Antarctic over the Southern Ocean (King et al., 2015).

Non-cloud resolving numerical weather model simulations of Arctic observations have been shown to produce boundary layers that are too well mixed and shallow, resulting in clouds that are at too low a height, and with too low a liquid water content, resulting in errors in the calculated incoming and outgoing radiation and errors in the surface energy (Figure 1.4, Tjernström et al., 2008 and Birch et al., 2012).

1.1.1 Significance of clouds to Arctic climate

The accurate representation of modelled clouds in the Arctic is important as they are one of the most significant factors controlling the surface energy budget (Curry et al., 1996). The surface energy budget regulates processes such as sea ice melt, temperature and low level turbulence generation in the Arctic. For most of the globe low level stratocumulus clouds have a net cooling effect at the surface. However, both in-situ observations and modelling studies Arctic stratocumulus have been shown to produce a net warming effect at the surface during all but a short period during the summer when incoming solar

radiation peaks (e.g. Interi et al. 2002, Palm et al. 2010, Screen and Simmonds, 2010). Stratocumulus attenuate the incoming solar radiation (SW) before it reaches the surface. Over the majority of the globe the radiative shielding of the surface from SW radiation by stratocumulus provides a relative cooling at the surface. The presence of stratocumulus cloud also result in an increase in the relative long wave (LW) warming at the surface as the cloud is also radiating in the LW. In the Arctic the SW radiation is so weak for the majority of the year that the magnitude of the relative cooling from reduced SW flux at the surface is smaller than the LW warming. The result of being that the stratocumulus clouds in the Arctic produce a net warming for all but the height of summer when the shielding of the surface from SW warming is higher than the impact of the LW warming.

The warming (or cooling) effect of the cloud layer is primarily dependent upon the liquid water content (e.g. Stephens 1978). The warming influence of water containing clouds has been linked to events such as the onset of melting and related processes, including, in 2012, the first recorded melt event at summit Greenland since 1889 (Bennartz et al 2013). Francis and Hunter (2006) showed that an increase in the amount of cloud cover in the Arctic along with a rise in the abundance of liquid water in the clouds, altered the LW flux at the surface, contributing to an observed northward retreat of the sea ice margin. In terms of Arctic clouds impact upon climate warming, Varus (2004) investigated the changes to Arctic clouds under $2\times CO_2$ radiative forcing conditions using a global atmosphere ocean-mixed-layer General Circulation Model . Relative to the control run the model produced more cloud in the higher latitudes (Arctic) and less at lower latitudes. The changes to cloud cover was found to enhance the warming due to increased CO_2 radiative forcing at all latitudes. The warming due to cloud changes being at its greatest in the Arctic, with Varus (2004) attributing 40% of the observed warming to changes in cloud cover.

1.1.2 Sea ice

One of the examples of how the warming in the Arctic is altering the environment is the trend for decreasing sea ice extent over recent decades (Figure 1.5). Of particular interest is the decline in summer sea ice extent. The decrease in the summer sea ice cover in the Arctic has occurred at a faster

than predicted rate (Stroeve et al., 2007). Sea ice volume as well as extent has been lost, with satellite retrievals showing a reduction in the amounts of longer lived, and thus thicker, multiyear ice (Laxon et al., 2013). The September sea ice extent decrease from 1979-2014 has been $-86\,000\ km^2\ yr^{-1}$ with reference to the 1981-2010 values (Serreze and Stroeve, 2015).

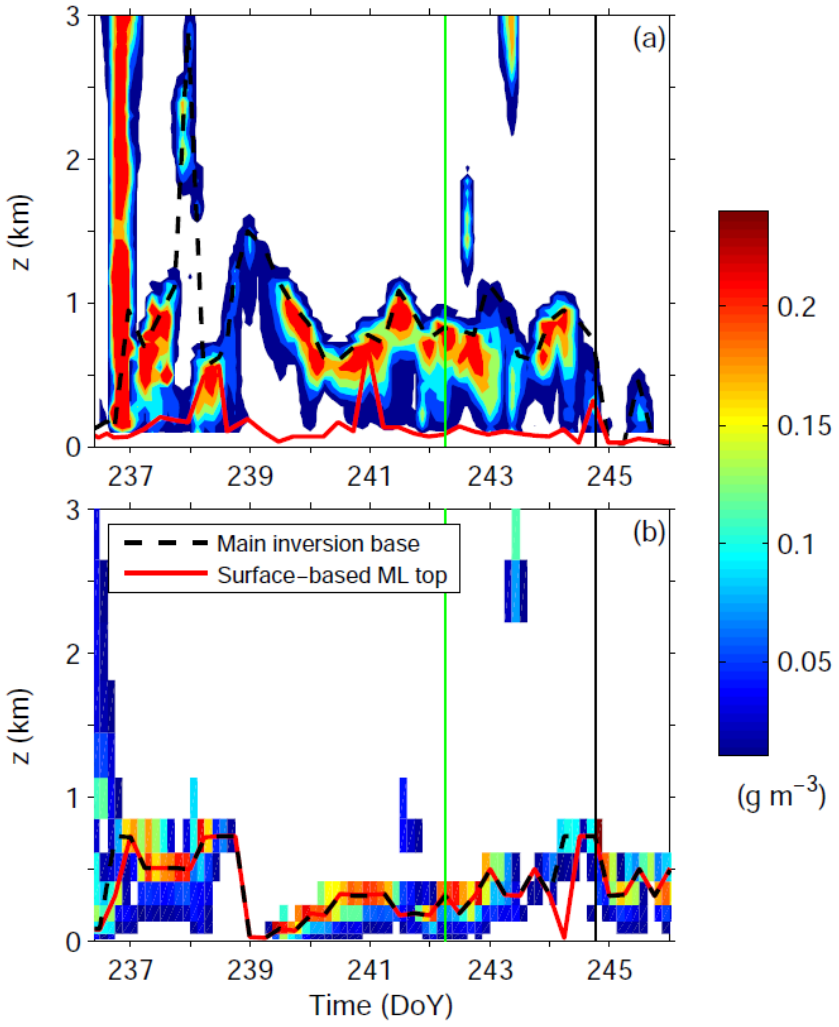

Figure 1.4 Comparison between (a) 3-hourly averaged observed and (b) MetUM output total cloud water concentrations from ASCOS. The MetUM output is clearly seen to produce a boundary layer that is too well mixed (e.g. no clear separation between inversion base and mixed layer top -red line surface mixed layer top and black dashed line the main temperature inversion base) with clouds that are too low and shallow, apart from day 245 where the MetUM over predicts cloud cover. From Birch et al., (2012).

Given the decreasing trend of summer sea ice in the Arctic various predictions have been made as to when, rather than if, an 'ice free' Arctic summer will occur, ice free being commonly defined as an extent at or under a value of 1 million km^2 (Wang and Overland, 2009). The recent accelerated loss of sea ice suggest that previous predictions, e.g. Boé and Qu (2009) who predicted an ice free Arctic by 2100, may have been too conservative. Predictions made by Overland and Wang (2013) suggest a range of dates from 2020 to 2040 using extrapolation of sea ice volume data, extreme ice loss events and climate models. The exact date of the onset of ice free Arctic summers is difficult to pinpoint exactly due to a mix of model uncertainty and internal variability in the Arctic climate system. Internal variability is found to not be the cause of sea ice decline by Jahn et al. (2016) as the decline occurs in all models in the ensemble used, but they did find that modification of the green house gas emission scenarios leads to a change in the onset range of consecutively ice free summers, stronger emission scenarios resulting in sooner consistent ice free years.

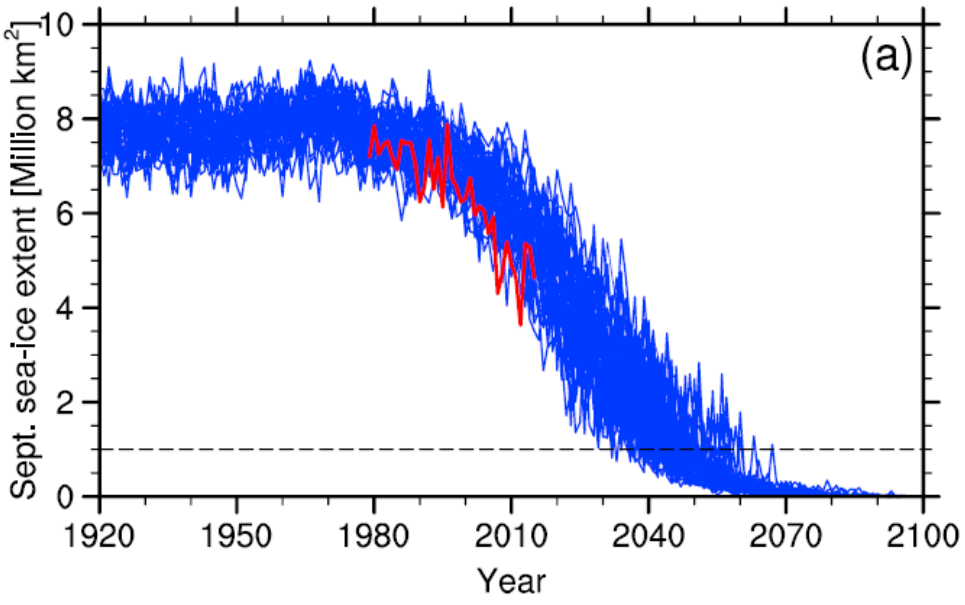

Figure 1.5 - Reproduced from Jahn et al. (2016). The red line shows the observed September sea ice extent as measured by the National Snow and Ice Data Center (NSIDC). The blue lines are the modeled sea ice extents from 40 climate ensemble runs. The dashed black line is the 1 Million km^2 threshold as classed as an ice free Arctic.

1.1.3 Impact of a warming Arctic

The impacts of a warming Arctic are likely to be far reaching and significant affecting the environment, wildlife and society as a whole. The selected examples given here are unlikely to be the full list of the impacts but do demonstrate the scope of the issue and importance of understanding the changes to the Arctic and need for accurate climate models so that we can inform and educate with the aim of mitigation and the implementation of adaptation where required.

Sea ice loss due to greater melting and reduced freezing will result in a loss of habitat for creatures that rely on it, such as polar bears. Polar bears use the sea ice as a platform for hunting, the lack of this platform means the bears are constrained to land for extended time periods and malnourished (Derocher, 2010). The lack of their usual food supply means Polar bears are forced to utilize other food sources , e.g. birds' nests in the Canadian Arctic (Iverson et al., 2014), impacting the wider ecology of the Arctic.

Sea ice loss around the margins of the Arctic Ocean is significant for the shipping industry. The reduction or loss of Arctic sea ice during the summer months will result in the extended use of the North-East passage and the consistent opening of the North-west passage shipping routes to commercial shipping. The Northwest passage potentially becoming a more economically viable shipping route than the Panama canal, depending on the fees imposed by the Canadian government (Lu et al., 2014). An example of the impact of the increased shipping on the Arctic environment is the associated increase in local emissions of black carbon, which can settle onto the surface reducing the albedo of snow and ice resulting in greater melting due to enhanced adsorption of LW radiation (Corbett et al., 2010).

The changes to the Arctic due to climate change are not limited to local impacts but have and are predicted to influence the globe as a whole. Warmer temperatures are leading to a thaw of the frozen soil (permafrost) around the Arctic, which aside from habitat changes, leads to the release of CH_4 and CO_2. The release of the CH_4 and CO_2 into the atmosphere will contribute to further warming and accelerate the thaw and release of even more CH_4 and CO_2 in a positive feedback loop (Schuur et al., 2015). Enhanced warming of

temperatures in the Arctic disrupts the typical synoptic-scale atmospheric pressure patterns; this disruption has been linked to a slowing in the progression of Rossby waves over the mid-latitudes and alteration of the path of the jet stream. The slowing of the Rossby waves can lead to the persistence of weather patterns over the mid-latitudes and the increased likelihood of extreme weather events such as heat waves and flooding (Francis and Vavrus, 2012).

1.2 The boundary layer

The atmosphere is divided up into distinct layers based on changes to the temperature profile throughout its depth. The layer closest to the Earth, where weather systems occur, is the troposphere. The troposphere is capped by the Tropopause which is identified as a distinct change in the temperature gradient as the temperature ceases to decrease with height. The change in temperature gradient signifies the end of the Troposphere and start of the Stratosphere, where temperatures continue to increase with altitude due to adsorption of radiation by ozone. The Tropopause is found at an average height of 12 km varying to be higher at the equator (18 km) and lower at the poles (9 km) due to thermal expansion.

The troposphere can itself be further broken down into distinctive layers, namely the boundary layer and the free-atmosphere. The boundary layer is the layer directly in contact with, and impacted by, the Earth's surface and is the atmospheric layer in focus in this thesis. The boundary layer may be cloud free or cloud topped (by fair weather cumulus or stratocumulus) and classically exhibits a pronounced diurnal cycle. The boundary layer air is, typically, well mixed and as such potential temperature tends to remain constant with height until its top. The free-atmosphere exists above the temperature inversion that typically caps the boundary layer. The free-atmosphere is typically stable and so potential temperature tends to increase with height, inhibiting vertical mixing. A stable atmosphere being when the temperature profile decreases with height in line with the dry adiabat, the rate of cooling of a dry air parcel due to expansion from lower atmospheric pressure aloft. A rising parcel of moist air cools at a slower rate than dry air as

latent heat is released as moisture condenses out due to the cooling caused by thermal expansion. The released latent heat offsets some of the cooling due to expansion and subsequently parcels of moist air follow the moist adiabat. An unstable atmosphere results when the temperature profile cools at a slower rate than the saturated adiabat.

The temperature inversion at the top of the boundary layer inhibits turbulent mixing upwards, restricting mixing to the boundary layer. Buoyant air from the boundary layer may sometimes overshoot the temperature inversion, subsequently mixing free troposheric air down into the boundary layer in a process known as entrainment. Mixing of surface air further up into the free troposphere only typically occurs during periods of deep convection, such as that during a thunderstorm when cumulonimbus are present, or the movement of weather fronts, both of which are uncommon in the high Arctic.

The structure within the boundary layer itself can be broken down into further layers and is variable in time depending upon the external forcing. Turbulent mixing is driven from the surface by wind shear (mechanically generated turbulence) and convection (buoyant forcing), and from cloud top by buoyant convection driven by long-wave raditative cooling of the upper cloud.

The Arctic summer boundary layer has been observed to often have a weak inversion at about 100 -400 m above the surface, decoupling the cloud deck above from the surface. The surface forcing is usually weak, with negligible buoyant forcing and typically weak winds (Brooks et al., 2017), maintaining the shallow well-mixed surface layer, while cloud-top cooling drives a cloud-mixed layer that extends to some distance below cloud base (Shupe et al. 2013, Brooks et al. 2017). The coupled/decoupled state of the boundary layer depends upon whether these two mixed layers overlap (Brooks et al. 2017).

1.2.1 Turbulence

Turbulence is, at a very basic level, the chaotic movement of a medium that is distinct from its mean motion. The motions cannot be predicted at a fine scale but the broader statistical behaviour can be derived and approximated by equations and subsequently modelled. The turbulence in atmospheric observations can be deduced using averaging to remove the mean flow from observations of the 3-dimensional wind components.

Atmospheric turbulence creates mixing in all three dimensions and is critical to the behaviour of the boundary layer and the clouds that occur. Turbulence exists at a wide range of spatial and temporal scales, the larger scale turbulence breaking down into smaller and smaller motions until the energy is finally dissipated in the molecular level as heat.

1.2.1.1 Turbulent Kinetic Energy

Turbulent kinetic energy (TKE) is a measure of the intensity of the turbulence in the boundary layer calculated from the balance of the sources and sinks of turbulence. The change in turbulence over time is the TKE budget tendency. The TKE budget equation, assuming horizontal homogeneity and ignoring subsidence is as:

$$\underset{1}{\frac{\partial \overline{TKE}}{\partial t}} = \underset{2}{\frac{g}{\overline{\theta_v}}\left(\overline{w'\theta_v'}\right)} - \underset{3}{\left(\overline{u'w'}\frac{\partial \bar{u}}{\partial z} + \overline{v'w'}\frac{\partial \bar{v}}{\partial z}\right)} - \underset{4}{\frac{\partial \overline{(w'TKE)}}{\partial z}} - \underset{5}{\frac{1}{\bar{\rho}}\frac{\partial \overline{(w'p')}}{\partial z}} - \underset{6}{\varepsilon},$$

Equation 1.1

where *t* is time, *g* is gravity, θ_v is the virtual potential temperature, *z* is height, *p* is pressure, ρ is air density, ε is the dissipation rate and *u/v/w* are the different wind componants (Garratt, 1992). Primed quantities indicate turbulent perturbations from the mean, and overbars indicate the averaging operator.

The different terms of the equation describe the different processes creating and dissipating turbulence. The first term of the equation is the tendency of TKE. The second term is buoyancy and it can be either productive or consumptive of TKE depending on the sign of the heat flux ($\overline{w'\theta_v'}$). The third term here is the production or loss of TKE due to wind shear. The fourth term is the contribution due to the vertical turbulent transport of TKE. The fifth term is the influence of pressure upon TKE e.g. the movement of gravity waves. The final term is the loss of TKE due to viscous dissipation as the energy is lost down the turbulent scales to be converted to heat.

Small scales of turbulence are driven by the cascade of energy down from the larger scales and so it is a reasonable assumption that the dissipation rate is larger during periods of greater turbulence production (Stull, 1988; Shupe et

al., 2012). The larger the production of TKE at a given point the larger the subsequent loss of energy at small scales as the energy cascades and the greater the dissipation rate, making the dissipation rate a proxy for the amount of turbulence at a given point.

1.2.1.2 Richardson number

The Richardson number (Ri) is a useful measure of turbulent state or stability of the atmosphere derived from the buoyancy and shear terms of the TKE equation. The Ri is calculated from the ratio of the consumption/production of turbulence from buoyancy to the generation of turbulence from wind shear. The most commonly used form of Ri is the gradient Richardson number (Ri_g), which is calculated as:

$$Ri_g = \frac{g}{\theta_v} \frac{\frac{\partial \theta_v}{dz}}{\frac{\partial u}{\partial z}^2 + \frac{\partial v}{\partial z}^2}$$

Equation 1.2

where θ_v is the virtual potential temperature, u and v are the horizontal winds and g is gravity (Stull, 1988). A negative Ri_g is indicative of a turbulent environment with values of $Ri_g > 0$ indicating some degree of stability, though there is a transition zone between the truly turbulent and non-turbulent states. The intermediate Ri_g values are between 0 and, values od 0-0.25 are considered stable according to buoyancy driven motions but turbulent due to shear while values of 0.25-1 are of an indeterminate state as they can retain some degree of turbulence (e.g. Stull 1993) or perhaps have turbulence initiated due to factors such as gravity waves (Meillier 2004, 2008).

In summary:

- Ri<0 - turbulent,
- 0<Ri<0.25 - thermodynamically stable, turbulent (shear driven)
- 0.25<Ri<1 – indeterminate - the turbulent state depends on past history, turbulence or laminar flow is maintained, but not actively forced
- Ri>1 – non-turbulent, laminar flow.

1.3 Stratocumulus topped boundary layer

Stratocumulus are a low level stratiform layer cloud that are weakly convective and have a fluffy cellular top and structure from the convective motions. Cloud top is, on the large scale, level and typically capped by the strong temperature inversion at the top of the boundary layer. Stratocumulus are the most common cloud type globally, covering around 1/5th of the Earth's surface, the majority of stratocumulus percentage being over the ocean at as opposed to the land (Hahn and Warren, 2007).

The ideal conditions for stratocumulus formation are when the boundary layer is relatively shallow, well mixed, above a surface source of moisture and in a region of large scale subsidence (Wood and Hartmann, 2006). The conditions for stratocumulus formation are frequently met over the western side of the ocean basins in the mid-latitudes and over the Arctic basin, where large scale persistent decks of cloud are observed (Hahn and Warren, 2007).

Shallow boundary layers enable the cloud driven mixed layer to more readily extend from the cloud down to the surface mixed layer. Mixing over the entire depth of the boundary layer enables transport of surface sources of moisture up to the cloud layer to replace moisture lost through precipitation, sedimentation and evaporation at cloud top due to entrainment of dry air.

The exact turbulent and thermodynamic structure of the stratocumulus boundary layer depends upon a mix of local processes alongside large scale forcing e.g. subsidence, winds, advection. Local processes can be broken down in to those due to the surface layer and those due to the cloud layer and their interaction with incoming radiation and are summarised in Figure 1.6.

In general, the stratocumulus topped boundary layer is well mixed with conserved quantities e.g. virtual potential temperature, constant throughout the profile, the temperature typically following the dry adiabat under the cloud layer and the wet within cloud. The temperature inversion at cloud top is enhanced in comparison to the cloud free boundary layer as radiative cooling from cloud top acts to cool the top of the layer (Lilly, 1968).

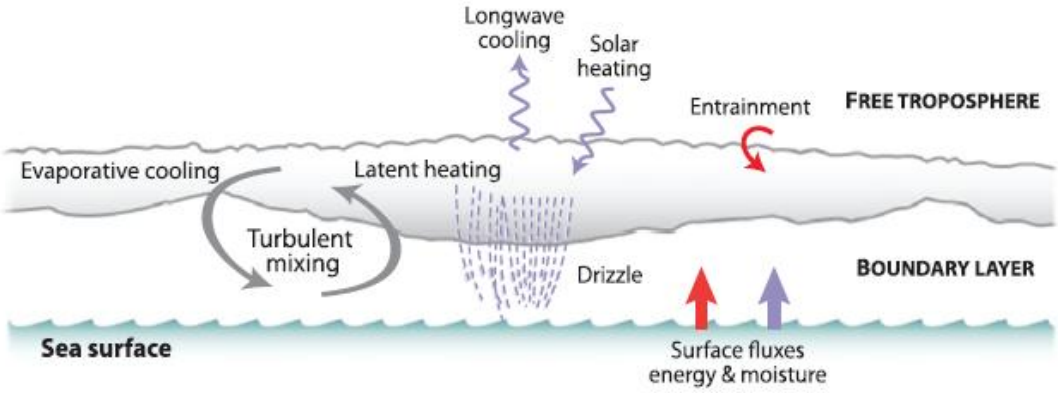

Figure 1.6- Diagram illustrating the basic local processes that govern the behaviour of the stratocumulus topped boundary layer (reproduced from Wood (2012)).

1.3.1 Radiative cooling in cloud

During conditions with little or no wind shear at cloud top in-cloud turbulence is mainly a result of radiatively driven processes (Lilly, 1968). LW radiation emission towards space by the cloud at and near its top creates cooling. The cooled air is denser than the air around it and so sinks. Downdrafts and updrafts mix the cloud and give rise to the formation of cellular patterns of areas of subsiding and rising air characteristic of the top of stratocumulus decks (Nicholls, 1984).

Early work on radiative cooling hypothesized that it all occurs within the temperature inversion at cloud top (Lilly, 1968) but further work by Deardorf (1981) demonstrated that the amount of cooling within the inversion is variable and that this fraction is important in determining the amount of cloud top entrainment.

The fraction of radiative cooling (FRC) that occurs within the inversion is linked to the radiative extinction depth and the ratio between the depth of the inversion and the height of the base of the inversion (Deardorf, 1981). The radiative extinction depth is determined by the cloud droplet size, phase, number and distribution. When cloud density is increased the fraction of cooling that occurs within the inversion is higher and consequently the amount of entrainment also increases, the converse being true for increasingly tenuous cloud (Deardorf, 1981). The relationship between cloud density to

radiation and the FRC is non-linear (Figure 1.7). A greater change to the FRC is seen with small density ratio changes at tenuous densities with the FRC reaching a plateau as density increases up to the point that further changes in density no longer alter the FRC.

Observation and model studies by Slingo et al. (1982) examining the liquid water profiles of nocturnal stratocumulus in relation to their vertical distribution of LW flux and cooling have complementary results to the work by Deardorf (1981). In clouds with adiabatically distributed liquid water profiles, higher liquid water paths presented sharper LW cooling peaks at cloud top. Sharper LW peaks are attributed to the higher cloud emissivity due to more liquid water. Emissivity is the ratio between the measured emitted radiation from a body and the theoretical emission of the body as a perfect emitter (a blackbody). As seen with FRC and cloud radiative density the relationship with liquid water and cloud emissivity is non-linear. A large change occurs in emissivity for a corresponding small change in liquid water at low liquid water values until the liquid water content is high enough that the cloud radiates as a blackbody. Once radiating as a blackbody, further increases in liquid water have no impact upon the sharpness of the peak in LW cooling. Denser clouds, e.g. those with higher liquid water contents, are therefore expected to have a sharper peak in cooling giving a higher FRC and greater cloud top entrainment.

1.3.2 Entrainment

The buoyant motions of the cloud layer from radiative cooling and latent heating creates mixing at cloud top. Air cooled by emission of LW cooling sinks away creating downdrafts, while rising parcels of warm air can overshoot the temperature inversion. The result is a layer of mixing at cloud top where the air from the free atmosphere is mixed down into the boundary layer or entrained. The layer in which entrainment occurs is known as the entrainment zone, classically defined as the region at the top of the mixed layer where the buoyancy flux is negative (Driedonks & Tennekes, 1984).

At cloud top entrained air at the mid-latitudes is warmer and drier than the cloud layer and so acts to counteract some of the radiative cooling and dry the layer at cloud top. A rise in temperatures and loss of liquid water to

evaporation have the result that in some instances entrainment can act to reduce the LW cooling and subsequent turbulence generation. Alternatively there are occasions when the entrained air causes a large enough amount of evaporation that the layer is made more turbulent, creating more mixing and entraining further air from aloft, causing further evaporation. The feedback of entrainment and cooling is known as cloud-top-entrainment instability and may continue until it eventually evaporates the cloud layer (Deardorf, 1980). In regions such as the Arctic where humidity increases above cloud top (e.g. Solomon, 2011) the impact of entrainment upon the cloud layer is likely to be different than the classical response.

1.3.3 Impact of aerosol variation on the cloud layer

Water droplets require very high super-saturations, that do not arise in the environment, to occur in the absence of a surface for water vapor to condense on to. In the atmosphere water vapor condenses on small hygroscopic nucli suspended in the air, aerosols, such as mineral dust, pollen, sea salt and gasses e.g. Dimethyl Sulphide (Barry and Chorley, 2003). The aerosol that enable condensation to occur are collectively known as Cloud Condensation Nuclei (CCN).

Cloud droplets do not readily freeze at sub zero temperatures and persist as super cooled liquid droplets down to -40 °C before they will freeze without a catalyst to the freezing process, homogonous freezing (Pruppacher & Klett, 1997). Aerosol acting as Ice Nuclei (IN) are relatively rare being much less common than those that act as CCN, CCN concentration usually ranging between 100 cm^{-3} and 1000 cm^{-3} in a typical marine environment (Raes et al., 2000) with IN concentrations being 10^{-5} to 0.1 cm^{-3} (DeMott et al., 2010). Different IN have varying temperatures at which they will facilitate freezing, so though a particular IN may be present ice may not have formed as the temperatures are still too high for the IN to be active.

The size, number and phase of water droplets/crystals as well as the total water content of a cloud impacts its emissivity altering the clouds radiative forcing. The amount of aerosol and the constituent CCN and IN available to an air parcel will impact the number, size and phase of any droplets that form within that parcel.

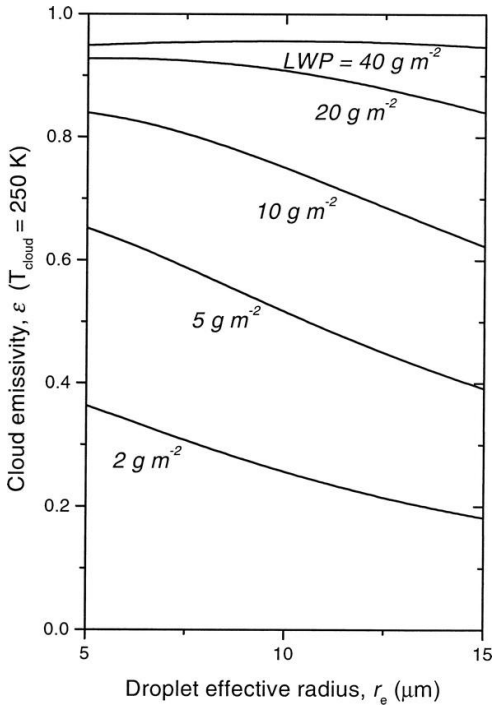

Figure 1.7. The derived sensitivity of cloud longwave emissivity to droplet effective radius and LWP at 250 K. From Garrett et al., (2002).

Garrett et al (2002) found little variation in the emissivity of a cloud layer due to droplet effective radius at Liquid Water Path (LWP) values over 40 g m^{-2} , for a constant cloud temperature of 250 K. The cloud is observed to already be radiating near to a black body at and above a LWP of 40 g m^{-2}. When radiating as a grey body (LWP < 40 g m^{-2}) variation in emissivity with droplet effective radius was seen to vary, with radius having an increasing impact as LWP drops (Figure 1.7).

If a cloud has sufficiently low LWP to be radiating as a grey body, such as in the low LWP cases observed over Barrow and during SHEBA (Sedlar, 2014), then variation in the CCN numbers and subsequent alteration to the droplet radius have the potential to impact the cloud's radiative cooling rates and the surface energy budget. In simulations of mixed phase arctic stratocumulus by Morrision et at. (2008), LWP was observed to increase with higher CCN and decrease with higher IN. Higher IN concentrations leading to more ice formation and more precipitation, which decreases LWP. Subsequently impacting the clouds radiative forcing, impacting the surface energy budget by what is known as the glaciation indirect effect (Lohman, 2002). At higher LWP

the addition of CCN in the simulations by Morrison et al. (2008) had negligible influence of the LW forcing but changes were apparent in the LW behaviour of the low LWP (< 50 g m^{-2}) clouds.

More detailed work specifically on the radiative and dynamical changes associated with droplet number variation in low LWP (<50 g m^{-2}) subtropical stratiform clouds was carried out by Petters et al. (2012). At substantially low (<20 g m^{-2}) LWP, higher droplet number led to greater radiative cooling at cloud top, above this very low LWP droplet number impact was near negligible. Short wave radiation was impacted at all LWP values, higher droplet number associated with increased SW heating. Higher droplet numbers during the night resulted in increased entrainment of the dry overlying air and a reduction in LWP, in the Arctic the overlying air is often more humid and so the LWP reduction may not result. Daytime simulations of the higher droplet number clouds also led to a reduction and eventual dissipation of the cloud layer which was attributed to the increased SW heating offsetting LW cooling and weakening the cloud's circulation. Short-wave warming resulted in decoupling which led to the cloud layer being cut off from the surface moisture source and reduced replacement of water lost via evaporation and detrainment. In the case of Arctic clouds the SW forcing is weak or nonexistent during the majority of the year and the overlying air is moist so although the reaction of the cloud dynamically to higher droplet number may be to radiate more effectively the response to that increased mixing may actually result in an increase in LWP as moist air is entrained from aloft as in Solomon et al., (2011).

1.3.4 Cloud controls on surface radiative forcing

The main controls on the radiative properties of a cloud are its liquid/ice concentration and the size and number of droplets/crystals. Liquid water being the dominant control on cloud radiative properties and the subsequent LW and SW forcing (e.g. Curry et al, 1996, Lilly, 1968).

The LW cloud surface forcing during ASCOS was found to range between 60-85 W m^{-2} for clouds with LWP over 50 g m^{-2} and with rapidly decreasing LW forcing as cloud emissivity dropped at lower LWP (Sedlar et al., 2011). Relatively small changes in LWP at sub 50 g m^{-2}, where the cloud radiates as

a grey body, resulted in a relatively substantial alteration to the clouds LW forcing consistent with the work by Petters et al., (2012) and Garrett et al., (2002).

The impact of aerosol due to its impacts on cloud droplets is known overall as the aerosol indirect effect which is broken down into the first and second effects. The first aerosol indirect effect being the impact of changes in droplet number/size (Twomey, 1977) and the second being the changes in precipitation amounts (Albrecht, 1989).

The impact of CCN addition to the net radiative forcing of low LWP clouds was investigated by Mauritsen et al., (2011) through the simulated addition of either 1 cm^{-3}, 10 cm^{-3} or 100 cm^{-3} CCN to the observed distributions for a given cloud. An additional 1 cm^{-3} was found to faintly increase the LW forcing. An additional 10 cm^{-3} CCN gave three times the increase in LW forcing of that from the addition of 1 cm^{-3} CCN and the cloud layer was classed by Mauritsen et al., (2011) as no longer being tenuous. The 100 cm^{-3} CCN simulations showed little further change in the LW forcing with further LWP rise (around 1 W m^{-2}) with the main change being in the SW where cloud forcing dropped by approximately 2.5 W m^{-2} to -5 W m^{-2}. The results from the Mauritsen et al., (2011) sensitivity studies demonstrates that in a 'tenuous' low LWP cloud regime in the Arctic the addition of relatively low amounts of CCN can have a substantial impact upon the cloud radiative forcing at the surface.

1.3.5 Coupling and decoupling of the cloud to the surface

In the stratocumulus topped boundary layer the cloud layer may be coupled or decoupled from the surface mixed layer. The stratocumulus topped boundary layer when well mixed throughout the full profile is classed as coupled. A decoupled state is where the cloud mixed layer and the surface mixed layers are distinct and do not meet. In the decoupled cloud topped boundary layer the profiles of temperature and humidity show constant but different well mixed values in the cloud-mixed and surface-mixed layers. The cloud and surface well mixed layers are separated in decoupled cases by a relatively stable intermediate layer e.g. Figure 1.9.

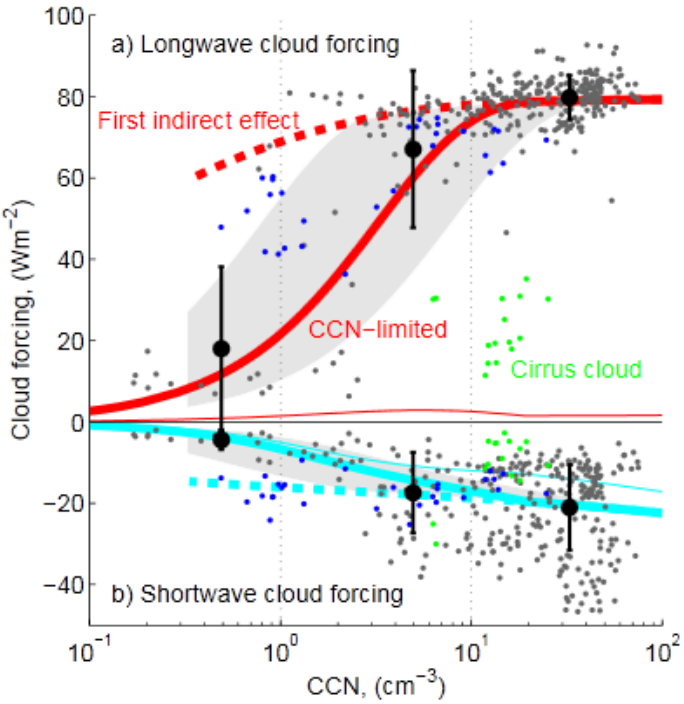

Figure 1.8 - Reproduced from Mauritsen et al. (2011). Modeled cloud surface forcing against CCN concentrations for both a) LW and b) SW radiation. Thick solid red and cyan lines are the idealized radiative transfer results for the runs where cloud can sediment out liquid, the thick dashed lines are for the first indirect effect only. The grey dots are the hourly averaged results from simulations of the cloud layer. The blue dots are a case where the results are particularly dependant on super-saturation. The green dots are a cirrus case. Large black dots are the bin averaged results. The grey shaded area is the range of the idealized lines based on sensitivity to variation in effective radius from 0 cm^{-3} to 30 cm^{-3} (solid lines being 15 cm^{-3}).

There are several different mechanisms by which decoupling can occur by causing the formation of a stable layer of air between the surface mixed layer and the cloud mixed layer. The main mechanisms are advection of a different air mass, deepening-warming of the cloud layer, cooling of the sub cloud layer due to drizzle, shortwave warming of the cloud layer and weak shallow cloud and surface turbulence layers.

Deepening-warming decoupling occurs over water when increased sea surface temperatures result in changes to the latent heat and buoyancy flux profiles and a deepening of the cloud layer result in a discontinuity and the cloud layer decouples from the surface (Bretherton and Wyant, 1997). An

example of deepening-warming decoupling in the literature is that observed by Jones et al., (2011) of a stratocumulus deck over the Pacific Ocean. They observed a stratocumulus deck that gradually thickened and began drizzling further away from shore, in association with increasing surface temperatures, eventually becoming decoupled. An increase in the latent heat fluxes over the warmer water increased the buoyancy flux in the cloud layer, causing it to deepen and rise. While the cloud layer rose the buoyancy fluxes in the layer underneath were found to stay the same or slightly decrease. The discrepancy in latent heating and buoyancy fluxes throughout the profile eventually leading to the cloud layer decoupling from the lower part of the boundary layer just under cloud base.

Decoupling due to drizzle occurs due to the drizzle warming the cloud layer (condensation) and cooling the layer beneath (evaporation), by the latent heating/cooling creating a temperature discontinuity that decouples the cloud layer from that underneath. The cloud layer warms as the drops condense and the layer underneath cools as the falling droplets evaporate (Brost et al., 1982). Drizzle decoupling behaviour is not a universally observed occurrence in stratocumulus clouds. Jiang et al., (2001) simulated a drizzling Arctic stratocumulus cloud and found that while the drizzle did stabilise the sub cloud layer that cloud base actually descended so the decoupling influence of the drizzle was not as pronounced.

The impact of ice precipitation on the Arctic boundary layer turbulent structure has been shown to vary in significance. Harrington et al. (1999) showed ice precipitation to be a strong stabilizing influence but simulations by Sarve et al. (2015) found the influence of ice to be less significant due to the already high humidity of their surface layer. The high humidity at lower levels in the boundary layer suppressed the amount of sublimation and subsequent latent cooling in the sub-cloud layer. In a case where the moisture increased aloft the sub-cloud layer became moister as more liquid was entrained. The cooling in the sub-cloud layer was subsequently reduced but the cooling near the surface was unchanged and so the stability under the sub-cloud layer increased and the layer decoupled from the surface. Reducing the moisture aloft had the opposite effect, increasing the latent cooling in the sub cloud

layer, creating stronger downdrafts which turbulently coupled the cloud and surface layers.

Work by Ovchinnikov et al. (2011) looking at the addition of extra ice to a mixed phase cloud supports the idea that increased ice formation and precipitation lead to decoupling. Latent heat released in downdrafts due to higher levels of ice formation (in a high IN run) reduced the levels of negative buoyancy weakening the circulation in the cloud.

Shortwave warming related decoupling is commonly observed as part of the typical diurnal behavior of marine stratocumulus and has been widely observed and modeled (e.g. Sandu et al. 2008, Rogers and Olsen 1990, Turton and Nicholls 1987 and Nicholls 1984).The marine stratocumulus rise and gradually thin throughout the morning, eventually decoupling from the surface later in the day and potentially then breaking up completely (Turton and Nicholls 1987). The incoming SW radiation offsets some of the LW cooling that creates cloud mixing at the top of the cloud layer and evaporates cloud droplets, thinning the cloud and weakening the strength of cloud driven turbulence. The warming of the cloud layer due to SW heating is at a greater rate than that below, creating a temperature discontinuity and forming a stable layer, effectively decoupling the cloud from the surface.

Shortwave warming decoupling can, rather obviously, only occur when the incoming shortwave radiation is present and strong enough to have a significant influence on the cloud layer. In locations such as the high Arctic shortwave warming's influence on decoupling and boundary layer structure is only likely to play a role during the mid-summer when incoming radiation peaks. Tjernström (2007) examined the diurnal cycle of the stratocumulus topped boundary layer in the central Arctic using observational data from July-August collected during the Arctic Ocean Experiment 2001. There was found to be a small but statistically significant diurnal cycle in the cloud layer, if much less pronounced than that observed at lower latitudes. In contrast to the lower latitudes the cloud base was found to lower during the morning, with cloud top rising and peaking in height in the afternoon. Decoupling predominantly occurring during the 'night' with cloud driven turbulence picking up in the morning and gradually mixing its way towards the surface recoupling the cloud

layer. During the decoupled period humidity is trapped in the surface layer, once re-coupled the trapped moisture mixes up to the cloud and the cloud thickens and eventually begins to drizzle. The cycle observed by Tjernström (2007) is subsequently observed to be opposite to that found in marine stratocumulus. In the high Arctic and over the central Arctic Ocean the surface fluxes are generally low and conditions result in a relatively shallow surface mixed layer (e.g. Birch et al., 2012). Whether or not coupling or decoupling of the cloud and surface occurs in the Arctic is thought to be primarily due to the depth cloud driven turbulence reaches (Tjernström et al., 2012).

1.4 The cloud topped Arctic boundary layer

During the summer months in the Arctic the stratocumulus topped boundary layer profile is predominantly weakly stable or near neutral and frequently decoupled (e.g. Solomon et al., 2011, Shupe et al., 2013 and Sotiropoulou et al., 2014). Decoupled profiles were observed during ASCOS 75% of the time according to Shupe et al. (2013). The main impact of decoupling is the inhibition of transport from the surface up to the cloud layer. During periods of decoupling the transport of surface sources of aerosol and moisture will be limited and the cloud properties subsequently influenced.

A distinguishing feature of the lower atmosphere in the Arctic as opposed to that of lower latitudes is the presence of an increase in humidity above the top of the boundary layer. Moist air from over the ocean is advected northwards over the ice, cloud formation occurs at the top of the boundary layer and the humidity then drops as the cloud precipitates and moisture is lost to the surface (Curry et al., 2000).

A humidity inversion above cloud top is present in 75-80% of all the SHEBA and ASCOS data according to Sedlar et al. (2011), making it a significant feature of the typical Arctic atmosphere.

The top of Arctic mixed phase stratocumulus frequently extends up above the temperature inversion and into the humidity inversion, in contrast to lower latitude stratocumulus that have cloud top located at the base of the temperature inversion at boundary layer top. The extension of cloud into and potentially above the temperature inversion creates an extended cloud top

zone with different behaviour to that of cloud top in a typical stratocumulus (Solomon et al., 2014).

The surface mixed layer in the Arctic is typically shallow, 10's to a few 100's of meters, and its depth is mainly determined by wind-shear (Brooks et al., 2017) as the surface heat fluxes are weak (e.g. Birch et al., 2009).

The impact of boundary layer structure and the impact of near surface temperature inversions on Arctic Amplification was investigated by Bintanja et al. (2011).The study ran a series of simulations at ×2 and standard CO_2 forcing, with alterations to the boundary layer mixing from adjustments to the Richardson number dependant mixing coefficients. The amount of mixing in the boundary layer was found to govern how much of the warming at the surface can be offset by being be 'diluted' to higher levels through mixing. Impaired mixing was found to even further amplify the warming at the surface during all but the summer months.

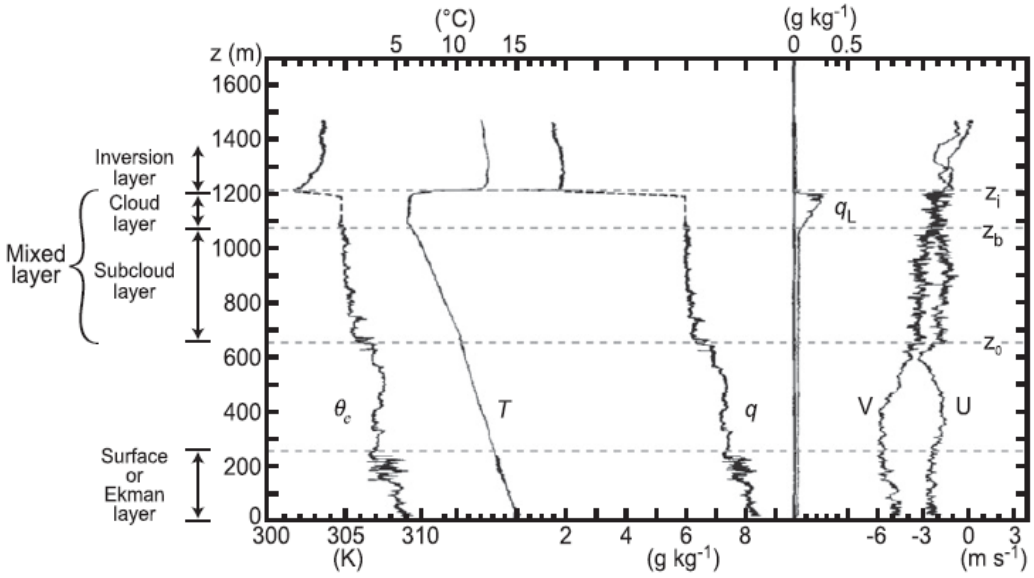

Figure 1.9 - An example of the different layers of the boundary layer and profiles of water vapour *q*, liquid water q_l, equivalent potential temperature θ_e, temperature *T* and the horizontal winds *U V*, observed in a decoupled Stratocumulus cloud over the North Sea. Figure reproduced from Wood (2012) who adapted it from Nicholls and Leighton (1986).

Surface sensible heat fluxes were found by Sarve et al. (2015) to be a weakly destabilising influence on the boundary layer structure when warming the surface layer and stabilising when negative. A positive latent heat flux also acted as a stabilising influence by reducing the potential cooling from sublimation and evaporation by moistening the surface layer.

1.4.1 Arctic mixed phase stratocumulus

1.4.1.1 Persistence

The vapour pressure over ice is lower than that over water and so the tendency is for ice crystals in a cloud to grow at the expense of water vapor when both are present, a process known as the Wegener–Bergeron–Findeisen (WBF) mechanism. The ice crystal will eventually then grow so large at the detriment to any liquid droplets that the ice falls from the cloud and so gradually depletes the amount of available water vapor in the cloud layer. The persistence of mixed phase clouds in the Arctic is surprising because the WBF mechanism means a mixed phase cloud might be expected to fully glaciate and dissipate due to water loss through precipitation. The general high percentage of cloud cover in the Arctic is attributed partly to the absence or low impact of dispersive processes e.g. strong precipitation and synoptic circulation, as well as the generally high level of water vapour in the air from sources such as convective plumes over open leads (Curry et al. 1996). More specifically the longevity of mixed phase Arctic Stratocumulus is attributed to the entrainment of moist air, increases in local relative humidity due to adiabatic expansion in updrafts, and a relative scarcity of IN relative to CCN (Morrison et al., 2012) as well as the relatively quick loss of ice from the cloud layer as it rapidly grows and precipitates (Savre et al., 2015).

The constant loss of ice from the cloud layer as the crystals grow and fall results in a depletion of the total water content of the cloud layer and so to maintain the cloud an influx of moisture is required. Water vapour can enter the cloud layer via entrainment from above or mixed up from bellow.

It is thought that the extension of cloud top into the humidity inversion is an important source of moisture for mixed phase stratocumulus in the Arctic and an important factor in their unexpected persistence and high percentage prevalence. To investigate the impact of the humidity inversion and sub cloud

water vapour upon cloud persistence in the Arctic, Solomon et al. (2014) conducted a series of idealized Large Eddy Simulation runs. The model runs were conducted with and without the humidity inversion above cloud, high and low water vapour under cloud and a 'dry' run with low water vapour both above and under the cloud layer. In the 'dry aloft' case the cloud layer cooled at a greater rate due to less LW insulation from water vapour aloft. The air evaporating into the layer above added to the cooling giving rise to increased downdrafts, deepening the cloud layer and lowering its base. The lower cloud base and enhanced mixing subsequently entrained more moist air from the sub cloud layer than the control run with the LWP reaching the same level as the control case with moisture above. The moisture inversion above cloud was partly restored after 12 hrs of model time in the dry aloft run due to the detrainment (evaporation and upward mixing) of cloud top.

Solomon et al. (2014) also found that removal of the sub cloud moisture produced a cloud layer with a LWP that trended back towards the control level, though never fully returning to control levels of LWP. Arctic mixed phase stratocumulus appeared slightly more sensitive to removal of moisture below cloud than above, but the cloud was still able to effectively obtain enough moisture from either source to maintain similar levels of liquid water. Only in the run where the both the layers above and under the cloud layer had reduced water vapour did the LWP stay consistently significantly below that of the control run levels. This modelling study demonstrated that Arctic mixed-phase stratocumulus are remarkably robust to changes in the source of moisture regarding their persistence and maintenance of LWP. It is also the case that even though the LWP was 80% that of the control run in the 'dry' simulation the cloud layer still remained after the full 12 hours of simulation time.

Regarding the role that ice plays in mixed phase clouds Solomon et al. (2014) found that the removal of ice processes in their large eddy simulations led to a much thicker and higher LWP cloud layer developing. The no ice simulated cloud increased in LWP throughout the entire 12 hr simulation, the control run with ice processes present reached a stable LWP after 2 hours. Ice processes lowered cloud water content via the WBF mechanism concurrently reducing the rate of cloud base decent as the heat released from freezing reduced the

strength of the downdrafts (Solomon et al.,2014). Ice processes in the cloud layer increased precipitation and the presence of ice throughout the boundary layer decreased cooling rates in the sub cloud by reducing the available water for condensation as the ice crystals grow.

1.4.1.2 Cloud Seasonal Cycle

Total cloud fraction in the Arctic is dominated by low level clouds in simulations by Varus (2004), consistent with observations from comparative observational studies. Low clouds are more common during the summer months than the winter months, peaking at fractions just over 0.8 during September in the simulations and never dropping under 0.4 during the winter months. The converse trend is true for high clouds, although high cloud fraction remains under 0.2 at all times during the year. Stratocumulus fraction occurrence in the Arctic shows a seasonal cycle with the lowest fractions during the winter at ~70% and highest in the summer months when it can reach 90% (Interi et al., 2002).

The presence of more ice and its lower residence time in the cloud layer relative to liquid is thought to account for some of the reduced cloud cover during the winter months, as well as higher ice causing more precipitation. Other reasons for the reduced cloud cover during winter is the reduced levels of surface moisture in comparison to the summer months as the ocean surface is exposed more frequently during the summer and so there is greater available liquid water vapour (Hermann and Goody 1976).

1.4.1.3 Low liquid water path

In contrast to mid-latitude stratocumulus observations of low level, sub 50 g m^{-2}, liquid water path (LWP) clouds are not uncommon over the Arctic and have been observed to have an occurrence of 30-40% (Bennartz et al., 2013). A decade of observational data on Arctic clouds from over or near land is available from Barrow and a year of observations from over the sea-ice is available from SHEBA. Using the Barrow and SHEBA data Sedlar (2014) found that low-level single layer clouds, such as those to be studied in this thesis, occurred 22-30% of the time. Sedlar (2014) separated out the single layer cloud cases into those classed as optically thick with a liquid water path (LWP) of 75-300 g m^{-2} and thin 0-50 g m^{-2} with the higher LWP, optically thick,

cases all from the Barrow data and the optically thin cloud from both Barrow and SHEBA. The higher LWP clouds were observed to have a deeper cloud mixed layer and thus likely to be more frequently coupled to the surface layer.

1.4.1.4 Encroachment into the inversion

A unique feature of the Arctic stratocumulus topped boundary layer is the encroachment of cloud up above the base of the temperature inversion at cloud top and into the inversion (e.g. Tjernström, 2005 and Sedlar and Tjernström, 2009). Sedlar et al. 2012 investigated how frequently the cloud top extended up into the inversion in observations from Barrow Alaska, ASCOS and SHEBA. Cloud top encroachment was found to occur in 60% of the SHEBA cases, 66% of the ASCOS data and 33% of the Barrow data. The Barrow data has significantly less incidence of cloud extending aloft than the ASCOS and SHEBA, data indicative that extension into the inversion is more likely over the central Arctic than the surrounding land.

The humidity inversion aloft and the extension of cloud up into the temperature inversion have been cited as reasons for the unexpected persistence of the mixed-phase in Arctic stratocumulus (Morrison et al., 2012) and their longevity (Solomon et al, 2011). The impact of extension up into the temperature inversion upon the cloud layer dynamics and its behaviour is not widely studied and so the impacts upon cloud layer and boundary layer structure largely unknown.

1.4.2 Aerosol sources in the Arctic

During the summer in the central Arctic the background aerosol concentration is low and transport of anthropogenic aerosols is limited (Mauritsen et al., 2011). Consequently, the emission of aerosol acting as CCN or IN from the surface is thought to be of increasing importance during the summer months.

During the last few days of the ice drift during ASCOS Tjernström et al., (2012) found the dissipation of the cloud layer and lack of cloud formation to be associated with very low (<1 cm^3) CCN concentrations. The importance of accurate appropriate parameterisation and simulation of aerosol conditions was demonstrated by the failure of the Met Office Unified Model to simulate the clear conditions during the low CCN conditions. The Met Office model

erroneously produced a cloud layer during the cloud free period, an error attributed to the use of a fixed CCN concentration of 100 cm^3 in the model (Birch et al., 2012 and Hines et al., 2017). In addition to the lack of accuracy in producing clear conditions the errors in CCN concentration also lead to inaccuracy in the amount and phase of droplets/crystals in the clouds that were simulated, with the Met Office Unified Model miscalculating the sign of the net surface radiative flux during ASCOS due to errors in the cloud properties (Birch et al., 2012). Prenni et al (2007) studied clouds observed during the Mixed-Phase Arctic Cloud Experiment (MPACE), finding that errors in the parameterisation of IN could result in errors of 10-100 Wm^{-2} in the surface energy budget.

Errors in the parameterization of aerosol in the Arctic are primarily attributed to a lack of direct observations on concentrations and poor knowledge regarding the sources and sinks of the aerosol (e.g. Browse et al., 2012). Anthropogenic aerosol, from heavy industry in the high Arctic, in Russia for example, is widely transported to the Arctic during the winter and spring as the polar front is at its most southern so the polluted air can be carried northwards on the circulation (Curry et al., 1996). The polar front retreats northwards of the heavy industry emissions around the edge of the Arctic during the summer and so transport from the lower latitudes is more limited .

Local sources of aerosol are also important, particularly when the transport of anthropogenic aerosols is limited and background concentrations are low during the summer. Local sources of aerosol are not well understood, due to the paucity of observations, but a diverse range of CCN and IN sources have been proposed. The ejection of droplets resulting from the bursting of bubbles in the open leads as bubbles trapped in the ice melt and rise results in airborne sea-salt and biological particles (Nilsson et al., 2001), such as marine-microgels (Orellana et al., 2011). The breakdown products of Dimethyl Sulphide from periods of high biological activity are a source of surface aerosol over open water during the spring and summer periods (Leck and Persson, 1996).

2 ASCOS – Observational Work

2.1 Introduction

Clouds are the dominant control over the surface radiation budget in the Arctic (Shupe & Intrieri, 2004.) The most prevalent cloud type is low-level, mixed phase stratocumulus. Despite their importance to the Arctic climate and radiation budget our understanding of the behaviour of Arctic clouds is limited, mainly because of the paucity of direct observations. Our lack of understanding of Arctic clouds and their specific behaviour results in errors in model simulations because parameterisations from mid-latitude stratocumulus are used (e.g. Birch et al., 2009). Model simulations struggle to represent both the location of cloud and the structure of the cloud topped boundary layer in the Arctic (Tjernström et al., 2008), for example frequently predicting the boundary layer to be too shallow and well mixed (Birch et al. 2012). Observations from both ASCOS and SHEBA show the Arctic boundary layer to be frequently decoupled, exhibiting a distinct and separate turbulent surface mixed layer with a cloud mixed layer above a relatively stable layer that separates the two (e.g. Sotiropoulou et al. (2014) and Solomon et al. (2011)). Whether or not the surface and cloud mixed layers meet and turbulent exchange is possible between the surface and the cloud layer has the potential to have an impact upon the cloud layer itself in terms of the supply of moisture and aerosol from surface sources. Tjernström et al., (2012) suggest that due to weak surface fluxes and in the absence of other factors the dominant control on decoupling in the arctic between cloud and ground is the depth of cloud driven turbulence.

The Arctic Summer Cloud-Ocean Study (ASCOS) was an observational, ship-based campaign that took place during the late summer of 2008 in the central Arctic. It focused on Arctic clouds and their interaction with the boundary layer and surface Tjernström et al., (2014). The ASCOS campaign collected a wide range of meteorological observations of the stratocumulus topped boundary layer that provide a detailed picture of the thermodynamic and turbulence structure of the boundary layer, throughout its full depth, along with the

properties of boundary-layer clouds. The turbulence data collected during a two week period of ASCOS, alongside the range of meteorological variables, provides the opportunity for investigation into the behaviour and controls over cloud driven turbulent mixing in Arctic stratocumulus.

2.1.1 Hypotheses

A. That dissipation rate is a reliable and useful way of determining the depth that the cloud mixed layer can reach down into the sub cloud layer. That dissipation rate and cloud mixed layer depth are a reliable way of determining the turbulent coupling state between cloud and surface.
B. That there is a link between the physical properties of the cloud layer and the depth that cloud driven mixing reaches. The hypothesis being that the cloud driven turbulence is primarily controlled by the amount of LW cooling at cloud top. The amount of liquid water within the cloud layer is a key factor in determining the LW radiative properties of the cloud layer, including the emissivity. We therefore expect a correlation between the cloud mixed layer depth and the cloud microphysics, primarily the liquid water due to the impact of liquid water variation upon the clouds LW radiative properties.

2.1.2 Aims

The overall aim of this thesis is to improve our understanding of the influences upon the depth of the cloud mixed layer in the Arctic. Subsequently improving our ability to predict when the cloud is coupled to the surface in conditions where the depth of cloud driven turbulence is the dominant influence upon coupling. Specifically the aims of the analysis of the ASCOS observational data are to:

1. Find an effective way to measure the depth and variability of the cloud driven mixed layer down from cloud top using dissipation rate. Allowing assessment of whether the boundary layer is coupled or decoupled and the vertical extent of the cloud driven turbulence.
2. Investigate the relationship between cloud microphysical and radiative properties in relation to the vertical extent of mixing to identify any

possible relationships and controlling factors over the depth of the cloud mixed layer.

3. Identify key areas to investigate in more detail in focused modelling work.

2.2 ASCOS

The data used in this chapter was collected during the ASCOS field campaign. ASCOS was carried out with the aim of understanding the processes controlling the properties of the summertime Arctic cloud-topped boundary layer, the cloud, and the surface energy budget during the Arctic summer through direct observations (Tjernström et al., 2014).

The measurements used here were collected during Aug-Sept 2008, and include both in-situ measurements and remote-sensing retrievals. These provide a short but reasonably comprehensive view of the microphysical and turbulent conditions in the boundary layer over the sea ice of the central Arctic Ocean during the late summer and the very start of the winter freeze-up.

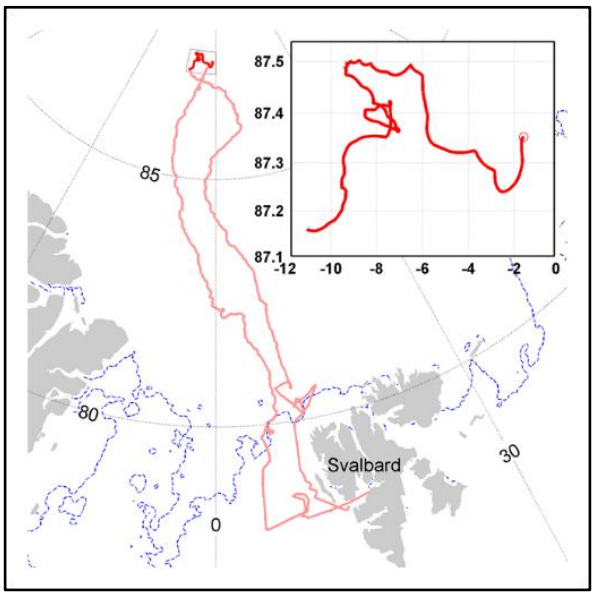

Figure 2.10- The track of the Oden during the ASCOS campain. The pink line is the ship track with the red portion highlighting the ice drift portion. The ice drift is shown in detail in the subplot. The ice edge as of 12th August 2008 is shown in blue. Reproduced from Mauritsen et al. 2011)

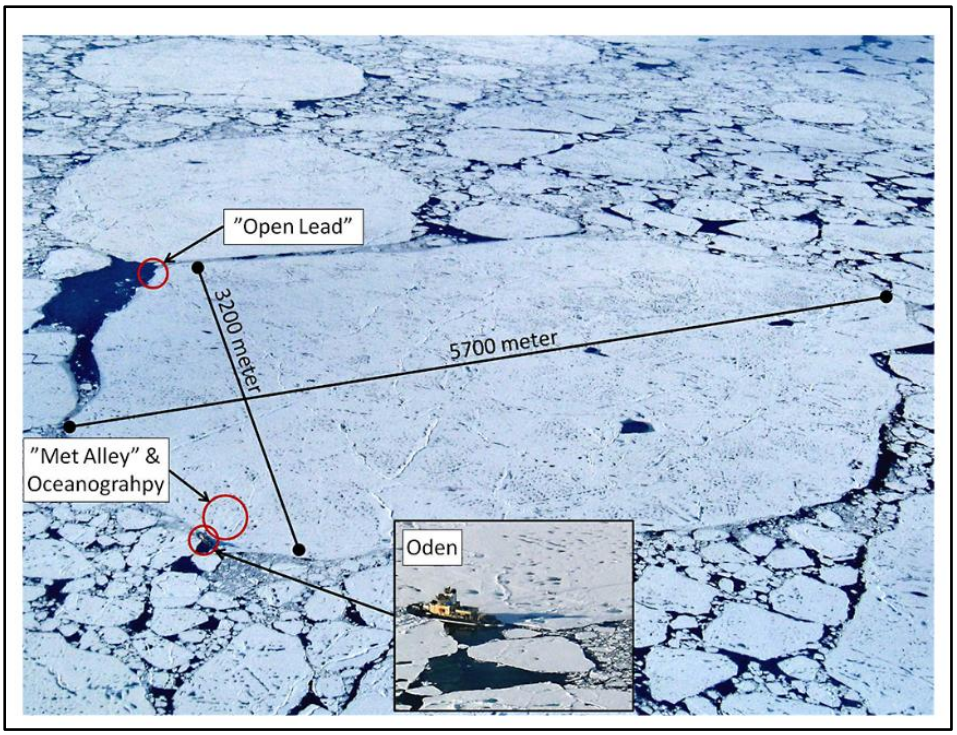

Figure 2.11- Photograph of the ASCOS siteshowing sea ice conditions, size of the floe and location ofdeployed meteorological equipment. Reproduced from Tjernstrom et al., (2014).

The ASCOS campaign began as the ice breaker *Oden* departed Longyearbyen on the 2nd of August 2008. From Svalbard the ship travelled north, through the ice edge, up to a maximum latitude of ~87°N. On the 12th August the *Oden* was moored to an ice floe with which it drifted until the 1st of September. Once the ice drift was completed the *Oden* sailed south, returning to Longyearbyen, ending the campaign on the 9th of September (Figure 2.10).

The ice floe the *Oden* was moored to measured 3.2 × 5.7 km and was surrounded by smaller floes amid patches of open water with one more defined 'open lead' area of water (Figure 2.11). During the ice drift instrumentation was deployed onto the floe in various locations monitoring the ocean, open lead and surface meteorology. In addition to the measurements on the ice floe an extensive suite of meteorological variables were recorded by the weather station on board the *Oden*. The *Oden* measurements ran throughout the entire ASCOS cruise inclusive of the ice drift period. A suite of remote-sensing instrumentation was installed on the *Oden,* measuring profiles of winds, temperature, water vapour and cloud water content. Direct measurements of the profiles are also available from regular radiosonde

releases throughout the cruise as well as from a tethersonde deployed during the ice drift.

The bulk of the measurements made during ASCOS, and all the data used in this thesis, were collected during the ice drift portion of the campaign. The analysis carried out here focuses on the Stratocumulus dominated second week of the ice drift 25th August to 1st September. The first week of the ice drift is not analysed here as it was heavily influenced by the passage of convective frontal systems with deep cloud which are not the focus of this thesis (Figure 2.12a,b), conditions during the portion of ASCOS analysed in this thesis are discussed in detail in section 2.2.2.

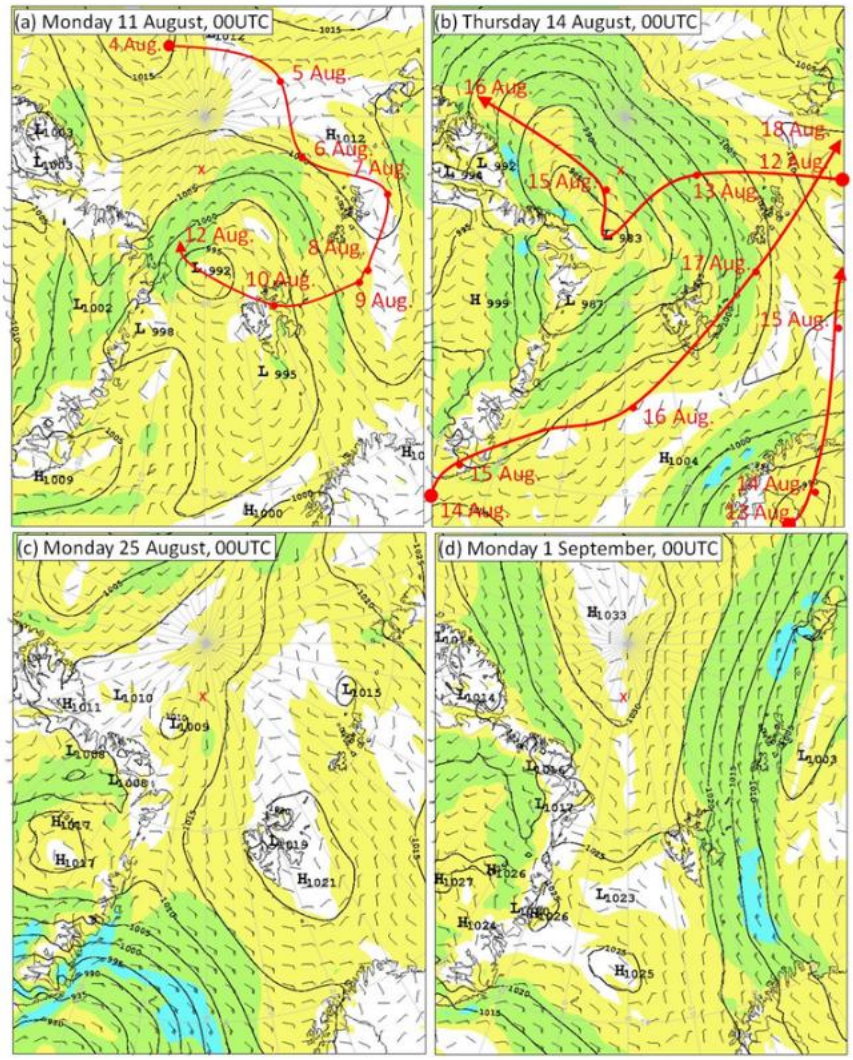

Figure 2.12- Surface pressure charts black (lines), location of the Oden (red x), path of low pressure system/s during first half of the ice drift (red line) and surface winds (colours and wind barbs). Reproduced from Tjernstrom et al., (2012).

2.2.1 Instrumentation

A detailed description of the ASCOS campaign and all the instrumentation information is given by Tjernström et al. (2014). Only the instrumentation relevant to the analysis carried out in this thesis is described here (Table 2.1).

Basic meteorological measurements of temperature, pressure and humidity are available for the entirety of ASCOS from a WeatherPak weather station installed on the 7th deck of *Oden*. In addition to the weather station on the ship a suite of surface-based instrumentation was set up on the ice floe. Named 'Met-Alley', the installation consisted of two micrometeorological masts. A 15 m mast was instrumented with 5 levels of turbulent flux measurements from sonic anemometers (2 of which were collocated with high frequency water vapour measurements from Li-COR Li-7500 open path gas analyzers) along with measurements of mean temperature and relative humidity. A 30 m mast was instrumented with a single sonic anemometer at its top, to extend the turbulence measurements as high as possible.

At an undisturbed location away from the other instrumentation the incoming and outgoing short and long-wave radiation fluxes were measured by pairs of Eppley pyranometers and pyrgeometers.

Profiles of temperature, humidity and winds up to a height of ~500 m were measured by a tethersonde. The tethersonde ran nearly continuously between the 17th August and the 1st September. Additional atmospheric profile measurements were taken by 6-hourly radiosonde launches providing temperature, pressure, humidity and wind measurements during the whole campaign.

A suite of remote-sensing instrumentation was installed on the *Oden*, giving near continuous measurements throughout the depth of the boundary layer. A vertically pointing MilliMetre Cloud Radar (MMCR; Moran et al., 1998), provided measurements of radar backscatter intensity and Doppler vertical velocity. A laser ceilometer provided profiles of backscatter intensity and estimate of cloud base height.

Observations	*Instrument*	*Notes*
Atmospheric temperature profiles	60 GHz Microwave radiometer	0-1.2 km Error < 1 °C E-S model
	6-hourly radiosonde	LEM initialisation E-S model
Surface pressure	*Oden* WeatherPak	LEM initialisation E-S model
2 m air temperature	Thermometer - 'Met Alley'	
LWP	Microware Radiometer 23.8 & 31.4 GHz	Error ~ 20 g m^{-2}
Cloud base height	Celiometer	
LW and SW incoming and outgoing surface radiation	Epply pyranometer and pyrgeometers	
IWP,IWC	MilliMetre Cloud Radar (MMCR)	E-S model
Cloud top		
w		
ε		
Droplet and Ice effective radius		E-S model
Mean winds profiles	449 MHz Wind Profiler	144 m to 3 km
Wind speed profile	Scintec MFAS phased array Doppler Sodar 6-hourly radiosonde	0-600 m
Humidity profiles	6-hourly radiosonde	LEM initialisation E-S model
Ozone soundings	Electrochemical sensor on sondes	
Surface albedo	Epply pyranometer and pyrgeometers	LEM initialisation E-S model
Pressure levels	6-hourly radiosonde	LEM initialisation
10 m wind speeds	Anemometer - 'Met-Alley'	LEM initialisation
Humidity and temperature in surface layer	*Oden* WeatherPak	Used for LCL calculation
Surface sensible, latent heat fluxes	Sonic anemometers	LEM initialisation

Table 2.1 - Table of observations used, their instrumentation source and any relevant notes on errors and what data is used in following chapters for radiation modelling (E-S model) and Large eddy modelling (LEM initialisation).

Profiles of atmospheric temperatures up to a height of 1.2 km, were retrieved every 5 minutes from measurements from a 60GHz scanning microwave radiometer. The radiometer retrieval uses microwave brightness temperature measurements to adjust a prior radiosonde profile using the method of Westwater et al. (1999). The brightness temperature retrieval becomes weaker at higher levels and so the resultant profiles increasingly resemble the linearly interpolated radiosonde temperatures with height, temperature at cloud top may therefore be less reliable than lower down in the profile. Vertical

profiles of half hourly mean winds were retrieved from a 449MHz radar wind-profiler from 144 m up to 3 km. A Scintec MFAS phased-array Doppler sodar, installed close to the masts on the ice floe, provided 10-minute average wind speed profiles up to approximately 600 m. Liquid water path (LWP) and precipitable water vapour was provided by a vertically pointing dual wavelength radiometer (Westwater et al., 2001).

The remote sensing measurements are combined to provide retrievals of cloud bulk, microphysical, and dynamic properties (Shupe 2007; Shupe et al. 2008; Shupe et al. 2012). Cloud top and bottom were calculated in the same manner as Shupe et al. (2012) with the cloud base taken from laser ceilometer measurements and the cloud top from the MMCR.. The cloud top is taken as the highest point in the instantaneous MMCR profile, up to 2031 m, that had a reflectivity above -50 dB. Cloud liquid water content is estimated from an assumption that the profile is adiabatic, and constrained by the total liquid water path. The boundary layer turbulent profiles in terms of dissipation rate was derived from the MMCR profiles (Shupe et al., 2012).

2.2.2 Overview of conditions during the ASCOS ice drift

The first half of the ice drift was influenced by unseasonal synoptic activity with a sequence of low pressure systems and associated deep fronts passing over the drift site. The first low pressure system moved over the ASCOS site at the very start of the ice drift on the 12th August (Figure 2.12a). A second low pressure moved over the site on the 14th-15th of August from the East and carried on westwards over the Canadian Archipelago (Figure 2.12b). Further low pressure systems developed in the Arctic during the first part of the ice drift but the site was not directly influenced by another low pressure system until the 23rd August. The low pressure on the 23rd was the last storm system to pass near the ASCOS site with conditions then becoming more typical of expected Arctic synoptic state, a neutral or weakly stable stratocumulus topped boundary layer, in the latter half of the ice drift.

The larger scale synoptic conditions during the second week are dominated by high pressure. Mean sea level pressure generally rises throughout the week as a high pressure system travels up from Svalbard towards the North Pole (Figure 2.12c,d). A subjective analysis of the passage of warm and cold fronts

over the ASCOS site was carried out by Tjernström et al (2012) by looking at the rate and sign of equivalent potential temperature change in the observed profiles and cloud characteristics from the MMCR

Figure 2.13). Several weak warm fronts were identified as passing over the ASCOS ice drift site during the second week on the DOY 240, 243 and 244 with a cold front observed right at the end of the drift period on the 1st

Figure 2.13). Tjernström et al (2012) noted that the height of the cloud tops changed with the passage of the warm fronts but that the stratocumulus layer remained persistent.

All of the analysis in this thesis chapter is carried out using only the second week of the ice drift – August 23rd to September 1st – and so the more specific meteorological variables discussed below are described only for this analysis period. Full meteorological descriptions of the entire ASCOS campaign are given in Tjernström et al (2014).

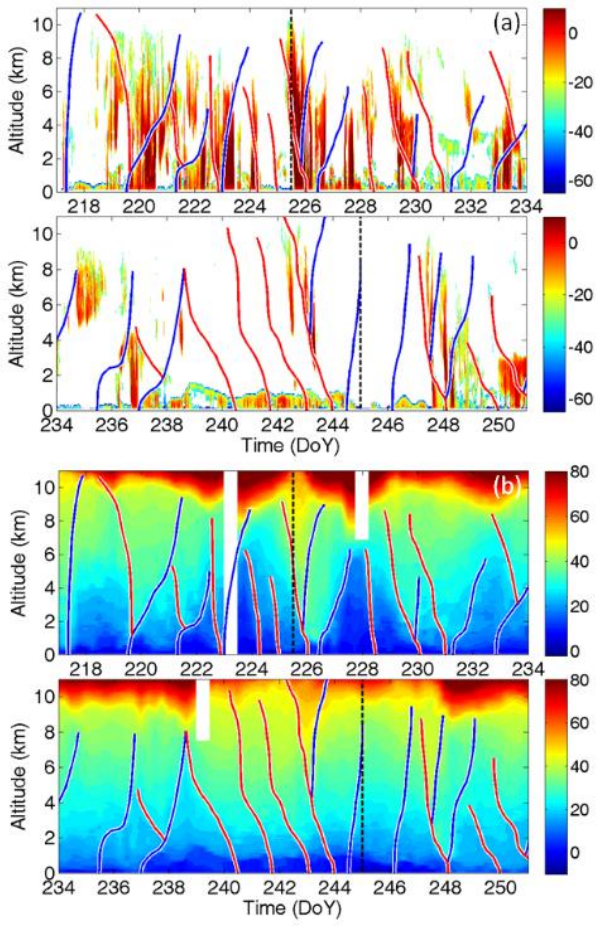

Figure 2.13- Time-height plots of a) MMCR radar reflectivity (dB Z_e) and b) radiosonde equivalent potential temperature (°C). The blue lines indicate cold fronts and the red lines warm fronts (subjective). Reproduced from Tjernstrom et al. (2012). Doy 6th Aug to 7th Sept

The stratocumulus layer is observed to be mixed phase throughout the 23rd to the 1st, with a peak in liquid water in the top third of the cloud layer (Figure 2.14 and Figure 2.15). Cloud phase is derived from a combination of cloud radar, depolarization lidar, microwave radiometer and radiosonde measurement are used in a stepwise progression to narrow down the phase at a given point (Shupe 2007).

Ice is present to some degree over the full depth of the boundary layer for nearly the entire analysis period (Figure 2.16). Higher levels of ice are seen during periods of precipitation in the form of light snow, which sublimates/evaporates before reaching the surface, as seen in the higher Doppler reflectivity levels dropping off before the surface and indicated in the cloud phase figure (Figure 2.16 and Figure 2.14). Periods of precipitation are identifiable by the increased Doppler reflectivity and velocity seen below cloud base e.g. 28th and 29th August (Figure 2.17). The precipitation is identified as ice, with the highest reflectivity values caused by the large surface area of snow. The majority of the snow and ice falling from the cloud layer appears to sublimate before reaching the ground (Figure 2.16, Figure 2.15) and specific humidity (Figure 2.18) can be seen to increase under cloud base down to the base of the cloud mixed layer in terms of the dissipation rate e.g. on Aug 28th - 29th (Figure 2.19). Humidity peaks are also seen at/above cloud top and in the surface layer. The peaks in humidity at the surface are more noticeable during the local 'night'; the sun does not set during ASCOS but there is a clear diurnal cycle in the SW radiation

Figure 2.20e) consistent with the results of an analysis of diurnal cycles in the Arctic by Tjernström (2007).

Throughout the week the persistent mixed phase stratocumulus cloud top varied between 800-1400 m and cloud base between 200-800 m (Figure 2.17). There was a small altocumulus present during the afternoon of the 29th with an associated reduction in the depth of the stratocumulus layer attributed to radiation shielding (Sedlar and Shupe, 2014). Other than the one

altocumulus cloud there was only one layer of lower level cloud under 2 km and out of contact with the surface during the week. At the surface light fog was present during the 25th to 26th and early on the 31st. Higher level cirrus ice clouds observed at >3 km were detected intermittently in association with the weak frontal systems passing over the ASCOS site

Figure 2.13).

Mean wind speeds at 10 m stayed under 5 m s^{-1} for the entire second week of the ice drift. The ice surface temperature remained near constant at -1.7 °C, which is close to the freeze/melt point of salt water, up until the end of the 30th August. The cloud cover thins and dissipates completely on the 31st; the associated surface and 2 m temperatures drop as it cools to space. The 2 m air temperature

Figure 2.20a) shows more variability than the surface temperatures but follows the same trend, dropping on the 31st as the cloud thins and a weak cold front moves through. The drop in temperatures has been identified as the likely point of the end of the summer melt and the onset of the winter freeze period (Tjernström et al 2012). The onset of freezing in the Arctic has been identified as typically occurring between the second week of August to the first week of September (Belchansky et al., 2004), so the timing of the ASCOS observed freeze is typical. The trigger to the timing of the freeze is the drop in temperatures due to the reduction of cloud cover, Sedlar et al (2011) suggest that the presence of the stratocumulus layer prior to this time delayed the onset of the winter freeze up.

Overall the ASCOS period used in this thesis is typical of the expected summer conditions in the Arctic and consistent to the conditions observed during other Arctic observation campaigns e.g. SHEBA (Interi et al., 2004).

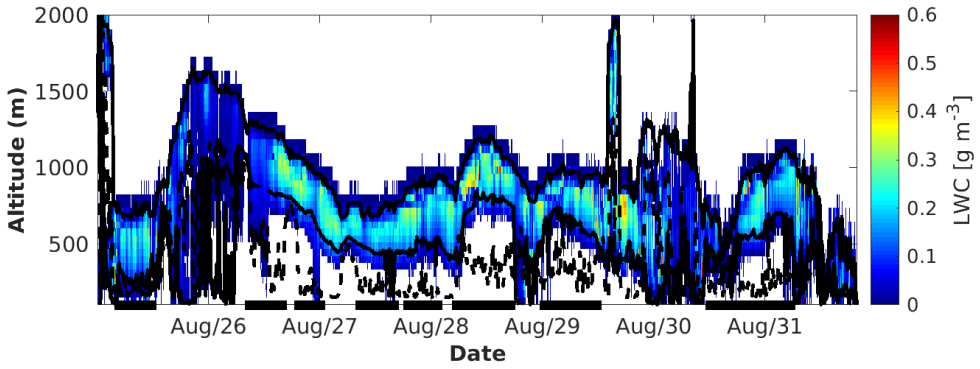

Figure 2.14- Liquid water content. Lines: cloud boundaries (solid black line) and base of the cloud mixed layer (dashed line), data subset used in analysis squares along x-axis.

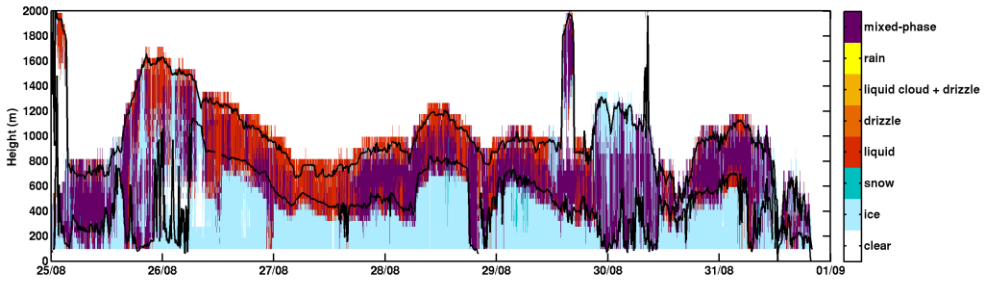

Figure 2.15- Cloud phase as derived by Dr M Shupe lines as Figure 2.14.

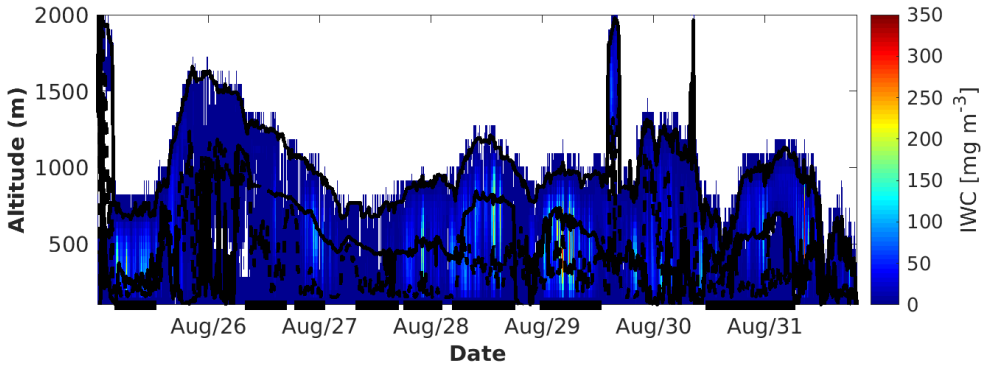

Figure 2.16- Ice Water Content, lines as Figure 2.14.

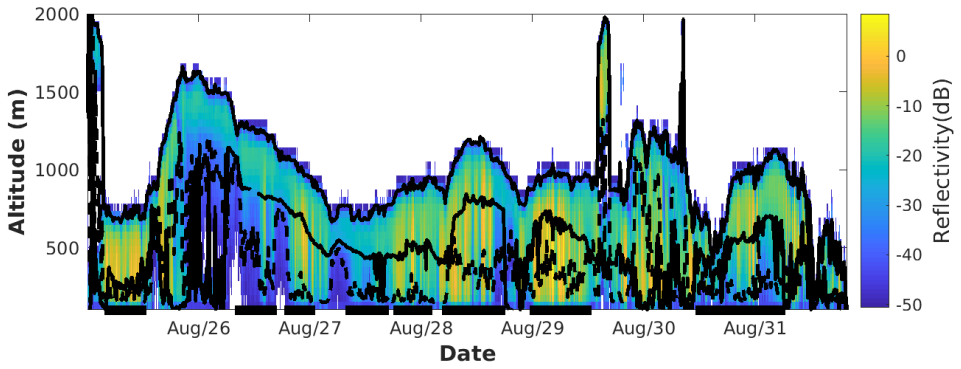

Figure 2.17 - Time height series of MMCR reflectivity (dB), capped above --50 dB, lines as Figure 2.14.

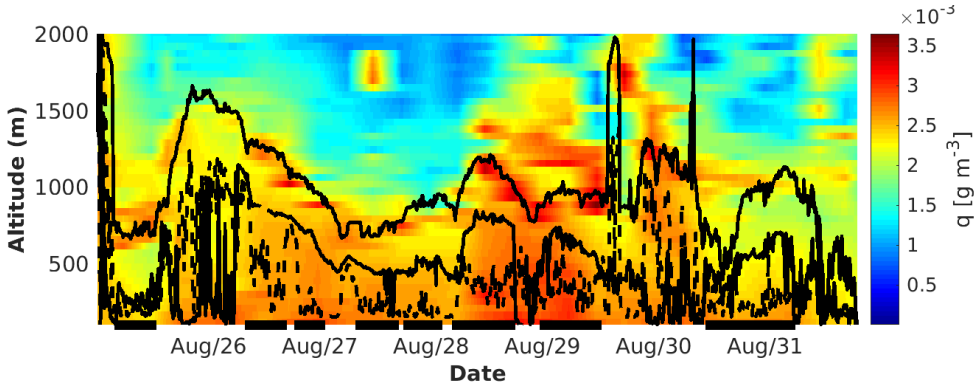

Figure 2.18- Specific humidity. Lines as Figure 2.14.

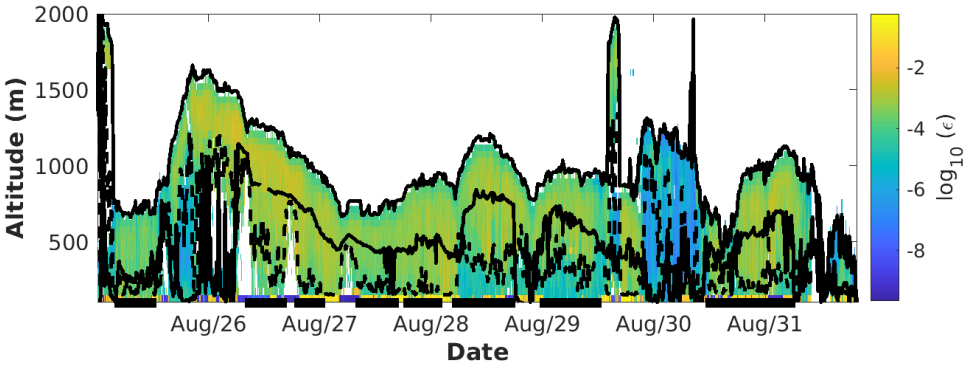

Figure 2.19- MMCR derived dissipation rate. Lines as Figure 2.14.

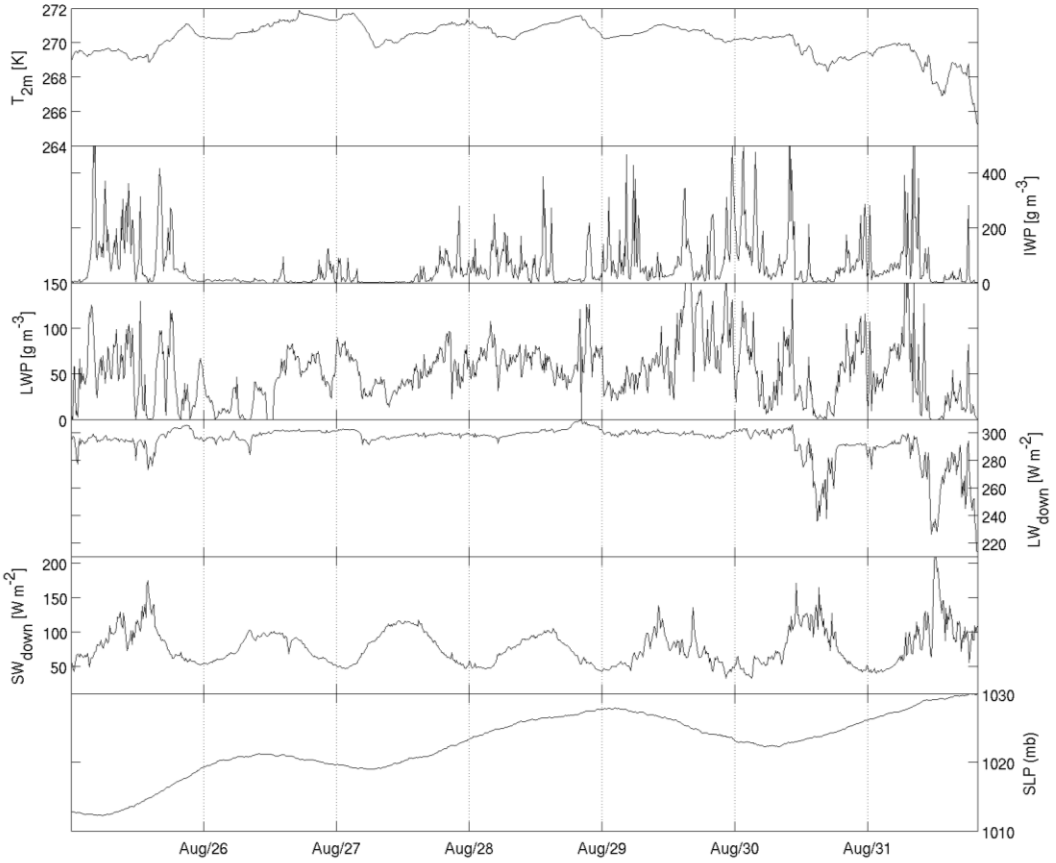

Figure 2.20- Observations of (top to bottom) 2 m temperature, ice water path, liquid water path, down welling LW radiation, down welling SW radiation and surface level pressure during the stratocumulus dominated period of the ASCOS ice drift 25th August-1st September 2008.

2.3 Data averaging

The sampling frequency, times, and heights of the measurements from different instruments is variable. In order to combine data from all the separate retrievals the observations must be averaged over equal intervals and time matched. Fixed 10 minute averages were used.

All data were also averaged down or interpolated onto a fixed vertical grid, matching that of the MMCR data. The MMCR data being the key observations in this thesis providing information on cloud properties and boundary layer turbulent structure in terms of the dissipation rate retrievals (Section 2.4.3).

2.4 Derived data from remote-retrievals

2.4.1 Liquid and ice concentrations and paths

The liquid water content profile was derived using the microwave radiometers and the ice water distribution retrieved from the MMCR. The vertical extent of the cloud liquid water is well defined in non-precipitating conditions, but the exact vertical distribution is unknown. The liquid water concentration profile was therefore refined using the assumption of an adiabatic distribution constrained by the LWP with an uncertainty of ± 20 g m^{-2} (Birch et al, 2012).

The vertical extent of the ice water is well described by the MMCR data but the relative errors of the total ice water concentration in the column is much higher than that for the liquid water values (error in ice water path could be up to a factor of two) (Birch et al., 2012).

The ice and liquid water concentrations were used in conjunction with other data from the temperature profiles, MMCR and radiometers (Shupe et al., 2012) to derive cloud phase classification.

2.4.2 Lifting Condensation Level

The lifting condensation level (LCL) is defined as the height at which a parcel of air would reach 100% saturation if lifted adiabatically from the surface. The LCL is therefore an estimate of the height cloud base would be located in a well-mixed, or coupled, boundary layer. A LCL height lower than the observed cloud base is indicative of less well-mixed potentially decoupled conditions (Stull 1988).

The LCL for ASCOS was calculated from the temperature and specific humidity measurements from the WeatherPak weather station on *Oden*. The ship weather station was located at a height of 20 m above the surface. The LCL is calculated by:

$$z_{LCL} = \frac{T_0 - T_{dew}}{\Gamma_0 - \Gamma_{dew}}$$

Equation 2.3

where z_{LCL} is the height of the LCL, T_0 is the starting temperature, T_{dew} is the dewpoint at the starting temperature, Γ_0 is the atmospheric lapse rate (wet or dry) and Γ_{dew} is the lapse rate of the dewpoint.

The LCL is calculated by finding the temperature expected at the LCL and then applying an appropriate lapse rate to find the height at which this temperature would be reached. During ASCOS ice was nearly always present, albeit in very low quantities, beneath cloud base (Figure 2.16). Due to the near constant ice presence the lapse rates were calculated assuming saturation with respect to ice.

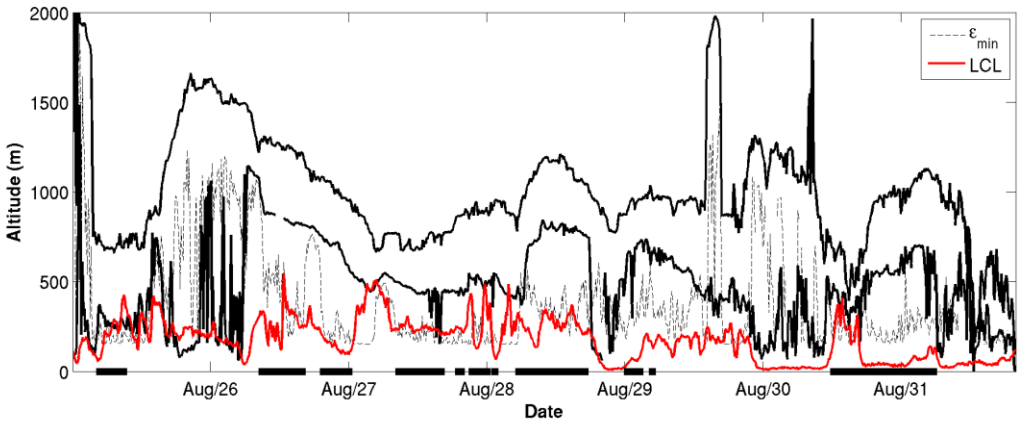

Figure 2.21- Time series of the height of the LCL (red). Cloud boundaries are the solid black line, the lower limit of the cloud mixed layer from the dissipation rate (dashed line). Periods included in analysis highlighted by black marks along the x axis.

The LCL was used by Jones et al., (2011) during VOCALS-REx in order to determine if the sea surface and stratocumulus deck were decoupled. They calculated the LCL using aircraft measurements from sub-cloud flight legs, using observations from the lowest 25 % of the boundary layer. The boundary layer was classed as coupled (decoupled) if the calculated LCL was within (further than) 150 m of (from) cloud base.

For the ASCOS data analysed the calculated LCL varies in height from the surface to roughly 500 m (

Figure 2.21). The boundary layer is considered coupled if the LCL is at (within the bounds of one vertical averaging level 45 m) or above cloud base. The

LCL was also used by Dong et al. (2015) to quantify the 'degree' of decoupling. The LCL decoupling index D_{LCL} is defined here as:

$$D_{LCL} = \frac{\bar{Z}_b - \bar{Z}_{LCL}}{\bar{Z}_b},$$

Equation 2.4

where $\bar{Z}_b$ is the height of the mean cloud base and $\bar{Z}_{LCL}$ is the height of the mean lifting condensation level.

2.4.3 Dissipation rate

The time series of Doppler vertical velocity measured by the MMCR can be used to estimate the turbulent dissipation rate ε, as described in Shupe et al., (2012). The Doppler velocity variance σ^2_{vm} is calculated as:

$$\sigma^2_{vm} = \sigma^2_w + \sigma^2_{vt} + 2cov(w, vt),$$

Equation 2.5

where σ^2_w is the variance due to vertical air motions , σ^2_{vt} are the variance due to the fall speeds of the hydrometeors and the last term is the covariance between the vertical velocity and fall speeds (Lothon et al., 2005). Mean Doppler velocity can also be represented as:

$$\sigma^2_{vm} = \int_{k_l}^{k_s} S(k)\mathrm{d}k = \frac{3A}{2}\left(\frac{\varepsilon}{2\pi}\right)^{2/3}\left(L_l^{2/3} - L_s^{2/3}\right),$$

Equation 2.6

where $S(k)=A\varepsilon^{2/3}k^{-5/3}$ is the turbulent energy spectrum in which A is the Kolmogrov constant (0.5), k is the wave number, L represents the length scales ($L=2\pi/k$) with L_s small 1s motions and L_l larger eddies over 60s averaging time. Shupe et al., (2012) then rearranged Equation 2.6 to give an equation for dissipation rate from the retrievals:

$$\varepsilon = 2\pi\left(\frac{2\sigma^2_{vm}}{3A\left(L_l^{2/3} - L_s^{2/3}\right)}\right)^{3/2}.$$

Equation 2.7

The dissipation rate calculation relies on the presence of hydrometeors to reflect the radar signal and so the retrieval can only be obtained when either liquid or ice is present. During ASCOS hydrometeors were frequently present in the form of ice throughout the full depth of the boundary layer (Figure 2.16) and so a near continuous time-series of dissipation rate ε profiles are available. The dissipation rate is a qualitative measure for atmospheric turbulence and is used here to provide information on the boundary layer turbulent structure.

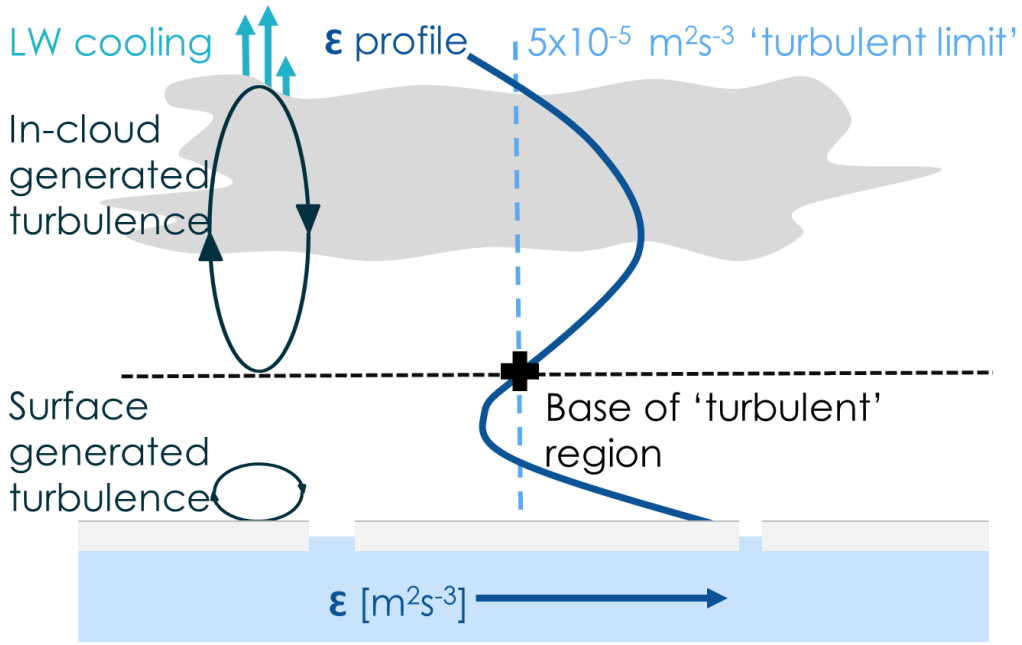

Figure 2.22- Diagram showing the simplified dissipation rate profile and mixed layers of a decoupled cloud layer during ASCOS.

The dissipation rate profiles enable evaluation of the depth of the cloud-mixed layer. The cloud-mixed layer being defined as the depth to which the cloud driven turbulence penetrates down into the boundary layer. Turbulence is a continuum but for practical purposes a definition of when turbulence is no longer 'significant' needs to be defined. Here we have defined $\varepsilon_{min} = 5\times10^{-5}$ m^2s^{-3}, a dissipation rate coincident with that in the region around cloud top. Cloud top being the point at which turbulence becomes non-significant as mixing rapidly drops away with altitude, suppressed by the stability of the temperature inversion. The ε_{min} threshold of 5×10^{-5} m^2s^{-3} was also used by (Shupe et al. 2012) in their studies of cloud turbulence during ASCOS.

Decoupled conditions, according to the ε_{min} criteria, are classed as those where the turbulence generated by in cloud processes does not penetrate far enough down into the boundary layer to meet the layer of surface generated turbulence (Figure 2.22). The 'gap', where the dissipation rate is under ε_{min}, between the two turbulent layers results in inhibited transport between the surface and cloud, rendering the layer decoupled. The cloud-mixed layer is defined as decoupled if ε_{min} lies at or above 195 m, which is two averaging levels above the minimum MMCR retrieval height. The 195 m level ensures that the analysis is only carried out on layers that are clearly separated, according to ε_{min}, from the surface turbulent layer. The base of the cloud-mixed layer is taken as the height at which ε first drops below ε_{min} underneath cloud top. The depth of the mixed layer being the difference in height between cloud top and the height of ε_{min}.

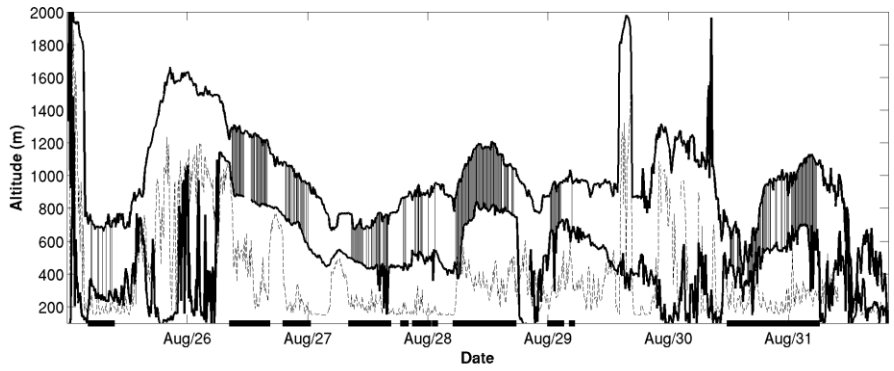

Figure 2.23 - Illustration of the times used during analysis, black vertical marks along the x-axis and vertical lines in the cloud layer (cloud top and bottom are black solid lines and mixed layer cloud base dashed line).

2.5 Data quality control

Observational data can be complex to interpret as many different factors interact with each other and so narrowing down the cause of any shift in an observed value is difficult.

To reduce the number of possible interactions and influences on the cloud-mixed layer, only periods with a single layer of mixed phase stratocumulus cloud were used. Cloud above the stratocumulus layer will alter the incoming and outgoing radiation at cloud top and cloud underneath the stratocumulus

layer will influence the boundary layer turbulent structure. Periods with only a single cloud layer enable a more direct comparison between the depth of cloud driven turbulence and the cloud properties.

It is necessary to select decoupled conditions for analysis on the depth of the cloud mixed layer. Using decoupled conditions ensures that we have a true picture of the depth the cloud driven turbulence extends. Decoupled conditions allow the full possible depth of the cloud mixed layer to be realised, where as the cloud mixed layer from coupled conditions may be artificially shallow as the depth the turbulence can reach is limited by contact with the surface.

The primary method used to determine the mixed layer depth and if the period is decoupled in the ε_{min} turbulent threshold, so periods where the dissipation rate data was compromised were not used. Primarily data was flagged as compromised where the MMCR data failed due to lack of hydrometeors and/or the signal to noise ratio was too high. An example of a period flagged as unreliable for ε values is the morning of the 27th of August (Figure 2.19) where there is a block of 'missing' data (white colour) under roughly 400 m due to the lack of hydrometeors. The gap in the data results in an incomplete turbulent profile causing uncertainty around the derived depth of the cloud-mixed layer. The uncertainty compromises the results from the periods affected and so they will not be used in analysis of the cloud-mixed layer depth. There is only a small portion of time during the week of analysis that is affected by this issue and so the removal of theses times is not likely to bias the results.

Periods where the top or base of the cloud layer could not be reliably determined were also flagged and not included in the data set analysed. The removal of periods with an uncertain cloud base typically consisted of occasions of instances of significant precipitation or ground fog where the accuracy of the ceilometer could not be guaranteed.

Out of the 984 averaging periods 273 fulfilled the requirements for reliable, single layer, decoupled conditions (

Figure 2.23). The LWP and IWP values used are the liquid and ice water concentrations summed up between cloud base and cloud top from the radar profiles, so as to not include lower level fogs/mists or higher level ice. The mean LWP for the selected periods is lower compared to the mean for the

entire week with accompanying lower standard deviation. The cloud layer is also thinner and lower in the data subset analysed than that for the entire dataset. There is overlap between the two datasets and the decoupled data set is not significantly distinct from the week as a whole. It would not be unexpected to find that there is a difference between the decoupled and coupled clouds. The hypothesis is that the transport of water vapour and aerosol from the surface would be different between the coupled and decoupled cases, influencing the potential for the formation of cloud ice and water droplets.

A comparison of the surface temperatures and low level wind speeds show that there is no wide difference in meteorological conditions between the subset of data and the entire week (Table 2.2).

2.6 Decoupling criteria comparisons

The decoupling criteria of ε_{min} is a relatively recently developed criteria for determining decoupling occurrence and there are few other studies where the observations needed to calculate it are available and as such is it not widely used. It is therefore reasonable to compare the definitions and occurrence of decoupling used by other studies with the ε_{min} criteria to evaluate the validity of any comparisons in this or future work.

The dissipation rate data gives a near continuous view of the turbulent conditions throughout the entire boundary layer during ASCOS. The dissipation rate will enable us to directly examine the relative changes in turbulence and use our own classification of coupling directly from the turbulence measurements. In other studies, where such direct measures of turbulence are unavailable, other measurements and ways of classifying conditions as coupled or decoupled have been used. Examples of other measures of decoupling include subjective analysis of discontinuities in the potential temperature and humidity profiles (e.g. Birch et al., 2012 and Soloman et al., 2014) or analysis of other derived quantities such as the lifting condensation level (LCL) as used by Jones et al., (2011).

According to the ε_{min} periods classified as coupled or decoupled are generally grouped together. During most of the extended periods of decoupling there

are a few points classed as coupled present but the decoupled state remains dominant. The ε_{min} decoupling criteria and the LCL decoupling criteria are in broad agreement over which periods are likely to be coupled. There is more disagreement between decoupled classification periods. The discrepancy is not unexpected as it will take time for the temperatures to adjust in line with the dynamically driven mixing. The LCL is not as responsive as the ε_{min} criteria to changes or highly variable conditions. An example of the disagreement between the LCL and ε_{min} is a period from late 27th August to early on the 28th August (Figure 2.21). Chiefly classed as coupled in the dissipation rate data but only seen in part in the LCL data. The LCL heights show a series of sharp spikes that peak near cloud base but the LCL appears mainly to suggest the period is decoupled. However the dissipation rate data from this period is interspersed with brief instances of decoupling giving some agreement that the coupling conditions are intermittent.

	Max		*Min*		*Mean*		*STD*	
	All	sub	All	sub	All	sub	All	sub
LWP [gm^{-2}]	271	116	0	0	52	48	36	24
Cloud top [m]	2030	1309	95	451	1000	979	317	210
Cloud base [m]	1485	962	0	150	466	615	221	186
Windspeed [ms^{-1}]	6.1	4.9	0	0.1	2.8	2.6	1.3	1.2
T_{surf} [K]	272.3	272.0	263.7	267.1	271.0	270.7	1	0.9

Table 2.2- The maximum, minimum, mean and standatd deviation of LWP, cloud top, cloud base, surface wind speed and surface temperature for the entire Stratocumulus ASCOS period (All) and the subset used in analysis (sub).

According to the ε_{min} threshold criteria 68.8% of the period from the 25th August to the 1st September was decoupled. The Jones et al., (2011) LCL decoupling criteria classes 68.6% of the period as decoupled. The LCL decoupling index is positive, indicating some degree of decoupling, during 88.9% of the period. Birch et al., (2012) , Shupe et al. (2013) and Sotiropoulou et al., (2014) all classed the majority of the ASCOS period as decoupled. There is not complete agreement between all the classifications as to exactly when the cloud layer is decoupled, but there is a broad agreement as to the general timing of predominantly decoupled periods and the amount of time

spent decoupled. The comparisons between different measures of decoupling occurrence indicates that the results gained from analysis of decoupling using the ε_{min} decoupling threshold will be consistent with those from other methods of diagnosing decoupling.

2.7 Shape of profiles during decoupled single layer periods

The shape of the profiles of dissipation rate, specific humidity and potential temperature are indicators of the thermodynamic behaviour and structure of the boundary layer. The shapes of the profiles during the decoupled single cloud layer periods provides information about the impact of decoupling upon the boundary layer as well as the effectiveness of any transport between the cloud and surface mixed layers. The ice and open water surface potentially being a key source of CCN and moisture for the cloud in the Arctic boundary layer, particularly so during the summer when transport of CCN and IN to the Arctic boundary layer via advection is limited (Mauritsen et al., 2011). The profiles were normalised in height to provide a consistent view of the sub-cloud-base boundary layer structure with relation to the surface, mixed layer base (ε_{min} turbulent threshold) and cloud base. The dissipation rate profile between cloud base and top was also normalised to give a full picture of turbulence throughout the boundary layer.

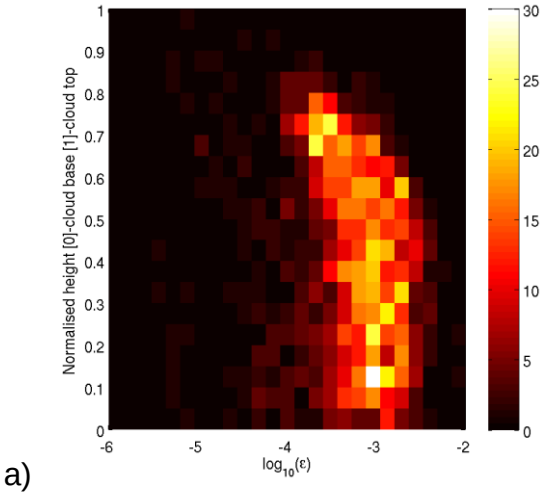

a)

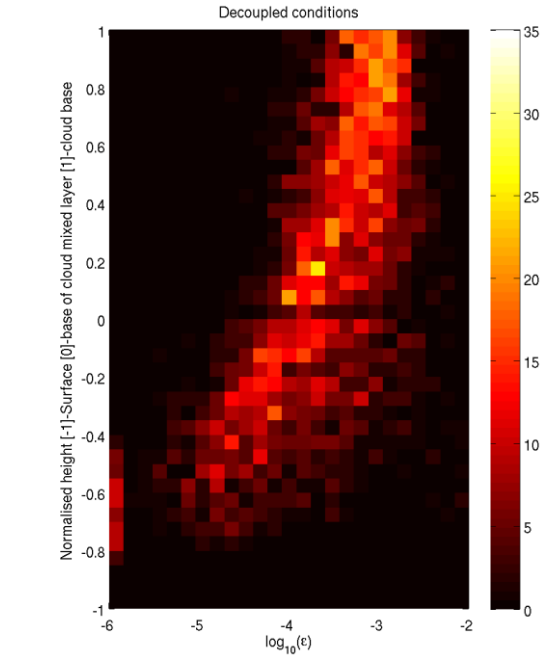

b)

Figure 2.24- Dissipation rate (log_{10}) frequency density for decoupled cases during the ASCOS stratocumulus period (colour scale), normalised in height with respect to a) cloud base (0) and cloud top (1) and in b) the surface (-1), base of the cloud mixed layer (0) and cloud base (1). Figures limited to log_{10}(-6) with values under this level seen as a cluster on the lower limit of the x-axis.

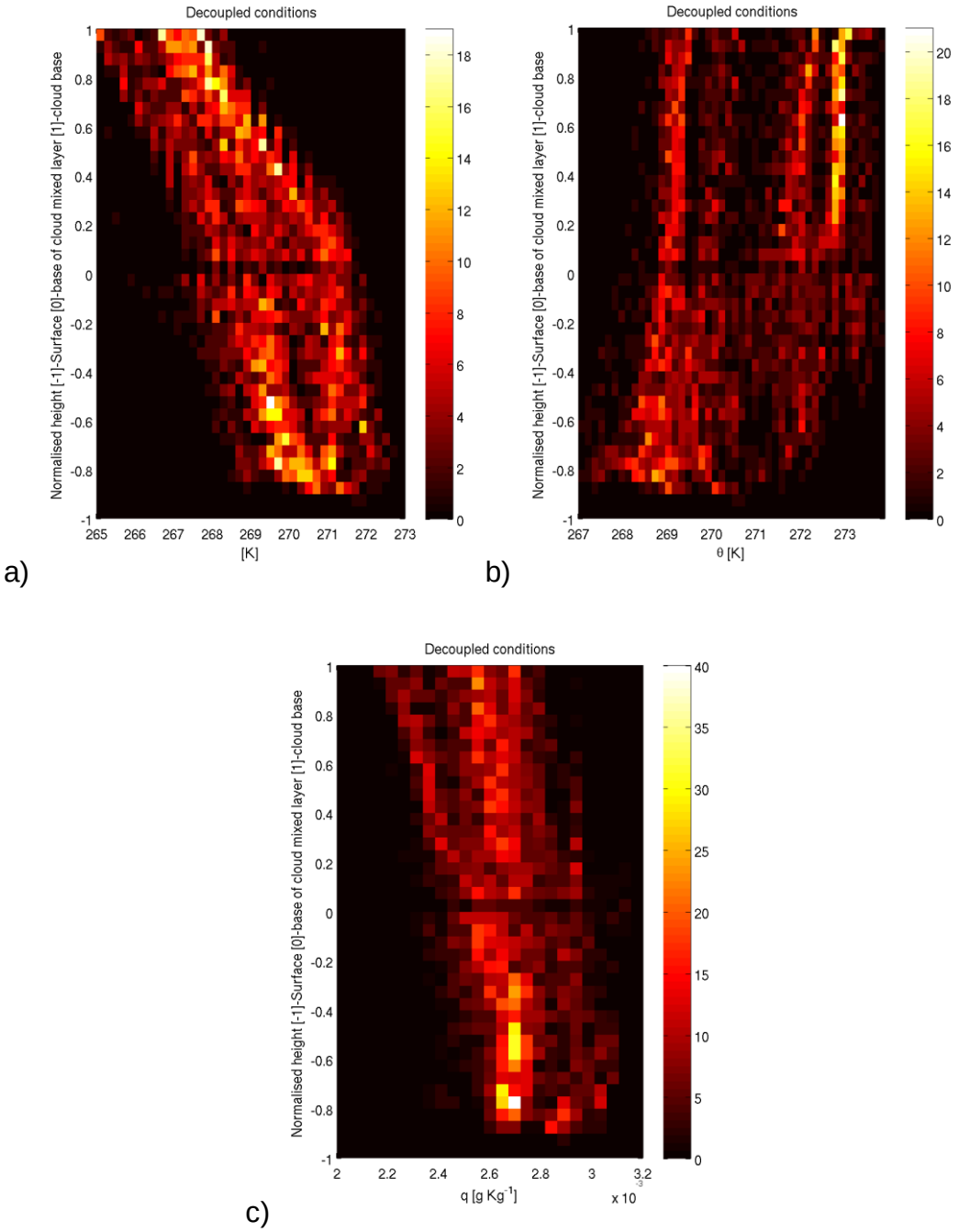

Figure 2.25 - Frequency density profile plots for a) temperature (K) b) potential temperature (K) and c) specific humidity (g Kg^{-1}). Y-axis values indicate the normalised heights of the surface (-1), base of the cloud mixed layer (0) and cloud base (1).

In-cloud dissipation rate can be seen to increase moving down from cloud top, reaching a steady level roughly half way through the cloud (Figure 2.24a). As well as dissipation rate strength, scatter also increases down from cloud top with the range of values remaining fairly consistent from mid-cloud to cloud

base. The range of the dissipation rate strengths remains constant in the lower half of the cloud. Under cloud base, the ε_{min} turbulent threshold stays at the strength of the dissipation rate in cloud for two thirds of the way down to the altitude of turbulence minimum threshold (Figure 2.24b). In the bottom third of the turbulent sub-cloud layer dissipation rate strength steadily drops off down to the value of the ε_{min} turbulent threshold, mirroring the rise in dissipation strength in the top to middle of the cloud layer. From the base of the cloud-mixed layer to the lower limit of the radar retrievals the turbulence quickly drops off (note the log scale in figure) with a wider range of scatter than seen in the cloud and sub-cloud turbulent layers. The lower x-axis boundaries are capped at $\log_{10}(-6)$ giving a cluster of higher frequency points at the edge of the plot in the surface layer indicative of the number of points with values lower than that of the axis limit. Note that the turbulence data does not reach all the way to the surface in the plot as the first viable range gate from the remote-sensing instrumentation is at 100m, giving rise to the gap in the turbulence data near to surface.

The dissipation rate frequency profile shape is consistent with work by Sedlar and Shupe (2014) who looked at the vertical motions in the Arctic stratocumulus topped boundary layer. Turbulence is generated in the top portion of the cloud layer, by downdrafts generated by LW cooling, which lead to a peak maximum in vertical motions in the lower portion of the cloud layer. The mixing extends down into the sub cloud layer and the decrease in turbulence occurs as the down drafts weaken. Turbulence is a continuum and does not just cease under the height ε_{min} but the steadily decreases in magnitude towards the lowest height of the turbulent retrieval.

Birch et al. (2012) and others (e.g. Nicholls and Leighton, (1986) and Sotiropoulou et al. (2014)) used temperature profiles as a way of determining if the cloud layer is decoupled. In the subset of decoupled periods it is expected that there would be a change in the gradient of the temperature profile at the level of ε_{min} turbulent threshold. There is a wide range of scatter in the potential temperature at all levels of the profile (Figure 2.25b). Rising potential temperatures are seen from the surface up through the surface mixed layer, indicating stable conditions under the cloud mixed layer base (Stull, 1988). There are several clear separate profile groups in the potential

temperature probability distribution profiles above the turbulent threshold up to cloud base (Figure 2.25b). The separate vertical temperature profile clusters in the cloud mixed layer are the profiles of the cooler potential temperature conditions later in the week and the warmer profiles from conditions at the start of the week. The separate temperature profile clusters exhibit a constant potential temperature with height, indicating that the layer under cloud down to the dissipation rate threshold is well mixed. The change in gradient of both the potential (Figure 2.25b) and observed temperature (Figure 2.25a) profiles occurs at the height of the ε_{min} turbulent threshold, which adds confidence that the dissipation rate classification of decoupling is robust as it is consistent with temperature indications of decoupling.

The overall trend of the specific humidity during the decoupled periods is for higher humidity levels in the sub ε_{min} layer with humidity levels decreasing from the base of the mixed layer to cloud base (Figure 2.25c). Specific humidity peaks in the bottom half of the surface layer with a decrease in humidity with height up towards the ε_{min} threshold. In the cloud mixed layer there then continues to be a slight decrease in specific humidity towards cloud base up from the ε_{min} level.

The steady decrease of specific humidity above the ε_{min} threshold in the cloud mixed layer indicates that although transport of moisture from the surface does occur it is inefficient during decoupling. The inefficient transport of water vapour during decoupling is further evidenced by the humidity peaks in the surface layer. The layers of 'trapped' water vapour are seen in the plots of the time series of specific humidity (Figure 2.18) which shows peak concentration half way under the ε_{min} cloud mixed layer. The peak of specific humidity in the surface layer during decoupling is consistent with Tjernstrom (2007), who found peaks in humidity in the surface layer during the ‘night’ when surface and cloud layers were decoupled which subsequently dispersed as the cloud and surface layers re-coupled during the day.

The shape of the humidity profile illustrates the potential impact of decoupling upon the efficiency of mixing from the surface layer to the cloud layer. Taking the shape of the specific humidity profile as a tracer for the shape of other surface sourced properties, such as CCN and IN, decoupling would act to

suppress transport to the cloud layer from the surface. The transport of CCN and IN from the surface is thought to be particularly important during the summer period when the formation of cloud is limited by the number of CCN particles (Birch et al., 2012).

2.8 Cloud-Mixed-layer depth Variance With Cloud properties

2.8.1 Geometry and liquid water path

The cloud-mixed layer depth (MLD) derived from the dissipation rate data was compared to cloud top and depth and found to have strong positive correlations (Figure 2.26a,b).The strength of the correlation between cloud geometry and cloud mixed-layer depth is dominated by the fact that the top of the cloud layer is also the capping height of the total boundary layer (r^2 for cloud top vs MLD is 0.85). The MLD cannot exceeded the height of the boundary layer, minus the height used to decide if the surface and cloud mixed layers are coupled, this relationship imposes an upper limit on the absolute value of a MLD for a given boundary layer/cloud top height. Cloud depth and MLD exhibit a clear positive relationship (r^2 of 0.46) at cloud depths of under 300 m, over 300 m the scatter increases (Figure 2.26b). At cloud depths above 300 m the gradient of increase in cloud depth with MLD reduces. It is unlikely that cloud depth itself is causal of the changes in MLD but rather the coincident variation in the cloud microphysical and thermodynamic properties with cloud depth e.g. cloud liquid water concentrations.

Normalisation of MLD with cloud geometry was considered but rejected as unsuitable. When decoupled the cloud layer does not ‘feel’ the surface and as such the distance from cloud base to the surface is essentially irrelevant. The normalisation of MLD with cloud top was tested and increased the scatter of data rather than collapsing the data down, which is indicative that it was not applicable. The strength of the correlation between cloud top and MLD is no doubt partly due to the geometric limits but not all of the correlation can or should be dismissed as false. Higher cloud tops are associated with both cooler cloud top temperatures and deeper clouds in this data set. Deeper and higher cloud layers are also correlated with higher liquid water path values

(Figure 2.26c,d) which in turn are linked to higher levels of LW cooling (Lilly, 1986). The factors mentioned here that could cause a change in the cloud MLD, (LWP, temperature and cloud depth), are all correlated with a higher cloud top so a strong relationship between cloud top height and MLD is not unexpected.Analysis of the LWP variation with cloud top height (Figure 2.26d, r^2 of 0.47) shows lower LWPs are associated with lower cloud tops so there may be some scatter related to geometry. It is unlikely that cloud top is a dominant cause of correlation as the overall relationship of LWP and cloud top height is weak.

Cloud depth and LWP are closely correlated in the ASCOS data set, r^2 of 0.69 (Figure 2.26c). Birch et al (2012) also noted that the LWP during ASCOS not only varies by increasing liquid water concentration but also by variations in cloud depth.

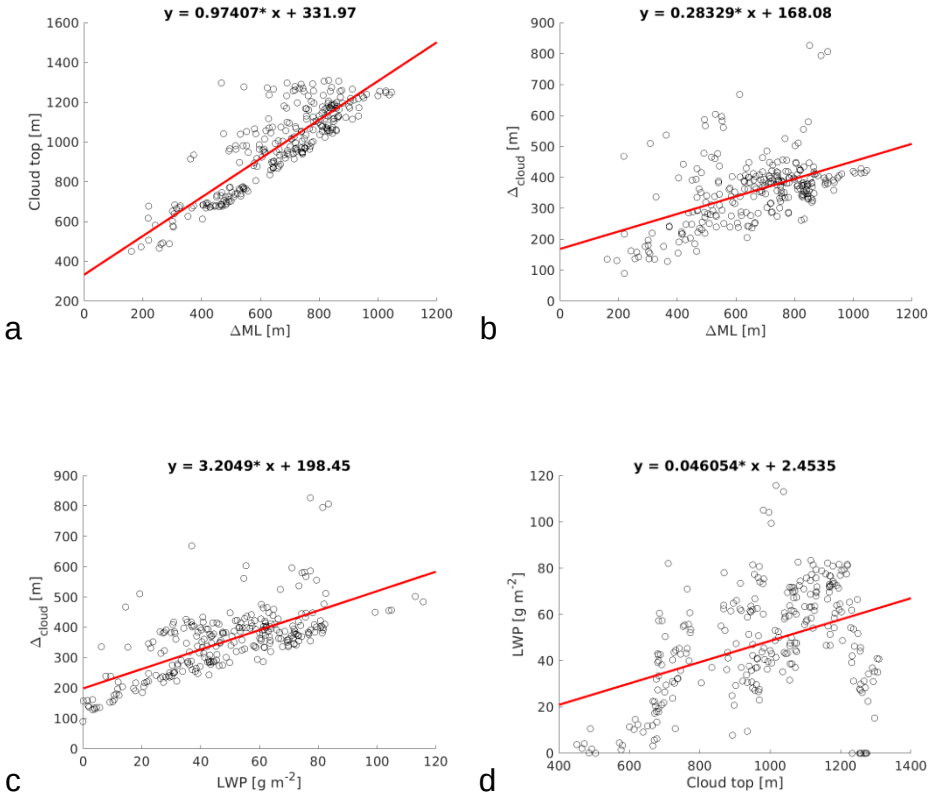

Figure 2.26 - Mixed layer depth vs a) cloud top height (r^2 - 0.85) and b)cloud depth (r^2 - 0.46). Liquid water path vs c) cloud depth (r^2 - 0.69) and d)Cloud top (r^2 - 0.47). Points are the individual 10 min points from the decoupled data subset.

The very clear positive correlation between LWP and cloud depth, is due to the fact that the main variation in LWP is not caused by higher liquid water concentrations over a similar cloud depth but by cloud extending over a greater depth (also noted by Birch et al., 2012). Assuming that liquid water content in the cloud layer increases adiabatically the deeper cloud layers will have greater LWP and a greater peak in liquid water content. The assumption of a clear adiabatic liquid water distribution may be false due to the extension of the cloud top up into the temperature inversion and the influence of cloud ice. The possible non-adiabatic liquid water distribution would give rise to an increase in scatter in the relationship between cloud depth and LWP.

Given that both cloud depth and LWP are known to impact cloud dynamics (e.g. Slingo et al., 1982, Curry et al, 1996) and that they are correlated with the height of cloud top the coincidental variation of these parameters must be considered when interpreting the rest of the observational results.

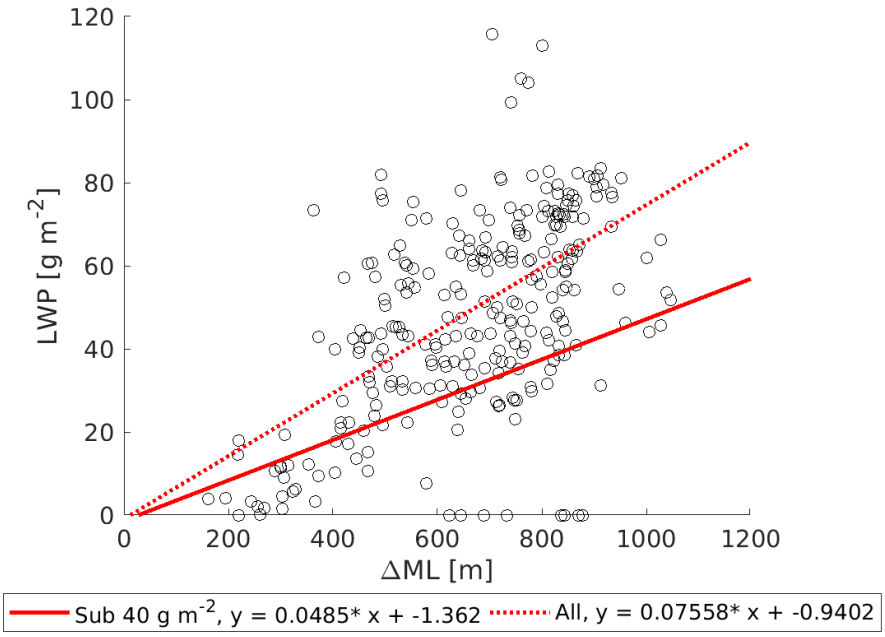

Figure 2.27- Cloud mixed layer depth vs liquid water path for the decoupled subset during the ASCOS stratocumulus period, with sub 40 g m^{-2} and all data fit lines, r^2 - 0.45 and 0.51 respectively.

LWP and MLD (Figure 2.27) show a positive correlation quite clearly up to LWP values of ~40 g m^{-2} at which point the scatter increases, obscuring any clear correlation, though there is still a positive relationship. The LWP of 40 g m^{-2} is the approximate LWP at which a liquid cloud layer switches from acting as a grey to black body and vice versa (Slingo et al.,1982). Below this limiting value changes in LWP will alter the LW cooling and buoyancy driven mixing. Above this limit any subsequent increase in LWP will not directly contribute to an increase in the LW radiation emitted by the cloud. Once radiating as a black body the levels of LW cooling becomes insensitive to LWP variation.

As LW cooling at cloud top is a source of cloud driven turbulence it is logical that MLD would show a relation to LWP when the cloud is not radiating as a black body.

2.8.1.1 Ice water path variation

Ice is a key feature differentiating Arctic mixed phase stratocumulus from stratocumulus at lower latitudes. The influence of ice upon MLD and its relation to cloud geometry and LWP is consequently not covered in mid latitude stratocumulus studies. There is no clear sign of any correlation between ice water path and the MLD (r^2 -0.0042) though there is a slight increase in the higher levels of ice at higher MLDs (Figure 2.28a). Low ice water paths are seen throughout the range of mixed layer depths and a high degree of scatter is observed at all mixed layer depths.

A positive correlation is observed between LWP and IWP (Figure 2.28c, r^2 - 0.34). The majority of the higher IWP ranges are seen at higher LWPs. Though a few high IWP points can be seen over the LWP less than 20 g m^{-2} value (which is close to the uncertainty in the LWP measurements (Tjernstrom et al., 2014). There are complex processes behind ice production but the presence of high specific humidity and liquid water are prerequisites for higher volumes of ice production. Ice forms in Arctic mixed phase stratocumulus primarily from a layer of super-cooled water at cloud top. It follows that the higher the quantity of liquid water the higher the possible amount of ice production, though this grossly oversimplifies the relationship.

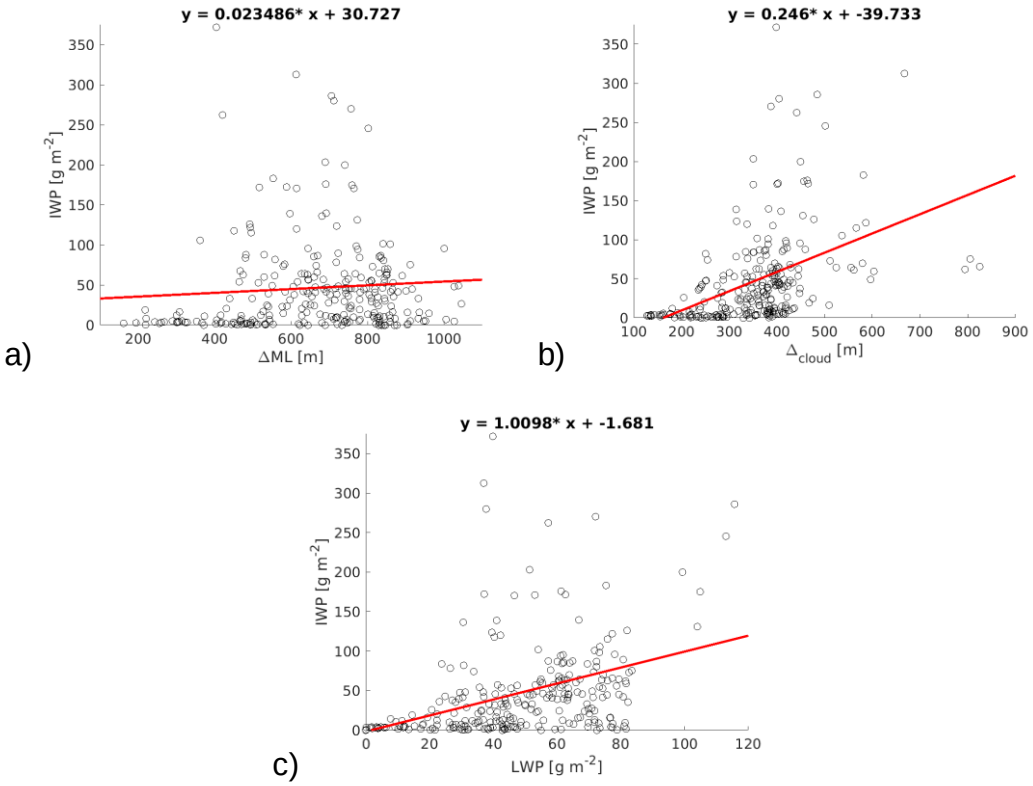

Figure 2.28- Ice water path vs a) Cloud mixed layer depth (r^2 - 0.042), b) Cloud depth (r^2 - 0.39) and c) liquid water path (r^2 - 0.34). Decoupled subset of ASOS data.

Examining the cloud geometry's relation to IWP, cloud depth and IWP exhibit a non-linear positive correlation, r^2 - 0.39 (Figure 2.28b). There is an increase in IWP with cloud thickness up until about cloud depth of 300m after which the range of IWP values increases along with the scatter. The IWP and cloud depth relationship resembles that of the LWP and cloud depth, with higher scatter over 300 m cloud depth.

Ice production is complex and there are many factors influencing the ice water path that may also have a direct impact upon the mixed layer depth. So although mixed layer depth and the radiative properties of the cloud are likely to be slightly impacted by the ice content it cannot be seen in this dataset due to the natural variability of observational data and the limited points available for analysis.

2.8.2 Cloud-Mixed-layer and surface LW radiation

To further test the hypothesis that at low LWPs, when not radiating as a black body, the MLD is dominated by the changes in radiative cooling the LW down-

welling radiation was examined. LW radiative properties of the cloud layer are related to the cooling at cloud top and hypothesised to control the subsequent MLD variations at low LWPs.

Pyrgeometers and pyranometers recording the up and down-welling LW and SW radiation were installed on the ice flow during the three week drift (see Tjernström et al., (2014) for details). They were positioned away from the masts to avoid shadows and interference. The distance of about 400 m of the radiation sensors from the remote-sensing instrumentation will result in some noise due to small spatial variations in the cloud as they will not see exactly the same segment of the sky. These variations are however a minimal source of noise (Shupe et al., 2012) and subsequently the LW and SW radiation can be related to the coincidently measured cloud properties.

The down welling LW radiation (LW_d) at the surface versus the MLD (Figure 2.29) shows a similar relationship to that of LWP against MLD. Up until a MLD of 400-500 m, LW_d and MLD both increase. At deeper mixed layers there is no corresponding increase in LW_d. There are distinct groups of data points at higher MLD with different stable LW_d values at 290 and 300 Wm^{-2}. The separation is caused by variations in LW emissions from cloud bases at different temperatures .

To remove the influence of cloud base temperature, the observed surface LW_d was normalised by the theoretical LW_d emission of the cloud base. The emissions were calculated from the cloud base temperature using the Stefan-Boltzmann law (Stefan, 1879 and Boltzmann, 1884):

$$\boldsymbol{LW_{norm} = \sigma T_{CB}^4}$$

Equation 2.8

Where LW_{norm} is the emitted energy, σ is the Stefan-Boltzmann constant and T_{CB} is the temperature at cloud base. The cloud can be said to be radiating as a black body when the normalised LW_d values are at or above one (Figure 2.30). Values over one are not unexpected. The T_{CB} was calculated by finding the temperature at the nearest temperature retrieval from the scanning microwave radiometer the height of the cloud base from the ceilometer. The

T_{CB} used may not be the exact temperature at cloud base due to the differing resolutions of the instrumentation. Additionally there will be water vapour and temperature variations between the surface and cloud base that may raise the observed emissions above that expected purely from cloud base temperature. It is also important to note that the pyrgeometer looks at the whole hemisphere of sky in comparison to the single point observation of the remote sensing instrumentation, so some small difference is expected.

Where the cloud is observed not to act as a blackbody, mixed layer depth increases with even small increases in normalised LW emissions (Figure 2.30). When radiating as a blackbody (LW_{norm}> 1) there is also a small increase in mixed layer depth with higher normalised emissions. The values of emissivity above 1 occur as there are additional contributions to the flux under cloud base to the surface that are unrelated to the cloud base temperature. The increase in mixed layer depth is associated with a greater distance between surface and cloud base resulting in a higher contribution from water vapour beneath the cloud layer to the observed LW_d.

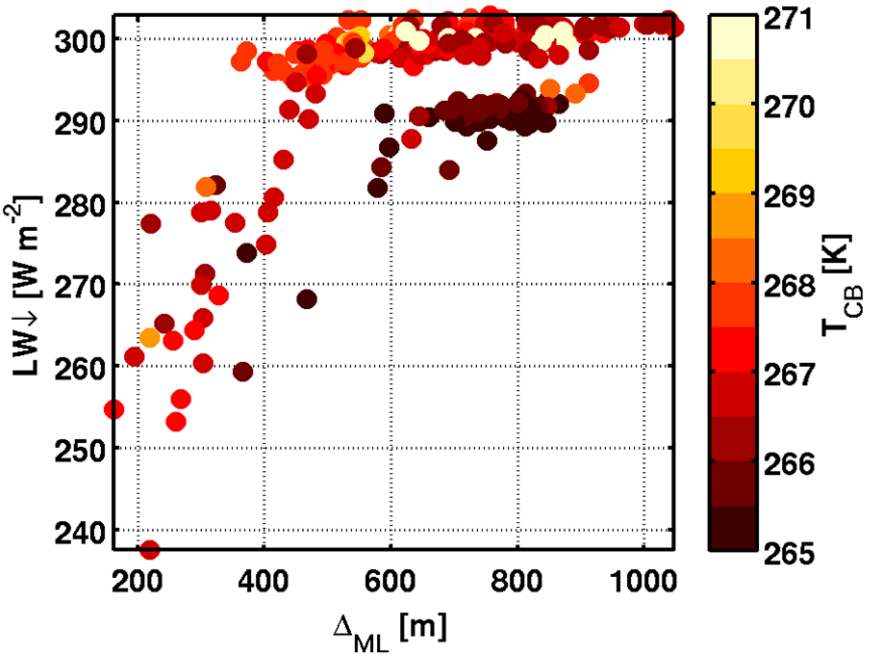

Figure 2.29 - Mixed layer depth vs surface downwelling LW radiation, points coloured by the temperature of cloud base.

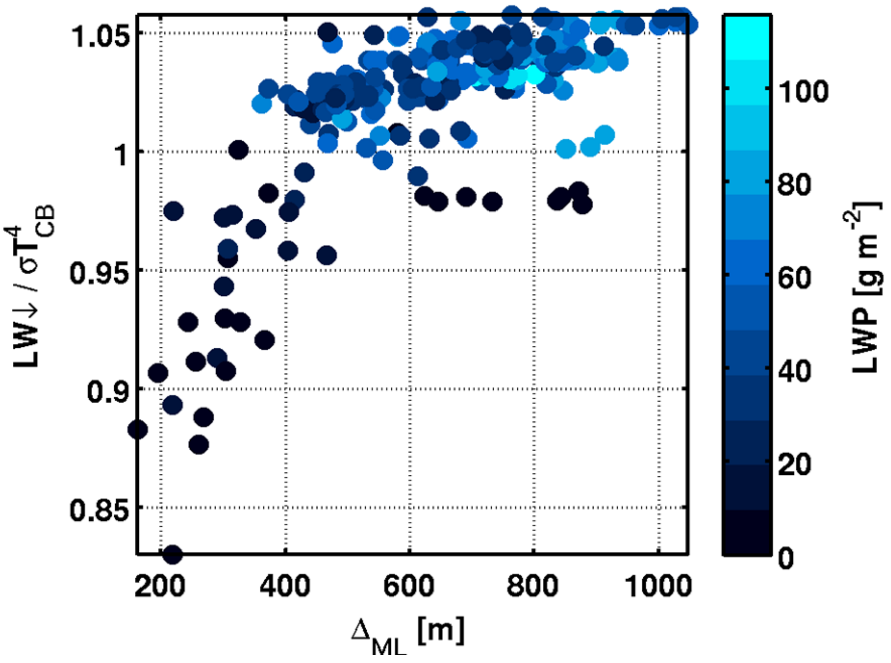

Figure 2.30- Mixed layer depth vs downwelling LW radiation normalised by the LW emmisions from cloud base. Coloured by the liquid water path of each point.

Clouds with normalised LW_d values that indicate they are not radiating as black bodies have LWP values under ~40 g m^{-2} coincident with the LWP at which the MLD correlation changes. Variations in mixed layer depth with LWP can be ascribed to the clouds' radiative properties and amount of radiative cooling. Reduced LWP leads to reduced LW emission which results in lower values of radiative cooling, less turbulence generation with a shallower mixed layer depth possibly resulting in more frequent decoupling.

At low LWP values (where $LW_{norm} < 1$) small changes in LWP result in large changes to the cloud's LW radiative properties (e.g. Sedlar et al., 2011). Variations in LWP can have a disproportionate impact on the amount of radiative cooling and the surface energy budget. Additionally at low LWP values clouds' radiative properties also become more significantly impacted by changes in droplet size and number (e.g. Garrett et al., 2002 and Mauritsen et al., 2011). Whether or not the cloud and surface are coupled or decoupled and if mixing can occur between cloud and surface may then impact the cloud's radiative properties. The amount of transported water vapour, CCN, and IN

available to the cloud feeding back to alter the cloud's LW cooling and subsequent boundary layer coupling state.

2.9 Conclusion

The dissipation rate from the MMCR cloud radar is a valuable dataset for the analysis of the turbulent structure of the Arctic stratocumulus-topped boundary layer. As hypothesised the dissipation rate was an effective data set for determining decoupling of the boundary layer. The dissipation rate coincident with cloud top was evaluated as 5×10^{-5} m^2 s^{-3} and used as the value at which turbulence was classed as 'ineffective'. The height of this 'ineffective' threshold was used to determine the depth the cloud driven turbulence reached beneath cloud base enabling calculation of the depth of the cloud mixed layer depth (MLD). The dissipation rate 'threshold' was used effectively to identify periods of decoupling as times where the dissipation rate threshold was found above the lowest retrieval height of the MMCR.

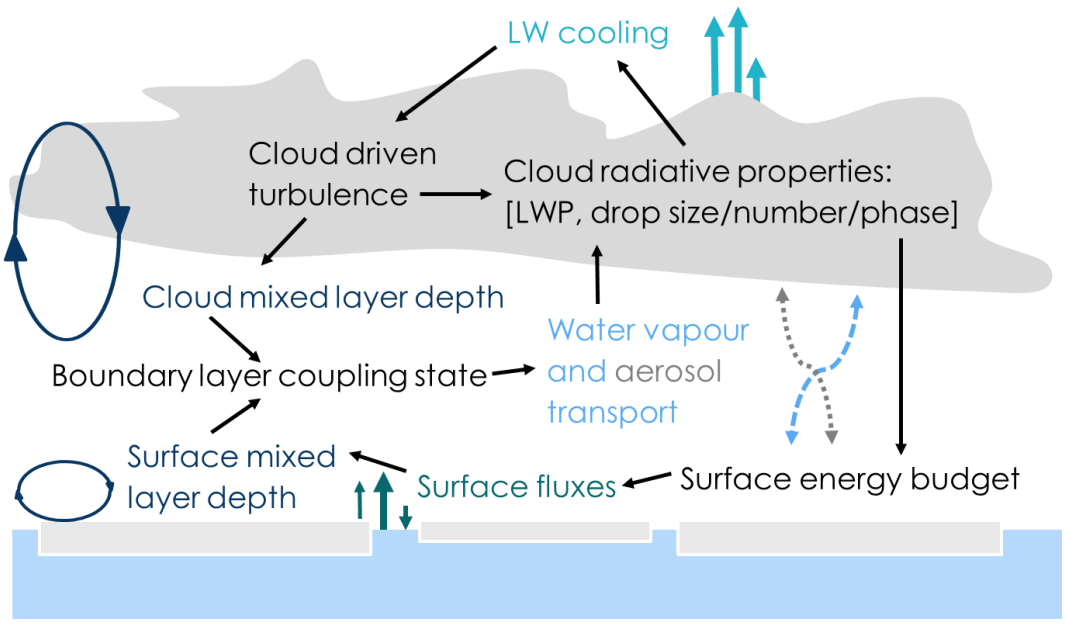

Figure 2.31 - Diagram of the interlinked processes and feedbacks that occur within the Arctic stratocumulus topped boundary layer.

The percentage of time during ASCOS that is decoupled according to the dissipation rate 68.8% is comparable to that of Sotiropoulou et al., (2014). The depth of the cloud mixed layer and periods of decoupling from the dissipation rate were found to agree well with alternative methods of diagnosing decoupling, namely the depth of the LCL and temperature profiles.

The uncertainty in classing the cloud layer as a binary coupled or decoupled is in the exact degree of transport still possible from the surface during decoupling periods, turbulence being a continuum some transport is still likely to occur so a binary view is a very simplistic first step. It is beyond the scope of this thesis but further work on the exact degree of transport from the surface to the cloud layer, and vice-versa, would enable a more definitive measure of the degree of decoupling.During decoupled periods there is a peak in humidity within the surface layer, signifying that vertical water vapour transport is limited during decoupling. Given that water vapour transport from the surface to the cloud is limited during decoupling it is reasonable to suppose that the transport of aerosol is also restricted. Analysis of the cloud geometric and basic microphysical properties with cloud driven mixed layer depth show there are a series of complex interrelated processes to be unpicked (Figure 2.31).

MLD has a positive correlation with cloud depth and height, attributed to the correlation in increased liquid water with greater cloud depth and higher boundary layer top.

Changes in MLD associated with changes to the cloud ice levels are difficult to discern from the data. Higher IWP values are associated with deeper cloud mixed layers but the correlation is likely mostly due to the greater levels of liquid water when there is greater ice and an overall deeper boundary layer.

The hypothesis that the mixed layer depth is related to the clouds physical properties, mainly the liquid water content is proved to be true but only with any real significance at LWP values under 40 g m^{-2}. At LWP values under 40 g m^{-2} the cloud layer was found to not radiate as a black body, with the result that changes in LWP under 40 g m^{-2} alter the clouds emissivity and thus the LW flux at the surface. Cloud turbulence generation is normally dominated by LW cooling at cloud top (Lilly, 1986) so changes in the emitted LW will impact the buoyancy driven turbulence generation. If the cloud is radiating as a black

body it is already emitting at its maximum capacity and so any change in LWP has little, if any, impact on the LW cooling. At the low LWP values where the cloud is radiating as a grey body a small change in LWP will impact the LW emission of the cloud and consequently impact the amount of cooling and turbulence generated within the cloud layer. The dominant control over MLD in arctic mixed phase stratocumulus at LWP < 40 g m^{-2} is the buoyancy driven forcing from alterations to the levels of LW cooling.

The changes to the clouds emissivity due to liquid water variation is likely to have altered the amount of LW cooling at cloud top and the subsequent buoyancy driven mixing. The relation of MLD alterations due to LWP induced LW cooling variations at cloud top is inferred at this point as ASCOS observation only provide a surface value of LW radiation. The changes in cooling at cloud top will need confirming via the use of radiation modelling as the LW flux profiles are unavailable in the observations. Radiation modelling that will provide profiles of radiative flux based on the observations is carried out in Chapter 3.

3 Modelled radiation and turbulence in Arctic Stratocumulus

3.1 Introduction

LW cooling at cloud top has long been identified as a source of turbulence through buoyancy driven motions (e.g. Lilly, 1968). The LW and SW radiation profile is both directly influenced by, and influences, the temperature and moisture profiles throughout the cloud topped boundary layer. The turbulent structure is in turn modified by changes to the buoyancy throughout the profiles driven by the radiative heating profiles.

Investigation into the structure of the radiative heating and cooling of the boundary layer and the corresponding turbulent structure of the boundary layer in the Arctic will enhance our understanding of the controls on cloud driven mixing and coupling.

Analysis of observations from ASCOS showed a positive trend with LWP and LW radiation at the surface and cloud mixed layer depth when the cloud was observed to radiate as a black-body. It was hypothesised that the most likely reason for the relationship between cloud mixed layer depth (MLD) and the LWP and LW radiation was a result of changes in LW cooling at cloud top. A change in behaviour of the cloud layer was observed at the point the cloud would theoretically switch between black-body and grey-body radiative states. The cloud MLD altered with LWP and LW changes for LWP values where the cloud radiates as a grey-body, scatter in the relationship increased at higher LWP where the cloud radiates as a black-body.

3.1.1 Hypotheses

A. In chapter 2 it was found that the surface LW flux and the cloud mixed layer depth were related at LWP values sub 40 g m^{-2}. The hypothesis is that the correlation between LWP and MLD is caused by the variation in LW cooling rates at cloud top, with LW cooling being the dominant control over the generation of buoyancy driven mixing. This is to be tested via comparison of peak LW cooling rates from modelled LW heating rate profiles with the depth of the cloud mixed layer and LWP.

B. Additionally it is hypothesised that the turbulent structure and the distribution of LW heating and cooling in the vertical are related and examination of the profiles will provide insight into the possible other influences of cloud mixed layer depth. In particular interest to this thesis is the behaviour of the turbulence in response to the extension of cloud top into the temperature inversion aloft. The hypothesis is that the extension of cloud top alters the amount of turbulence LW cooling can generate as the temperature gradient in the inversion results in a high level of stability for any cooled air to overcome. Inspection of the LW cooling profiles and the profiles of the turbulence in terms of Richardson number will enable any coincident behaviour to be examined.

3.1.2 Aims

In the ASCOS observational data set there are no observations of cooling rate or LW radiation flux throughout the cloud layer, which would enable clarification of the relationship between cloud driven mixing, cloud coupling behaviour and cloud properties.

Radiation modelling using the available observations of atmospheric and cloud structure, provides a method to obtain profiles of the SW and LW fluxes as well as the LW heating/cooling rates. The radiation profiles can be analysed with the profiles of cloud properties and turbulence to further evaluate the relationship between MLD, turbulence and LW radiation:

- Examine link between radiative cooling and the vertical extent or the cloud mixed layer.
- Examination of the turbulent structure of the boundary layer by using a Richardson number. Relate the Richardson number to the radiative cooling profiles to investigate the links between turbulence and radiative heating.
- Identify dominant factors controlling MLD as well as potential controls on the scatter of MLD at black-body levels of LWP.

3.2 Edwards-Slingo Radiation Model

This investigation uses the Edwards-Slingo stand alone radiation code (Edwards and Slingo, 1996) to model the LW and SW fluxes and heating rates during the ASCOS stratocumulus dominated period. The radiation code and scheme used is the same as that used in the Met-Office Unified Model and the Met Office Large Eddy Model (Ingram et al., 1997).

3.2.1 Radiation code setup and Input data

The code was run using the observed profiles of atmospheric structure as single columns at each 10 min time step. The input data levels were matched to the heights of the MMCR retrievals up to 2 km above which the heights and pressure levels used were those of the radiosonde. The radiosonde measurements were used up to run the radiation profiles up to a height of 10 km. The data used is from the lowest 2 km but the full profile's radiation was modelled to include the influence of the upper layers of the troposphere to minimise sources of error. The radiosonde data is 6 hourly and so the data above 2 km is interpolated between soundings.

The Edwards-Slingo code has an extensive range of input variables, the majority of which are to do with the composition of atmospheric gasses. Only a small selection of atmospheric gas data was available from the surface instrumentation and only O_3 profiles were available from a radiosonde. Any input variables not available were given concentration values of zero throughout the profile depth.

The non-zero data input into the radiation code were are listed here and the source of the retrievals are listed in Table 2.1.

- Temperature, [K]
- Liquid water, Ice concentrations, [kg kg^{-1}]
- Liquid, Ice droplet effective radius, [m]
- Specific humidity, [kg kg^{-1}]
- Surface temperature, [K]
- TOA radiation - set as 1370 W m^{-2}
- Surface albedo
- Latitude and Longitude, [°]

- Day length, [hrs]
- Pressure levels and surface pressure, [Pa]
- Cloud fraction, broken down into ice and liquid fraction. Binary system used - liquid or ice present or not present.
- Solar zenith angle, [°]
- O_3, [kg kg^{-1}]

The profiles set to zero in the Edwards Slingo radiation code are: Mass of sulphur, soot, biogenic aerosol, dust, CFC11, CFC12, CFC113, CH_4, CO_2, Dust, HCFC22, HFC123, HFC134a, N_2O, NaCl,O_2.

The code outputs LW and SW radiative fluxes (W m^{-2}) on the levels of the observations and heating rates (K day^{-1}) at the midpoint between the input observation layers. The bottom layer input to the profiles was at 50 m and not the surface as this is the lowest level of at which all of the atmospheric retrievals are available.

3.3 Model validation and caveats

In order to verify the validity of the simulated profiles of LW radiation comparisons were carried out between the modelled and observed LW and SW radiation. The comparisons will look at the general magnitudes and trends of the LW and SW time series and model.

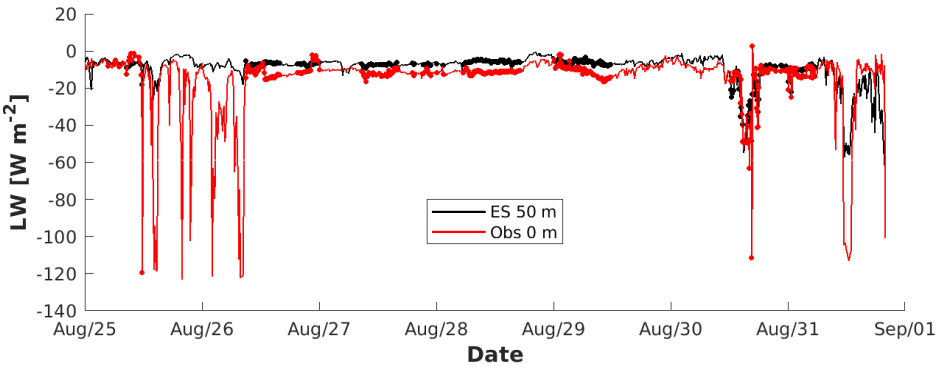

Figure 3.32 – Surface LW flux from the observations (red) and LW flux from the lowest level of the Edwards-Slingo radiation code at 50 m (black), periods used indicated by (.).

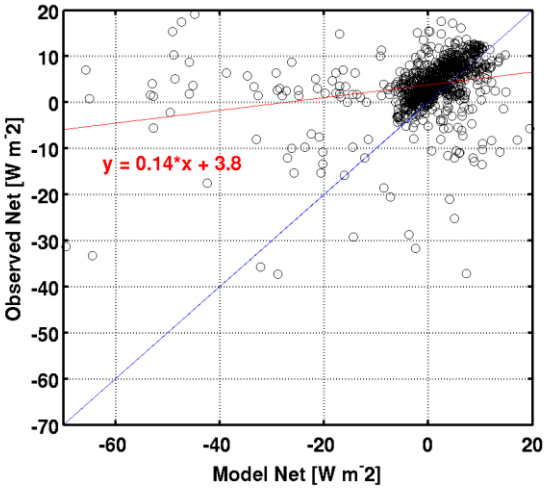

Figure 3.33 - Scatter plot of the observed surface net radiative flux and the modelled 50 m net flux, sum of LW and SW (black circles), the 1:1 line is blue and the best fit line is red.

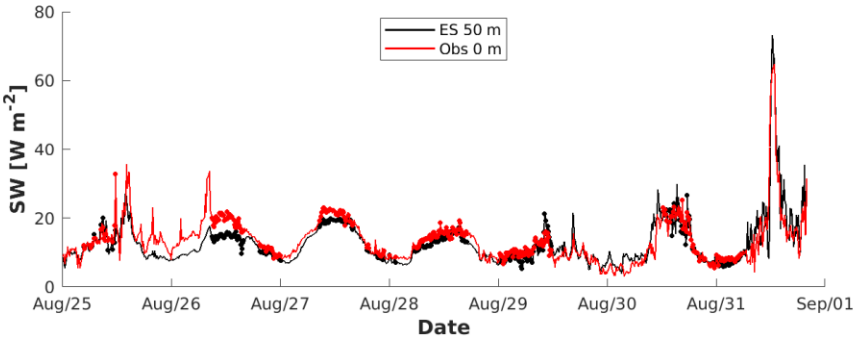

Figure 3.34 - Surface net SW flux from the observations (red) and SW flux from the lowest level of the Edwards-Slingo radiation code at 50 m (black), periods used indicated by (.).

An exact match is not expected. Error will be introduced as data is not available for all the minor chemical and meteorological factors that can interact with radiative transfer (e.g. radiatively active trace gases, organic aerosol, black carbon). Additionally the surface recordings and the data profiles input into the radiation code are from slightly different locations, which will add some scatter in the comparisons.

Looking at the LW net fluxes the ES model LW net flux at 50 m is lower than observed at the surface during nearly all of the time series from 25th to end 31st (Figure 3.32), with only brief instances on the 25th, 26th and 29th where the model LW is higher than the observed. The modelled LW dips far under the

observed LW on the 25th-26th. The period of the 25th-26th is a multilayer cloud period with low level surface fog observed. Instances of surface fog would reduce the LW cooling to space at the surface relative to higher levels in the profile giving rise to a potential discrepancy between surface and 50 m LW values.

Direct comparison between the NET flux model and observations show when observations or model fluxes are less than -20 W m^{-2} the results diverge. Above -20 W m^{-2} the model and observations analysis subset show a linear trend, with the model results offset from the 1:1 line by -3.8 W m^{-2} (Figure 3.33).

The general trends and magnitudes of the LW comparisons are similar enough that there are no obvious large errors or unexplainable discrepancies. The periods used in the data analysis in chapter 2 are consistent with those used in this chapter in the use of only single layer, decoupled clouds. The data subset used here is from when there are clear cloud boundaries and single layer stratocumulus, so that the more complex interactions that cause major discrepancies (e.g. ground fog) are excluded from the analysis.

The model and observations show the same diurnal cycle in SW radiation, and are closely matched in amplitude (Figure 3.34). There are some small differences throughout the week with the model SW flux being predominantly higher as less SW is attenuated at 50 m than at surface. The largest difference between the modelled and observed SW flux is during the 26th with the surface fluxes lower than modelled. As with the LW flux discrepancies, the difference is consistent with the timing of low level fog and high humidity.

The comparison between the observations and modelled SW and LW radiation shows a good agreement with similar general magnitudes and trends. The periods of divergence are explained by meteorological discrepancies between 0 m - 50 m coincident with periods of low level fog. Divergence between observations and model values is where surface fog would result in the higher LW and lower SW radiation values than the 50 m model fluxes. Overall the radiation model is providing a reasonable representation of the radiation profiles during the ASCOS analysis period.

3.4 radiation modelling results

3.4.1 Surface heating rates

The surface heating rates in the Arctic are of interest because the cooling or warming controls the freeze and melt of the ocean and ice surface. The heating rates from the ASCOS ice drift portion examined here cover the end of the summer melt and start of the winter freeze up (Tjernström et al., 2012). The ice drift portion of the ASCOS campaign ended just as the surface began to freeze but longer term observations taken as the *Oden* began to travel back to Svalbard showed the freeze up continued (Tjernström et al., 2012).

The net heating rates show oscillating positive to negative heating rates from 24th until midday of the 30th indicative of intermittent melting and freezing, assuming the 50 m heating and cooling rates are consistent with the surface values. A reduction in LWP and IWP on the 30th led to clear conditions on the 31st and a coincident a rise in the net cooling (Figure 3.35). The net heating is dominated by the LW component (Figure 3.36) but the SW portion is not an insignificant contributor (Figure 3.37). The LW flux drives the most cooling when LWP is low or zero. At the same time low LWP allows more SW radiation to penetrate down to the surface while SW heating acts to reduce the amount of cooling due to LW at the surface.

In the SW heating rates a clear diurnal cycle is apparent of ± 0.1 K day^{-1}, which is about a tenth of the LW heating rates. Due to the SW component a diurnal variation in the net heating rate is observed.

Overall the LW heating rates dominate the net fluxes and the SW is only of real significance when LW is of a similar magnitude..

3.4.2 Time-height series

Time height plots allow examination of the evolution of the entire boundary layer in time, rather than just individual profiles or levels. The analysis of the modelled radiation profiles enables evaluation of the influences and interactions on and between the fluxes and heating rates and their relation to the cloud mixed layer depth and turbulent structure throughout the boundary layer.

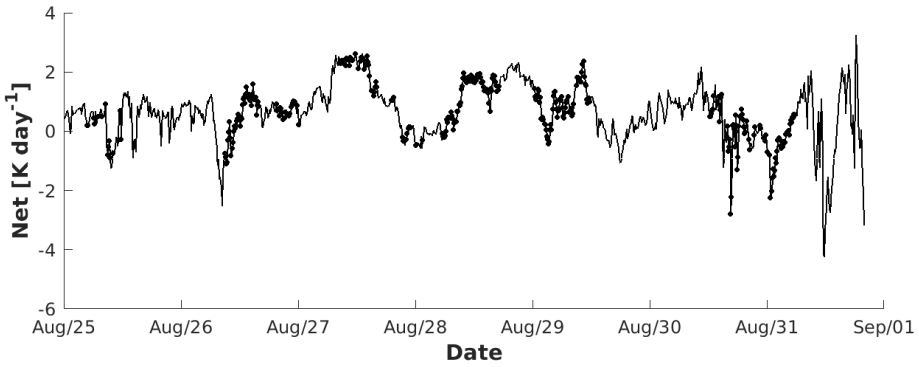

Figure 3.35 - The net radiative heating rate at 50 m height from the Edwards-Slingo radiation model, periods used indicated by (.).

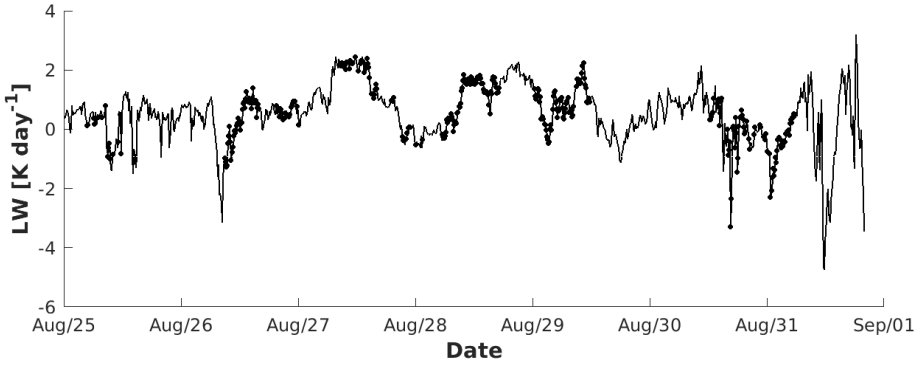

Figure 3.36 The LW radiative heating rate at 50 m height from the Edwards-Slingo radiation model.

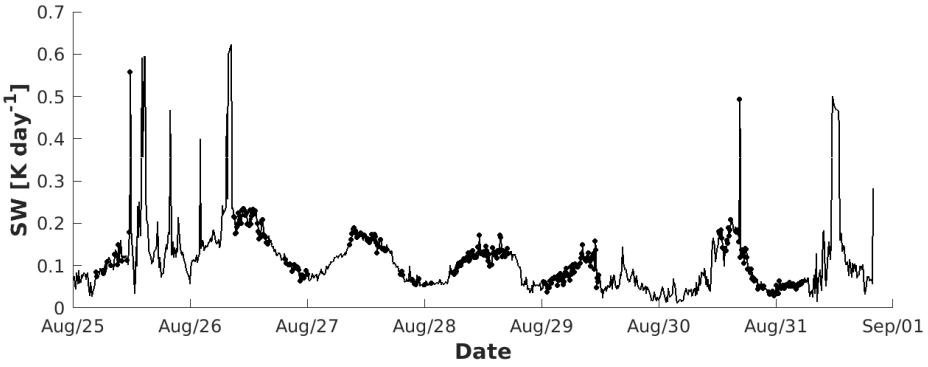

Figure 3.37 - The SW radiative heating rate at 50 m height from the Edwards-Slingo radiation model.

3.4.2.1 Radiative flux profiles

The LW net flux is predominately negative, indicating a dominant upward LW flux, through the majority of the boundary layer. The LW flux becomes less negative under cloud top, with instances of positive (net downward) flux at times within the lower half of the cloud layer (Figure 3.38). A look at the liquid water concentrations (Figure 3.39) shows that the positive LW fluxes are typically located underneath the location of the peak in cloud liquid water content within the cloud. The highest positive (downward) LW flux during the week is observed on the 29th as an Altocumulus cloud, containing liquid water, forms above the Stratocumulus deck. The Altocumulus cloud acts to insulate the Stratocumulus cloud top as the lower cloud is no longer radiating to space.

The range of LW flux values sub-cloud to surface are relatively small, a few W m^{-2} in comparison to the -100 Wm^{-2} and greater values at the top of the cloud layer. Variation in the sub cloud layer LW flux is in the single digit range but the relative differences will play a role in determining the structure of the heating in the boundary layer. Periods with higher level clouds can be seen as streaks of less negative upwards LW fluxes on the late 29th and 30th (Figure 3.38).

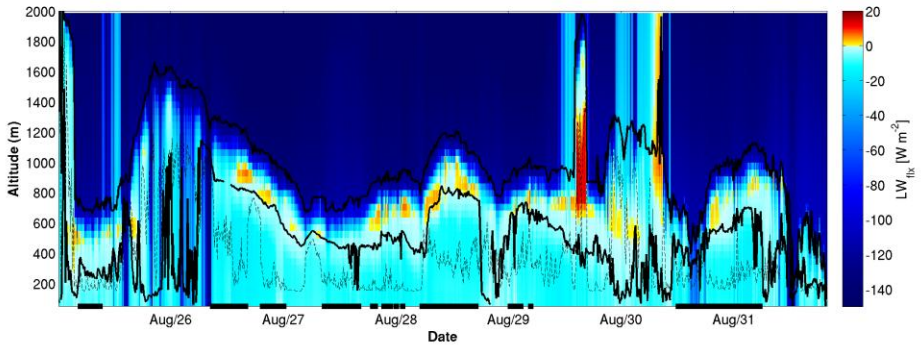

Figure 3.38 - Time height plot of the LW flux from the Edwards-Slingo radiation code. Solid black lines are cloud boundaries and dashed line is the lower limit of the cloud mixed layer from the dissipation rate, black squares on the x-axis are the periods used in data analysis of single layer decoupled periods.

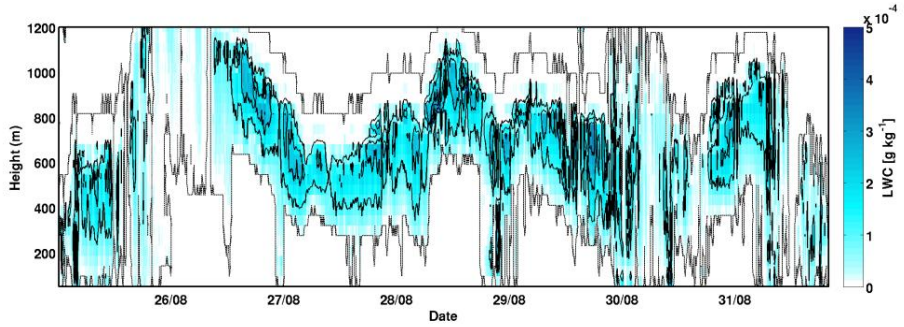

Figure 3.39- Observed profiles of liquid water content during ASCOS 25th to end 31st August.

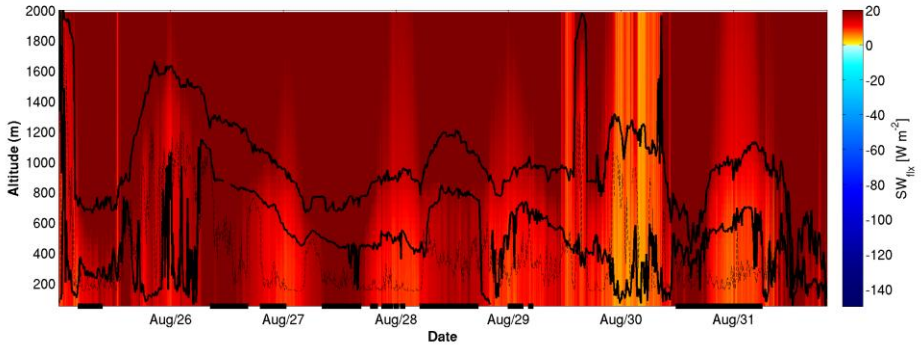

Figure 3.40 Time height plot of the SW flux from the Edwards-Slingo radiation code. Lines as Figure 3.38.

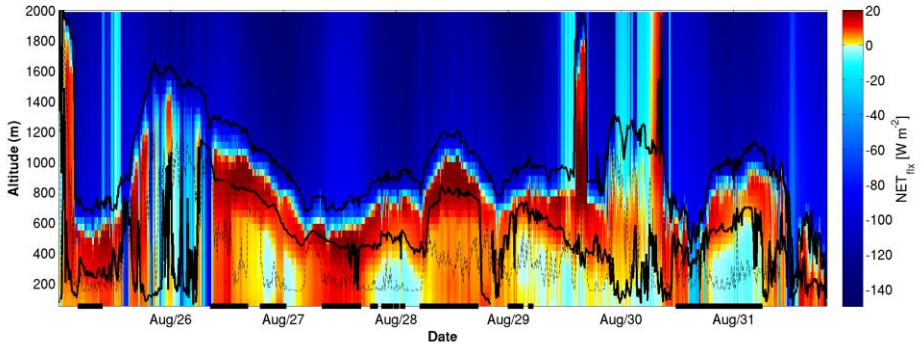

Figure 3.41 Time height plot of the net flux from the Edwards-Slingo radiation code. Lines as Figure 3.38.

ASCOS took place during the Arctic summer and though the sun did not dip under the horizon a clear diurnal cycle is seen in the time series of SW radiation profiles (Figure 3.40). The need for exclusion of periods containing higher level clouds in the analysis periods is seen in as the high level clouds

reduce the column SW flux in the boundary layer by ~10 Wm^{-2} e.g. during the 25th and 29th-30th

The net flux above cloud is dominated by the LW though the SW does show up in a diurnal cycle aloft that is not seen in the LW alone. The top half of the cloud layer is negative indicating a net upward flux. A small but notable step increase in the net flux is coincident with the location of the top cloud boundary. The net flux changes sign roughly a third of the way down the cloud layer at the point where the net up LW flux matches the SW flux (Figure 3.41). The net flux peaks around cloud base. The flux then remains positive for some distance under cloud base during 'night' with slightly negative flux to surface. During the day, where higher SW fluxes reach further down into the boundary layer, positive fluxes reach all the way to the surface. Under cloud base the negative LW values are lower than the downward SW and so the SW component dictates the overall sign and direction of the flux.

The combination of the LW and SW in the net flux results in an enhanced flux into the lower half of the cloud layer and sub cloud. The upper part of the cloud layer and net flux to space is LW dominated.

3.4.2.2 Heating rates

Above cloud top where humidity is higher LW heating rates are near zero. LW cooling rapidly increases downwards from cloud top and peaks at about 50 - 100 m under cloud top (Figure 3.42). Peak LW cooling is coincident with the peak in liquid water concentrations (LWC) in the cloud layer (Figure 3.39). The LW cooling will act to drive turbulence in the cloud layer as the cooled air will become denser than the surrounding air and sin. Cooling in the LW occurs in the top $^1/_2$ to a $^1/_3$ of the cloud layer, with warming in the lower portion of the cloud and beneath. The vertical limits of the warming under cloud base follow the limits of the liquid water profile. The further down into the cloud the more interference the liquid above gives to the direct cooling to space. The layers are essentially adjusting to the temperatures of the layers above and below to try and reach equilibrium. The upper limit of cloud liquid water (Figure 3.39) extends above the region of peak LW cooling (Figure 3.42). Cloud extends into the temperature inversion while the peak in LW cooling is coincident with the height of the peak in liquid water content.

There is a peak in LW warming at the stratocumulus cloud top on the 29th as the altocumulus overhead shields the cloud top from space (Figure 3.42). Cooling at the stratocumulus top halts as the altocumulus appears overhead with the stratocumulus layer instead experiencing radiative heating. The warming at cloud top acts to limit the buoyancy driven turbulence generated by LW cooling as evidenced by with a coincident reduction in dissipation rates. The stratocumulus layer thins during the period the altocumulus is present but quickly rebounds back to previous levels of LWP and cooling after the altocumulus cloud is no longer overhead.

It is important to recall that the time series is not necessarily following the evolution of a stationary cloud layer but that the clouds are moving overhead at the same time as evolving. The quick rebound of the cloud layer is just as likely in this case to be advection of a new section of stratocumulus cloud, unaffected by the altocumulus as opposed to the reformation of the same stratocumulus layer after the altocumulus has dissipated or advected away. It is difficult to say, based on this one instance, how the cloud alters in time due to radiative shielding. The observations do show the impact the shielding has relative to a cloud layer able to cool to space. In the sub-cloud to surface layer LW heating remains close to 0 K day^{-1}, with a typical range of ± 2 K day^{-1} with peak cooling just lower than -4 K day^{-1}.

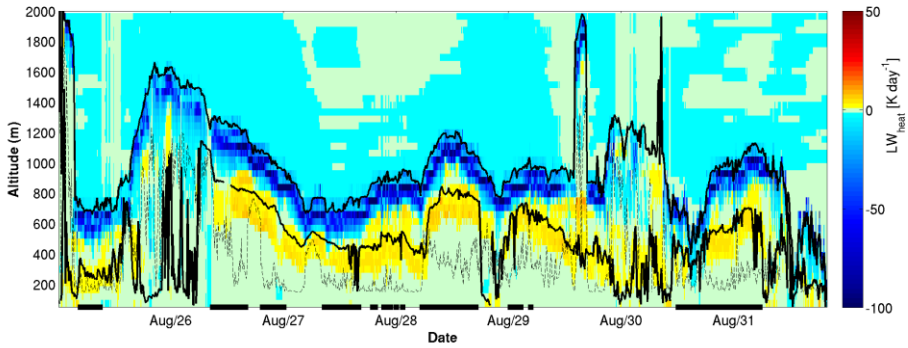

Figure 3.42 - Time height plot of the LW heating rates from the Edwards-Slingo radiation code. Solid black lines are cloud boundaries and dashed line is the lower limit of the cloud mixed layer from the dissipation rate, black squares on the x-axis are the periods used in data analysis of single layer decoupled periods.

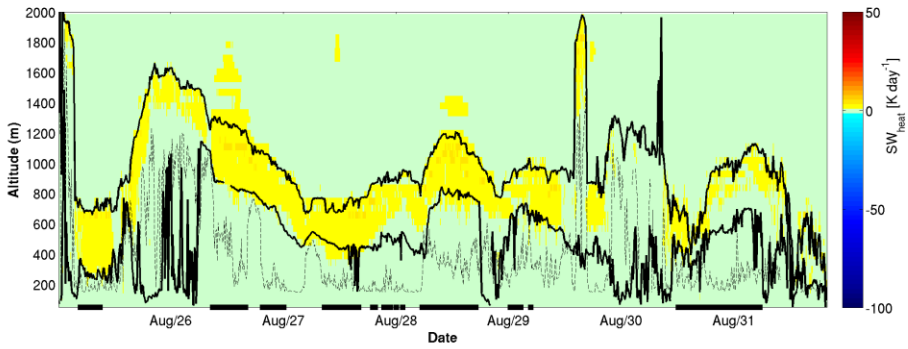

Figure 3.43 - Time height plot of the SW heating rates from the Edwards-Slingo radiation code. Lines as Figure 3.42.

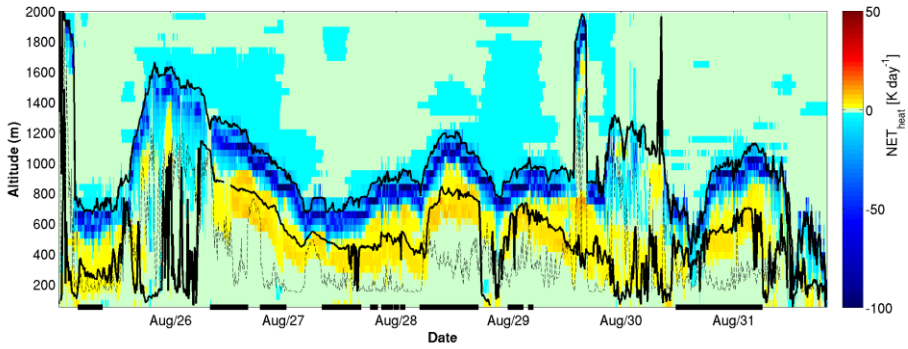

Figure 3.44 - Time height plot of the net heating rates from the Edwards-Slingo radiation code. Lines as Figure 3.42.

SW heating (Figure 3.43) occurs predominantly in the cloud layer and, as the LW cooling (Figure 3.42), peaks in warming coincident with the highest LWC values (Figure 3.39). The SW warming will act to offset any coincident LW cooling. As cooling causes buoyant overturning the SW in this case acts to counter the amount of buoyancy driven turbulence generation. The SW warming peaks at around +5 K day^{-1} and the LW cooling at greater than -100 K day^{-1}. The impact of the SW heating on cloud cooling is likely to be small as the as SW heating peak is significantly less than the LW cooling.

Beneath the peak in LW cooling and SW warming the levels of LW warming are of a similar magnitude to the SW warming. The LW and SW heating and cooling values are similar in the sub cloud layer acting together to produce a net heating of the cloud base and sub cloud layer (Figure 3.44).

The SW heating regions in and below cloud are where there is liquid water present or peaks of humidity. SW adds to the net warming of the immediate sub cloud layer to a greater extent than the layer containing no liquid water underneath. The higher SW heating further above the surface potentially acts to move the temperature profiles towards a more stable layer beneath cloud. The SW heating has a diurnal cycle and peaks during the middle of the day.

3.4.2.3 Modelled Radiative Fluxes vs LWP & MLD

The observed surface fluxes during ASCOS are correlated closely with the LWP and MLD up until the point the cloud radiates as a black-body (see previous chapter). The hypothesis formed is that the MLD is related to the LW cooling at the top of the cloud, which increases with higher LWP values up until the LWP at which the cloud radiates as a black-body. Once the LWP reaches the black-body threshold other factors that influence cloud driven turbulence have the potential to become increasingly significant. The peak positive radiative fluxes for the NET, LW_{net} and SW_{net} were found from each modelled profile. The peak fluxes were compared to the MLD and LWP.

The trend in peak LW flux with MLD and LWP seen in the model data is consistent with the trend in surface fluxes seen in the observational data (Figure 3.45c,d). The LW relationship with LWP is smoother in the modelled data than the observed. The modelled LW fluxes have a smooth trend in peak flux between the LWP values associated with grey and black body radiative states (Figure 3.45d). The pivot point of the transition is consistent for the modelled and observed fluxes at a LWP of ~40 g m^2.

Maximum modelled LW flux and MLD has a similar shape again to the observed LW (Figure 3.45c). The two regimes of grey/black-body are more distinct in the MLD trends than the smooth curve of the LWP with LW radiation.

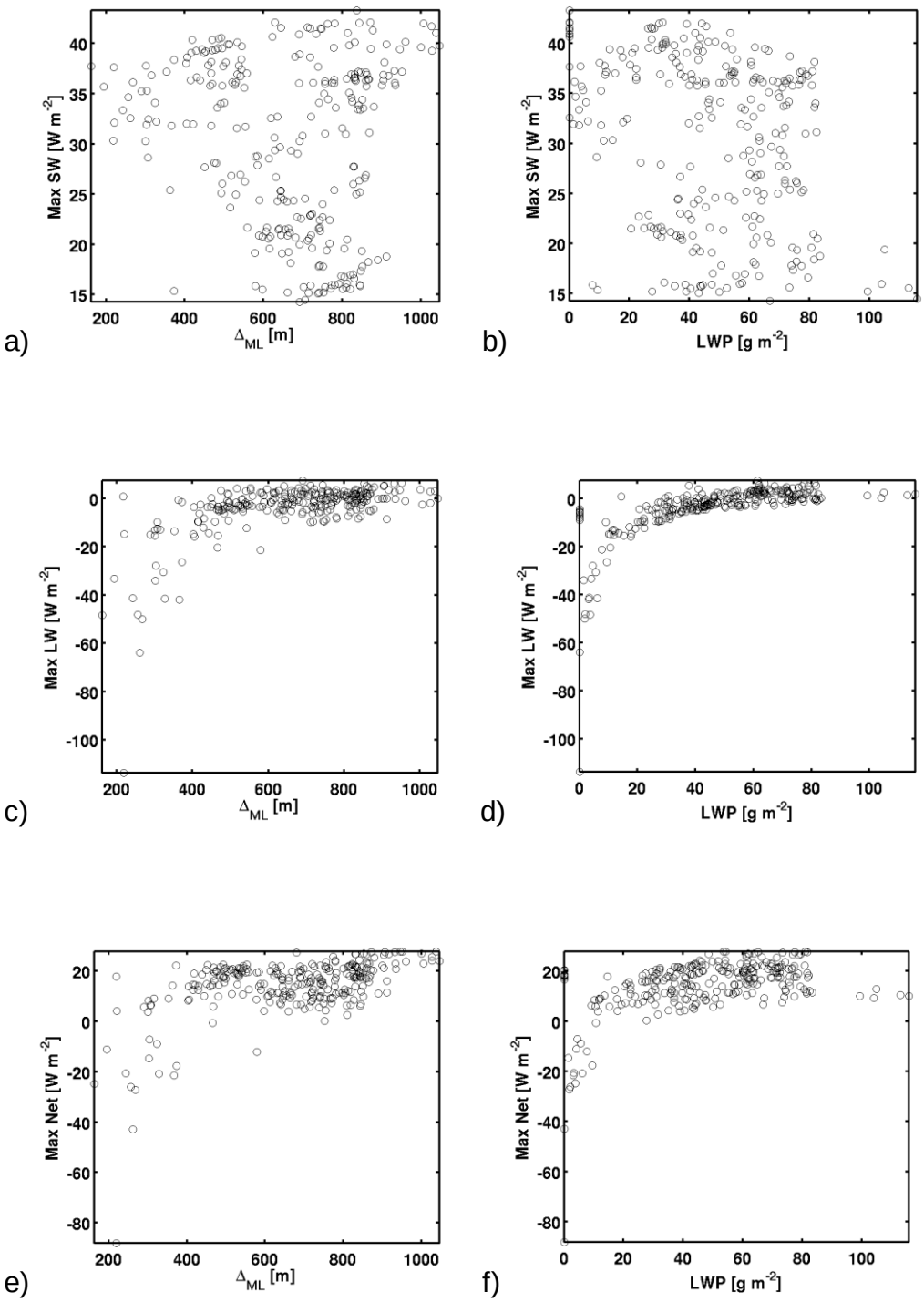

Figure 3.45 - Cloud mixed layer depth vs the Edwards-Slingo modelled peak a) SW flux c) LW flux and e) net flux. Liquid water path vs the Edwards-Slingo modelled peak b) SW flux d) LW flux and f) net flux. For the single layer cloud, decoupled data subset.

Lower MLDs are observed at the most negative LW flux values. The MLD increases up to 400 m from ~150 m with a rise in LW flux from under -60 W m^{-2} up to -15 W m^{-2}. At MLDs over 400 m the MLD rises to over 1000 m with a LW flux rise of ~15 W m^{-2}. The rise in MLD over 400m with LW flux is not due to the black/grey-body transition, so will be to do with the more subtle changes to do with liquid water content and other drivers of turbulence. The small magnitude of the relative changes in LW fluxes at higher MLD and the small sample size makes it hard to investigate subtle relationships from the ASCOS observations alone.

The peak SW flux and the LWP show little direct correlation (Figure 3.45b). For very low LWP (< 40 g m^{-3}) the SW fluxes are predominantly >25 W m^{-2}. From a limited data set it is hard to know if the is more causal or coincidental behaviour, given the influence of the movement of the sun over maximum SW values.

The relationship of the NET flux to the LWP and MLD shows greater scatter than the pure LW relationship (Figure 3.45e,f). The NET flux peak values are mostly positive at the black-body values of LWP. The shape of the net flux LWP and MLD relationship also still shows the shift between black and grey body, as seen in the LW. Overall the net flux's relationship to the LWP and MLD is that of the LW with added scatter from the SW.

3.4.2.4 Modelled peak LW Radiative Cooling

The peak LW cooling from the Edwards-Slingo model is associated with higher LWP (Figure 3.46b) and deeper MLD (Figure 3.46a). The MLD increases by ~200 m from peak LW cooling rates of -20 K day^{-1} down to -60 K day^{-1}. At cooling rates greater than -60 K day^{-1} scatter in MLD increases but there is arguably still a positive trend whereby the lowest boundary of the MLD increases with greater LW cooling. The point at which the scatter in the MLD vs LW cooling increases is the point at which the scatter in the LWP vs LW cooling also increases. The increase in scatter in LWP vs LW cooling is observed to be greatest above 30-40 g m^{-2}.

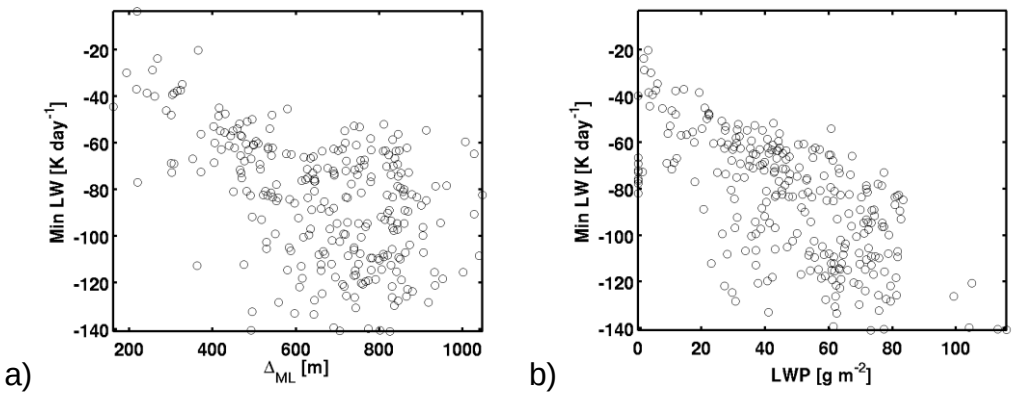

Figure 3.46 - Minimum in cloud cooling from the Edwards-Slingo radiation model against a) Cloud mixed layer depth and b) Liquid water path.

Greater LW cooling is associated with greater MLD and LWP at all levels of LW cooling, not just those LWP values at which changes in cloud emissivity from LWP variation will alter the LW cooling. Scatter in the MLD with LW cooling is greatest above the LWP at which the cloud radiates as a black-body but correlation in MLD with LW cooling is still present. In the grey-body radiation regime changes in LWP dominate the change in LW cooling which in turn alters the MLD. The increased scatter in the LW cooling vs MLD above the point at which the cloud radiates as a black-body indicates that LW cooling is not the only influence on MLD.

Under a LWP of ~40 g m^{-2} changes in LWP alter the LW cooling which in turn alter the MLD. Above 40 g m^{-2} LW cooling is still a driver of buoyancy generated cloud motion but other factors are increasingly influential. The correlation between LW cooling and LWP above 40 g m^{-2} will be due to more complex cloud interactions. Examples of simple interactions that may vary cloud liquid water and MLD correlation include the fact that deeper cloud layers have the potential to have deeper mixed layers and deeper clouds with higher cloud tops and subsequently higher different cloud top temperatures and altered LW cooling. The lack of scatter at the points where the cloud is radiating as a grey-body indicates that there is a clear and dominant relationship between LWP and LW cooling levels and MLD.

3.5 Radiative forcing and Richardson number

A Richardson number (Ri) provides a useful indicator of the turbulent state of the layer of air over which it is calculated. The Richardson number takes into account the balance between the sheer and buoyant forcing upon a given parcel using profiles of the potential temperature and wind to determine the turbulent state of the parcel.

3.5.1 Richardson number calculation

The remote sensing instrumentation deployed during the ASCOS ice drift were used by Dr G Canut to calculate the gradient Richardson number (Ri_g).The Richardson number data has a fixed 10 min by 10 m resolution and the profiles are from 45 m to 1200 m, 1200 m being the vertical limit of the air temperature data available from the 60 GHz scanning microwave radiometer. Although the 1200 m limit will miss out some of the cloud top data during the analysis period all the sub cloud periods we are focused on are captured. The established classical definition of Ri_g in a cloud free environment is:

$$Ri_g = \frac{g}{\theta_v} \frac{\frac{\partial \theta_v}{dz}}{\frac{\partial u}{\partial z}^2 + \frac{\partial v}{\partial z}^2},$$

Equation 3.9

where θ_v is the virtual potential temperature, u and v are the horizontal winds and g is gravity (Brooks et al , 2017). Following the work of Andreas et al., (2005) in the Arctic θ_v can be approximated to θ as the low humidity of the Arctic summer results in minimal water vapour contributions to stability. Brooks et al., (2017) use this approximation to give an equation for calculation of the dry Richardson number Ri_d during ASCOS:

$$Ri_d = \frac{g}{\theta} \frac{\left(\frac{\partial T}{dz} + \Gamma_d\right)}{\frac{\partial u}{\partial z}^2 + \frac{\partial v}{\partial z}^2},$$

Equation 3.10

where T is the air temperature and Γ_d is the dry adiabatic lapse rate. The appropriate equation for Ri calculation in cloudy environments is given by Durran and Klemp (1982):

$$Ri_m = \frac{\frac{g}{T}\left(\frac{\partial T}{dz} + \Gamma_m\right)\left(1 + \frac{Lq_s}{RT}\right) - \frac{g}{1+q_w}\frac{\partial q_w}{\partial z}}{\frac{\partial u}{\partial z}^2 + \frac{\partial v}{\partial z}^2},$$

Equation 3.11

where Γ_m is the moist adiabatic lapse rate, q_s is saturation mixing ratio, L_q is latent heat of vaporisation and q_w is the total water mixing ratio. Depending on local point conditions different dry Ri_d or moist Ri_m number calculations were used. The moist calculation was used when liquid water was detected in the profile. Ice only sections were separated into classes, based on probability distributions of the observed lapse rate. For is ice precipitation under cloud the lapse rate closely approximated the dry lapse rate, and equation 2 was used; for ice within the main body of cloud a moist lapse rate with respect to ice was observed and equation 3 is used with Γ_m defined with respect to ice (Brooks et al., 2017).

3.5.1.1 Richardson number thresholds

The resultant turbulent state and the dominant forcing controlling it is indicated by different threshold values of Ri. Negative values of Ri are associated with turbulent states driven by buoyant forcing, here driven predominantly by LW cooling at cloud top. Positive Ri values are indicative of a stably stratified state with a transition zone between the turbulent and stable states at low positive values of Ri. Classical Ri threshold boundaries are:

- Ri<0 - turbulent,
- 0<Ri<0.25 - thermodynamically stable, turbulent (shear driven)
- 0.25<Ri<1 – indeterminate - the turbulent state depends on past history, turbulence or laminar flow is maintained, but not actively forced
- Ri>1 – non-turbulent, laminar flow.

The gradient Ri is sensitive to the vertical resolution of the profiles from which it is generated (e.g. Tjernstrom et al 2008) and so the validity of the literature thresholds for this data set needs confirmation. To examine the relation of the Ri values and threshold to the turbulence Brooks et al. (2017) looked at the Ri values alongside the vertical velocity variance and dissipation rate values.

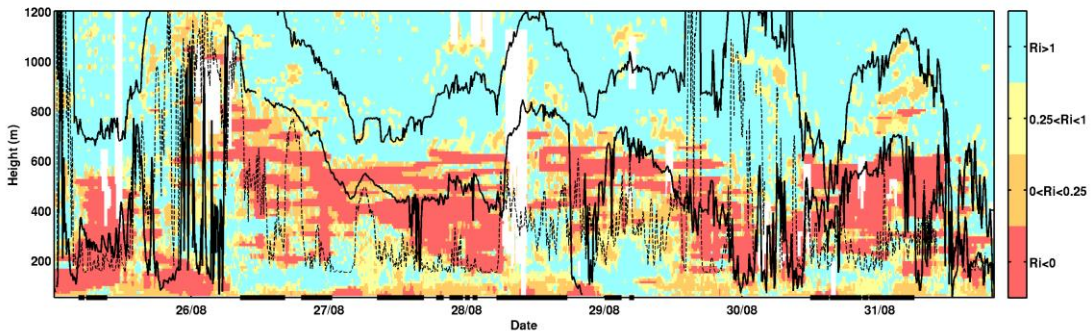

Figure 3.47 - Time height series of the Ri_g classifications (colours). Solid black lines are the cloud boundaries, dashed line is base of the cloud mixed layer derived from the dissipation rate, solid marks on the x-axis are the times of the single layer decoupled periods.

The dissipation rate analysis also confirms that the Ri calculated by Dr G Canut is consistent with respect to the analysis of turbulence already carried out in this thesis. The probability distribution functions of Ri with respect to the dissipation rate is particularly useful because the threshold of 'effective turbulence' used to classify the base of the cloud mixed layer from the dissipation rate is empirically defined in a manner that leaves some uncertainty. The dissipation rate turbulent threshold of 5×10^{-5} m^2 s^{-3} is found to be closely matched to the boundary between turbulent and stable Ri classifications, giving confidence in both measures of the threshold of turbulence.

3.5.2 Richardson number time series

Non-turbulent Ri_g values dominate in the upper half of the cloud layer and above with only small isolated points of potentially turbulent Ri_g values above 800 m (Figure 3.47). Turbulent Ri_g classifications are more frequently observed in the lower half of the cloud and just under cloud base.

Underneath the cloud mixed layer there is a non-turbulent layer of $Ri_g > 1$ values separating the cloud mixed layer and surface mixed layer for the majority of the week. At heights under 200 m there is a near continuous shallow layer of $Ri_g < 0.25$ indicative of a predominantly shear driven surface mixed layer. There are some instances of $Ri_g < 1$ reaching from the surface further up the profile above 200 m and up to the cloud layer. Examples of

where turbulent Ri_g values are very nearly continuous from the surface up to the cloud layer are the 25th/early 26th and late 29th/early 30th.

The cloud and ground are coupled when the profile has turbulent Ri_g values $Ri_g<0.25$ from the surface to the cloud layer. Periods where there is a clear layer of non-turbulent $Ri_g>1$ values between the surface and cloud mixed layer are classed as decoupled. The dissipation rate data provides information on the turbulent structure down to 190 m. Clouds that have a dissipation rate at or over 5×10^{-5} m^2 s^{-3} from cloud top down to 190 m are of an indeterminate coupling state according to the dissipation rate as we can not be certain that the turbulence does not drop off before the surface. The Richardson number provides a view of turbulent state down to 45 m and can pick up cases that are decoupled at heights lower than the dissipation rate is able to. The early hours on the 27th of August are classed as indeterminately coupled by the dissipation rate threshold whereas the Ri data shows clear decoupling. A non-turbulent Ri_g layer is observed at heights between 100-300 m, clearly separating the cloud and surface layers.

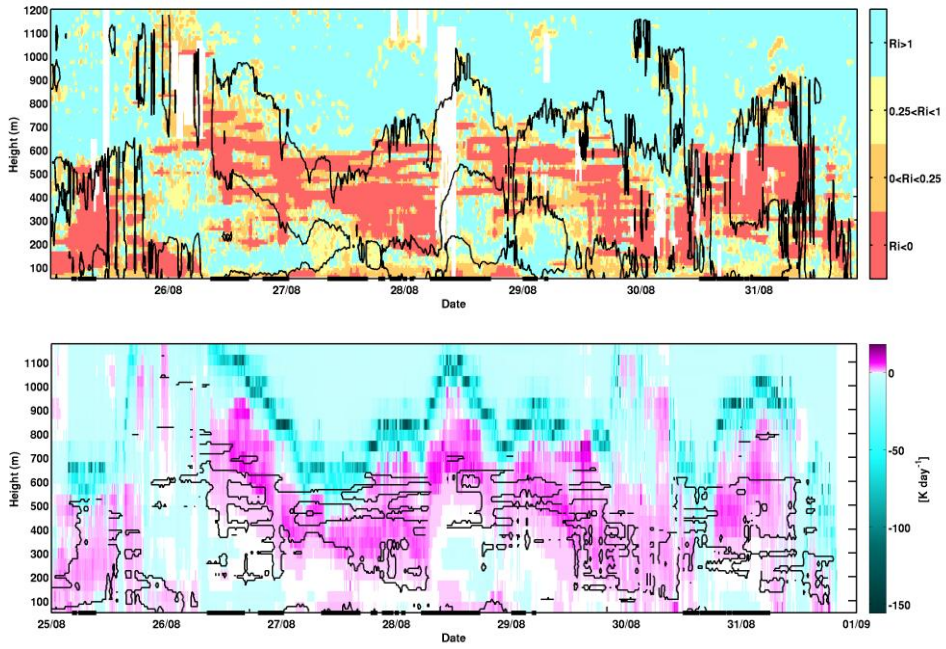

Figure 3.48- TOP- Richardson number time height series coloured by threshold values, black line is the zero contour for the LW heating rate from Figure 3.42. BOTTOM - LW heating rates time height series with the Ri = 0 contour (solid black line), turbulent $Ri_g < 0$.

Overall the Ri_g agrees with the dissipation rate on the timings of cloud-surface coupling in the boundary layer and provides further insight into the turbulent structure. Turbulence is frequently observed to not be continuous from surface to cloud. During periods of decoupling there is a distinct shallow turbulent surface layer under 300 m with an intermittent thin layer of non-turbulent air above. The surface and cloud mixed layers are distinct from each other for the majority of the week. The Ri_g turbulent layer extends from midway down the cloud to a point roughly coincident with the level of the cloud mixed layer depth as diagnosed from the dissipation rate profiles. The structure of the Ri_g numbers and turbulence provides evidence of a boundary layer structure consisting of a cloud mixed layer driven by cooling overlying a shallow turbulent surface layer that are separated by a non-turbulent layer.

3.5.3 Richardson number and heating rate distributions

The distribution of the turbulent Ri_g values is observed to roughly follow the distribution of the positive heating rates from the Edwards-Slingo time height series (Figure 3.48). LW warming extends from the top of the Ri_g turbulent layer down towards the top of the Ri_g non-turbulent layer. LW cooling occurs predominantly in the top third of the cloud which is within the Ri_g non-turbulent layer aloft. The top third layer of the cloud only has intermittent patches of Ri_g values indicative of buoyancy related turbulent motions. A positive Ri_g value indicates that the motions that occur within the cloud layer are stably stratified and no turbulence is generated through buoyancy. A Ri_g indicating stability does not mean the cloud layer is still or no motions occur but that the motions are not turbulent in nature and that turbulence is not generated.

Beneath the peak in LW radiative cooling turbulent Ri_g values are encountered along with slightly positive radiative heating rates. Turbulence in cloud driven by radiative cooling is seen to be shifted down into the cloud away from the cloud top. LW cooling above the peak in LW cooling rates is within a non-turbulent Ri_g layer and so it can be hypothesised that LW cooling here does not primarily generate buoyancy driven motions but instead drives condensation.

The lower limit of the layer of radiative heating is predominantly within the limits of the liquid water cloud (Figure 3.49). The Ri_g turbulent layer aloft

extends under the lower limit of the liquid layer closely following the lower edge of the radiatively heated layer. The lower limit of liquid water extends beneath the cloud base, as detected by the ceilometers. The liquid water under the detected cloud base may be tenuous cloud that is beneath the limits of detection by the ceilometers or it may be liquid water precipitated or sedimented out of the cloud layer that is constrained to the layer of air mixed by cloud buoyant motions.

The peak in liquid water concentrations follow the top of the Ri < 0 cloud-driven turbulent layer (Figure 3.49) and the height of the peak in LW cooling (Figure 3.42). Both the heating rates and Ri_g 'turbulent' classifications predominantly follow the contour of LWC>0. The depth of cloud mixed layer varies and there are influences such as advection and air mass changes that will also alter the layer depth. There is overall a clear relation between the top of the layer considered turbulent by Ri and the base of the cloud cooling layer.

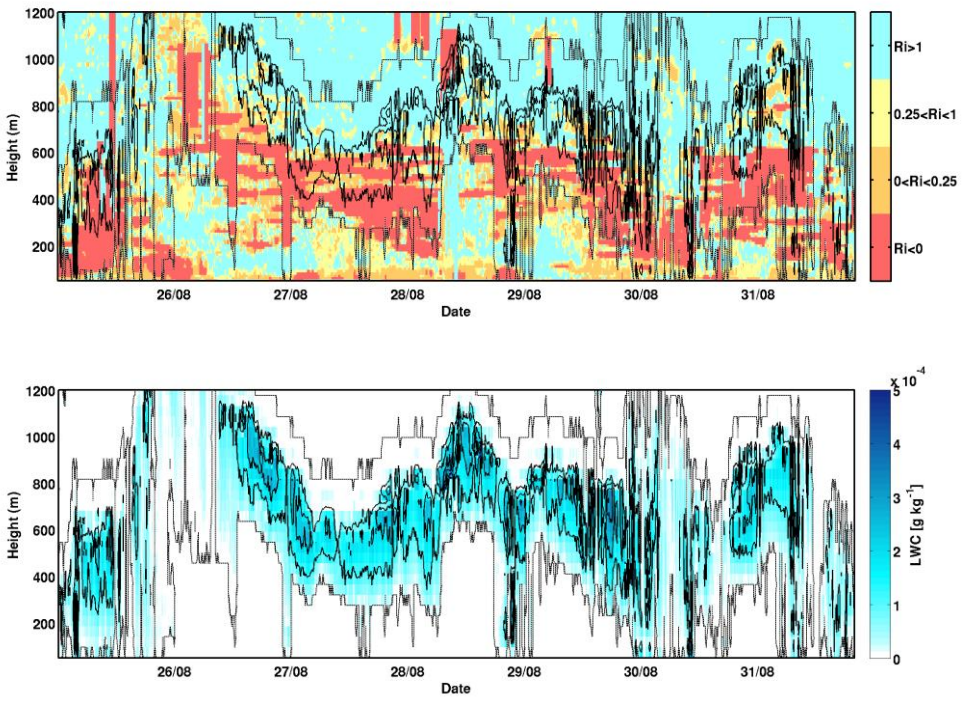

Figure 3.49 - TOP - Richardson number time height series coloured by threshold values, black lines are the liquid water content contours. BOTTOM - Time height series of liquid water content.

3.6 Conclusion

The hypothesis that the MLD is linked to the amount of LW cooling occurring within the cloud top was proven to be correct.

The modelled radiative flux and heating profiles show cooling to peak in the top third of the cloud layer with warming extending down towards the surface. The peak in LW flux increases with LWP for LWP values below the black-body limit of ~40 g m^{-2}. For LWP > 40 g m^{-2} the peak LW fluxes no longer increase with increasing LWP. The MLD increases due to rising peak LW fluxes up until the point the LWP reaches the 40 g m^{-2} black-body level. The MLD varied alongside the LW flux at negative flux values up until the flux was at approximately -5 W m^{-2}, the flux at which the cloud appeared to be radiating as a black body. The MLD is very likely dominated by the LW flux at low LWP where the cloud does not radiate as a black-body. Examination of the trends in MLD with peak cooling rates within the cloud layer showed correlation between MLD and LW cooling at LWP levels under 40 g m^{-2} with a large amount of scatter at higher LWP making any trends between MLD and LW cooling rates above difficult to discern. Above the black-body limit factors other than the LWP become more significant in varying the MLD. It is likely several different processes are occurring to give rise to the scatter in MLD.

As hypothesised radiation modelling in conjunction with the profiles of the Richardson number gave an insight into the relationship between turbulent structure and heating and cooling rates, most notably that the LW cooling within the temperature inversion does not generate turbulent flow.

A non-turbulent layer from a third of the way down into the cloud layer and aloft overlays a layer of turbulent air that is mixed due to the buoyant forcing of cooled descending air. The turbulent layer persists down the profile to a depth related to the strength of the turbulence generated by the LW cooling. In the simple single cloud layers analysed weaker cooling and/or higher cloud restricts the depth the cloud driven turbulence can reach. The restricted depth of cloud mixing results in a non-turbulent layer between the surface and cloud mixed layers, as the cloud driven turbulence cannot extend far enough down to meet the shallow, primarily mechanically driven surface layer (Brooks et al., 2017). The structure of the Ri turbulent layers further backs up that the cooling

at cloud top generates buoyant forces and the resulting cloud driven turbulence is primary cause of coupling as the surface mixed layer is too shallow to reach the cloud layer independently.

Cloud top extends up above the temperature inversion and into the layer above. The cloud layer above the temperature inversion is non-turbulent, turbulent Ri values beginning a third of the way down into the cloud layer under the peak in LW cooling and cloud liquid water concentration maximum. Examination of the liquid water and temperature profiles confirmed that the region of non-turbulent Ri resided within the temperature inversion, peak liquid water content and LW cooling being located at the base of the temperature inversion where the Ri numbers indicated turbulent flow.

The depth over which LW cooling occurs may be a factor in modifying the cloud mixed layer depth regardless of the LWP. Greater extension of cloud into the inversion potentially leads to LW cooling over a greater depth. LW cooling over a greater depth would lead to a shallower, weaker, peak in LW cooling (Deardorf, 1981). Less intense cooling possibly then leads to less intense turbulence generation as the cooled parcels have to descend a smaller distance to equalise temperature with their surroundings. Further work using the Met Office Large Eddy Model (LEM) will investigate further the impact of cloud top extension into the temperature inversion.

4 LEM- Model work

4.1 Introduction

Model simulations are useful to study processes in detail that are difficult or impossible to observe directly in the atmosphere and to test hypothesis from observational data. Model studies are particularly useful for study of Arctic clouds as there is a lack of extensive direct observations with which to fully explore the expected full parameter space.

Model simulations allow the influence of a particular variable to be more easily determined as several simulations can be run with the same starting conditions apart from the variable of interest. The Large Eddy Model (LEM) also allows different processes to be switched on or off or held at a constant value, simplifying the simulation and allowing the response of the boundary layer to be more directly attributed to specific alterations. Here the variable to be altered is the cloud liquid water content. The main influence on cloud mixed layer depth found in the observational studies was the variation in liquid water path and the related change in LW radiative cooling at cloud top. Given the limitations of the observational data, only a limited range of parameters were investigated and, given the complex and constantly evolving real-world conditions, any detailed comparative analysis between clouds with different LWPs is hampered by co-varying conditions that may also impact the cloud mixed layer depth. LEM analysis allows us to reduce the number of variables that change between different runs, to know exactly how much the variable of interest has altered, and thus give confidence in attributing the cause of differences between the simulations.

This chapter will further examine the controls on cloud mixed layer depth in Arctic mixed phase stratocumulus via a range of LEM simulations. Furthering the observational analysis and radiation modelling in the previous chapters. The focus of analysis will be on the behaviour of the cloud mixed turbulent layer that extends down from the cloud towards the surface. The cloud mixed layer depth (MLD) has been observed to alter in response to variations in

cloud liquid water content when the LWP is low enough that the cloud does not radiate as a black body. The response of the cloud layer to LWP variation at low LWP values is predominantly due to the changes in the LW cooling rates at cloud top. Changes in observed MLD with changes in LW cooling rates are observed at all LWP values indicative that LWP alone is not the sole control on peak LW cooling or MLD. There is considerable scatter in the observed MLD data and so picking out the influence of any one subtle control on MLD from the mix is difficult from the observed data alone.

4.1.1 Hypotheses

In this chapter the hypothesis is that the LEM can simulate an appropriate range of LWP values covering the parameter space seen in the ASCOS observations and that subsequent simulations allow evaluation of the trends between MLD and LWP. It is expected that the LEM simulations will show similar trends between MLD and LWP as in the observations. Equivalency between the trends shown in the LEM simulations to the observations will provide evidence that the finer trends unpicked in the LEM simulations are likely to reflect the real world process accurately.

4.1.2 Aims

The specific aims for this chapter are:

- Create a base case LEM run that is a simplified representation of a decoupled mixed phase stratocumulus as observed during ASCOS.
- Identify an appropriate method of varying the simulation LWP with the minimum possible alteration to the initial run conditions.
- Examine the development of the cloud driven mixed layer and its behaviour.
- Confirm that the simulated cloud MLD has the same response to LWP variation as the observed cloud layer during ASCOS.
- Carry out an examination of the profiles of the cloud layer to identify any possible influences on the MLD that could cause the increase in scatter seen in the observational data at LWP's where the cloud LWP indicates it radiates as a black body.

4.2 Model description

The model used is the UK Met Office Large Eddy Model (UKMO LEM referred to as the LEM). Gray et al. (2001) describe the LEM Ver 2.3 in detail. The version used here is Ver 2.4 with the Morrison microphysics scheme (Morrison et al., 2005) as implemented by Dr T. D. Plevin (Plevin, 2013). The LEM is a cloud resolving, anelastic, non-hydrostatic numerical model which explicitly resolves the largest scale eddies in the boundary layer with smaller scale eddies described by sub-grid parameterisations. The LEM is able to run with a high resolution, of a few meters, to enable the study of small scale processes in the atmospheres and explicitly resolve cloud details. It is able to represent a wide range of different clouds and atmospheric processes and situations e.g. The impact of aerosol on sub- tropical Marine stratocumulus (Johnson et al., 2004), cloud top entrainment (e.g. Stirling and Straton, 2011), Cirrus (e.g. Marsham and Dobbie, 2005) and mixed phase cloud (e.g. Marsham and Dobbie, 2006). The LEM will be used here to represent the Arctic mixed phase stratocumulus topped boundary layer.

- The radiation scheme used in the LEM is the Edwards-Slingo radiation code (Edwards and Slingo, 1996) which is called at intervals as defined by the user. The scheme is the same as that used as a standalone radiation mode in the previous analysis carried out in this thesis into the radiative profiles of the observations during ASCOS.
- The original microphysics scheme in the LEM is a single moment scheme, that defines only the mass mixing ratio of liquid and ice water. The number concentration is set to a constant value as defined by the initial setup value chosen. This is inadequate to study detailed interactions between the cloud and boundary layer. The Morrison microphysics scheme used here is a two moment microphysics scheme that diagnoses both the mass mixing ratio and the number concentration. Secondary ice processes, such as rime-splintering, are included (Morrison et al., 2005).

4.3 Setup and base-case design 2D

The case designed follows the work of Plevin (2013). The full size domain in 2D is 5 km in the horizontal Y plane with equal grid spacing of 10 m. Vertically the resolution is 5m below 1260 m and 10 m above; the lower resolution being above cloud top. Each model run is for 24 hours of simulated time, the radiation scheme is called every 10 minutes after the first 30 minutes of model spin-up. The model diagnostic fields are saved every 10 minutes throughout the run.

4.3.1 Simplified BASE case setup

Initial work with the LEM was to create a suitable idealised base case, based on the ASCOS observations, which could then be modified for controlled experiments.

As the focus of this PhD is to look at cloud driven turbulence the surface sensible and latent heat fluxes for the runs were set to zero. This is broadly consistent with the observations, where the surface heat fluxes were close to zero most of the time, and always less than 10 W m^{-2} (Brooks et al. 2017). Geostrophic wind was set to 1 m s^{-1} and kept constant at all vertical levels at inialisation, keeping wind shear and mechanical driven mixing to a minimum. Test cases run with higher, realistic levels of wind (u = -3.5 m s^{-1}, v = -8.0 m s^{-1}, not shown) showed similar cloud mixed layer depths and microphysics in terms of LWP and IWP to the 1 m s^{-1} case. The increased, realistic, wind speeds alter the levels of mechanical mixing within the boundary layer such as the potential depth of the mechanically driven surface mixed layer. As there was no clear difference in the cloud properties and the focus of this study is on the radiatively driven cloud mixed layer the 1 m s^{-1} case was used to minimise any possible influence on cloud behaviour attributable to mechanical mixing rather than radiative driven turbulence. The first case setup was based on the ASCOS observations from the 27th August 2008.

Initial runs based on the 27th August radiosonde profiles quickly showed that in this case the cloud driven turbulence reached the ground soon after the start of the simulation. Such quick and consistent coupling makes the evaluation of changes to the depth of cloud driven turbulence difficult. It was therefore

decided that a different day, with higher cloud, should be used as the basis of the idealised runs. The alternative setup was based on the 11:30 am radiosonde soundings from the 28thAugust. This case has cloud at 800-1200 m with a well mixed layer extending from cloud base to ~375 m. At the base of the well mixed layer there is a shallow 4 K temperature inversion, and coincident humidity inversion, above a well mixed surface layer (Figure 4.50). A humidity inversion of roughly 1 g m^{-2} is present immediately above the cloud layer. The 28th was chosen as we needed a day when the cloud and ground were predominately decoupled with the decoupling at a sufficient height above the surface that we can investigate deeper cloud mixed layer without having to design a new case or modify the existing setup profiles. An initial small temperature inversion beneath the cloud layer located at ~350 m as in the observations was removed. The temperature profile is set to transition smoothly from the surface to cloud value, to allow coupling or decoupling to evolve based primarily on the cloud driven turbulence rather than a predefined inversion below cloud base.

The initial liquid water profile is set to 0 g m^{-3} throughout, rather liquid droplets are automatically condensed out on initialisation of the temperature and water vapour profiles. Liquid cloud spontaneously condenses at initialisation with ice formation occurring from the start. The timing of the radiosonde the humidity profile is based on was during a 'decoupled' period and a humidity inversion is present in the sub cloud layer observations. The model profile of specific humidity has been linearly interpolated from surface to cloud base values. The linear humidity profile will allow the inversion to form in the model simulation naturally throughout the runs.

To avoid confusing changes in the cloud driven turbulence caused by temporal changes in SW radiation, incoming SW radiation was set to a fixed value in the 28th August case (Table 4.3). One of the key areas we are investigating is the cloud driven turbulence generated from radiative cooling at cloud top. A constant incoming level of SW radiation means that the trends we see in analysis in the initial case are not related to changes in the radiative forcing at cloud top via modification due to the diurnal cycle.

Variable			Observed value	LEM base run value
Start date and time			28-08-08 1130	28-08-08 1130
Surface temperature [K]			268.6	268.6
Sensible heat flux[W m^{-2}]			1.24	0
Latent heat flux [W m^{-2}]			1.86	0
SW cycle [W m^{-2}]			Present	TOA 264.3506
U [m s^{-1}]			-3.5	1
V [m s^{-1}]			-8.0	0
Surface pressure [Pa]			102000	102000
Albedo			0.83*	Fixed 0.83
Effec radius water [m]			-	$8e^{-6}$
Effec radius ice [m]			-	$29e^{-6}$
Coriolis [rad s^{-1}]			-	0.0001453
IN concentration [L^{-1}]			-	1.7
Aerosol distribution	Number [μm^{-3}]	2	-	115.0
		1	-	8.02
	Effec radius [μm]	2	-	5.0
		1	-	70.0
	Geometric standard deviation [μm]	2	-	2.56
		1	-	14.5

Table 4.3- Base case LEM -setup initialisation variables. Aerosol distribution is broken down into two modes 1 and 2. *At the time of the profile, the albedo over the subsequent 24 hours will vary.

The initial winds in the base case run are set at a constant value with height to reduce the chance of shear generated turbulence dominating the cloud driven turbulence we are studying. This series of LEM studies is aimed at investigating the cloud driven radiative turbulence and so, although unrealistic, no wind shear with height is included in our runs. Low winds with limited shear also limit the turbulent momentum flux generated at the surface and so gives a minimal mechanically mixed surface mixed layer. A very shallow mixed layer at the surface is important in this simplified case to ensure that the cloud and surface layers remain decoupled throughout the duration of the run. In

addition to there being no change in height the winds are set to a very low value of 1 m s^{-1}.

The model albedo was set at 0.83 matching the observational value at the start of the radiosonde launch. The LEM uses a fixed albedo throughout the model run, so may depart from the later evolution of the albedo that is possible in the observations.

The base case IN concentration was set to 1.7 L^{-1}. The CCN concentrations are not prescribed directly. Droplet activation due to aerosol is taken as a fraction of the aerosol spectra, represented by a multi-mode log normal size distribution, as in Morrison et al. (2005,2009). The aerosol are then activated at a parameterised supersaturation once droplets are at a critical effective radius. The concentrations and spectra used here (Table 4.3) are those as used by Pleavin (2013) which are derived from under cloud observations from flights over the Arctic during Arctic Mechanisms of Interaction between the Surface and Atmosphere (AMISA). The explicit equations of the LEM aerosol activation are not detailed here and can be found in Morrison et al., (2005,2009) and Pleavin (2013).

4.4 Basic cloud-mixed-layer investigative setups

As the LWP and LW radiative cooling appear to be the dominant influences on the depth of the cloud mixed layer it was decided that LEM simulations of a modified base case with different LWPs would be run. The model simulations will confirm whether the observation findings translate into the model and if the model behaviour follows the observational then we can have clear faith in our hypothesis. If the model simulations do match that of the expected results from the observations we will then be able to further analyse the model results to obtain information about more than just the dominant processes controlling the MLD in the knowledge that our runs are relatable to the behaviour of the observations.

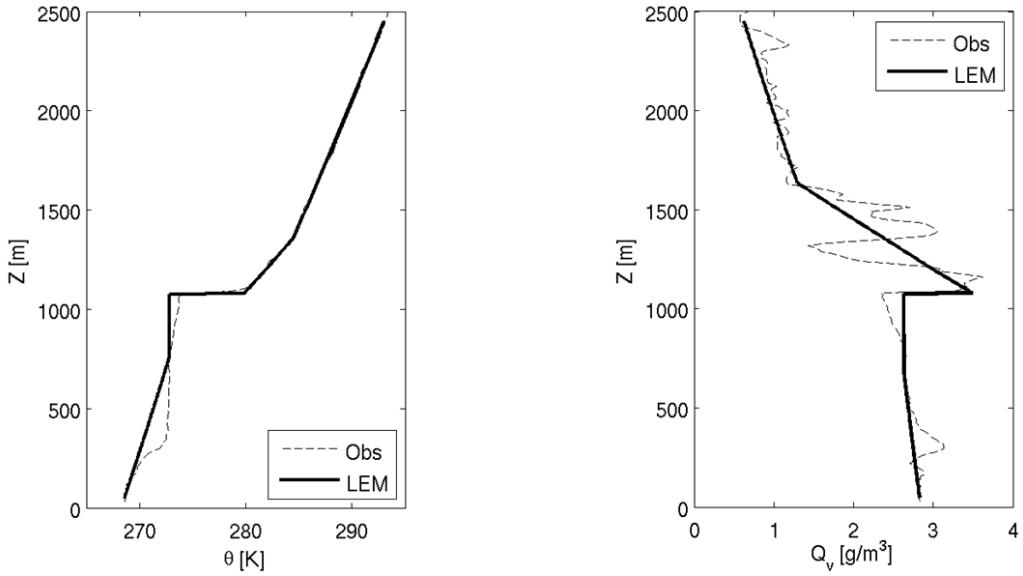

Figure 4.50 - Profiles of potential temperature (LEFT) and specific humidity (RIGHT) from the radiosonde observation at 1130 on 28th August 2008 (dashed line) and the simplified profiles used as initialisation profiles for the LEM runs (solid line).

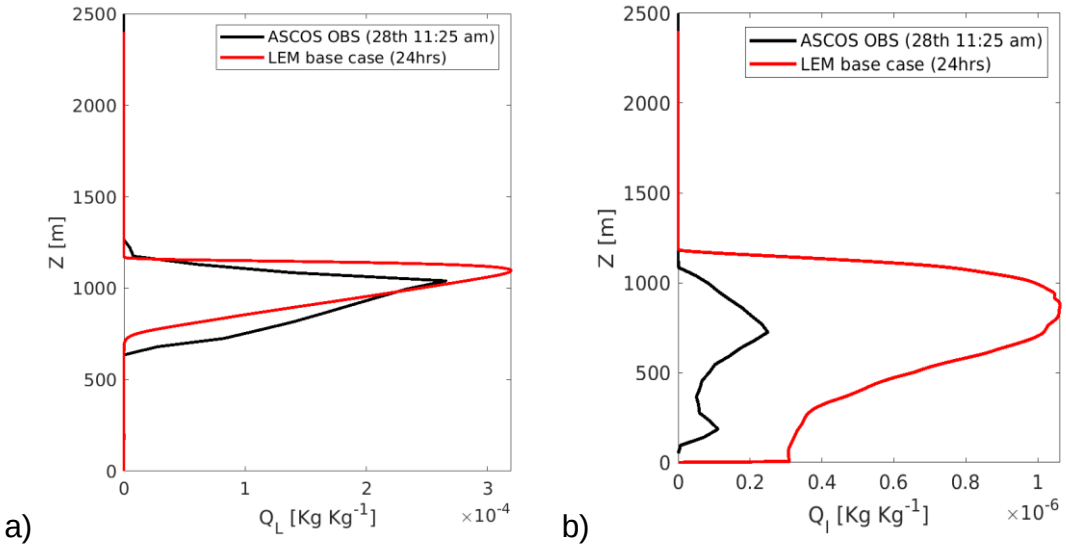

a) b)

Figure 4.51 - ASCOS observations from time of initialisation profiles and the LEM profiles from the end of the run once fully span up. a) The liquid water mass, b) the ice water mass.

4.4.1 Base case observations comparisons

The base case LEM simulation is based on the cloud that occurred during ASCOS on the 28th of August 2008. The cloud on the 28th had a LWP of around 75 g m^{-2} and a cloud layer from 600-1200 m (Figure 4.51a). The observed cloud MLD extended down from cloud top to 400 m giving a MLD of 800 m. The cloud was mixed phase with precipitating ice that reached from cloud base to the surface.

The simulated cloud based on the observed radiosonde profiles has an average cloud depth of ~400 m. The LEM cloud base is between 650-700 m and cloud top rises from 1000 m to 1175 m as the cloud entrains air from aloft (Figure 4.51a). The LEM cloud driven mixed layer did not reach down to the surface at any point during the simulation. After ~6 hrs the LWP stabilised at around 80-85 g m^{-2}. The mixed layer depth was on average ~650m, becoming increasingly variable as the run progressed. The LEM cloud is mixed phase with ice present throughout the boundary layer as is the observed cloud layer (Figure 4.51b). More ice is present in the LEM than the observations but the shape of the profiles is consistent and overall ice mass is well within the range of ice water paths observed in Chapter 2 Figure 2.20.

4.4.2 Method of case LWP variation

The base case design requires modifying in an appropriate way to provide a suitable range of LWP values with which to study their impact on cloud MLD. Ideally the alteration to cause LWP variation will require little change to the initial setup, keeping the runs as similar as possible. Alterations made to the initial setup can cause coincident variation alongside the changes due to LWP variation, complicating the comparative analysis.

The modification of the temperature profile between runs to create a higher LWP cloud layer was deemed inappropriate. Changes to the temperature profile will alter the stability of the profile and LW cooling. The subsequent turbulence generation of variable temperature profile runs and the depth to which the cloud driven turbulence may reach will vary independently of the liquid water content of the cloud layer.

Runs with variable humidity profiles were tested. It was found the cloud layer formed at the start of the run varied but quickly returned back to the LWP levels of the original base case. The cloud formation being robust and primarily dependent upon the initial temperature profile rather than the specific humidity. It is also the case that changes to the humidity profile will alter the LW cooling profile. A complete removal of the humidity increase above the cloud layer reduced LWP at the start of the run but the cloud LWP gradually rose up to just under the base case levels of LWP by the end of the 24 hours run time, which is not a useful response for creating a series of runs with stable cloud layers at a range of LWP's.

An alternative to modifying the initialisation profiles of temperature and humidity is to modify the amount of ice formation by altering the amount of ice nucleation that occurs. The amount of ice that occurs alters the amount of liquid water within a cloud layer as greater ice concentrations uptake water vapour at the expense of liquid droplets via the Wegener–Bergeron–Findeisen (WBF) process. Altering the concentration of ice nuclei (IN) will alter the levels of ice formed and so alter the amount of liquid water formed, all other variables being equal. Modifying the cloud condensation nuclei concentrations values achieves some change in LWP but not significantly enough to reach the LWP at which the cloud will not radiate as a black body.

The Morrison microphysics scheme allows alteration of the amount of ice formation by modifying the number of droplets converted to ice in a given volume in a proxy of heterogeneous ice nucleation. The limitations here being that the amount of liquid converted into ice is not limited by the total number of aerosol available, so unlike the real world the ice production does not stop because all of the available ice nucleating aerosol has been used. The nucleation is also not specific to locations where the aerosol might be concentrated but is constant throughout the domain.

4.4.2.1 IN variation runs

To manage to get the higher than base case LWP values the ice concentration needs reducing, to get the lowest LWP values the ice concentration needs increasing. The base case has an IN concentration of 1.7 L^{-1}. To get a range of different LWP values runs with IN concentrations that are multiples of the

base case were run. IN concentrations at the base case IN × 0.1, 0.25, 0.5, 1, 2, 3, 4, 5, 6, 7, 8, 9 were carried out.

The runs provide a suitably wide range of LWP for analysis. The mean liquid water path from the end of the simulations varies from 218.1 g kg^{-2} for the lowest IN run to only 0.8 g kg^{-2} for the highest IN run (Table 4.4). The IN runs from IN×3 to IN×9 all have LWP values under the point at which the observed cloud is seen to behave as a grey-body. The IWP for the two highest IN runs is lower than the previous IN multiple run of IN×7. The LWP in the IN×8 and IN×9 runs may have fallen so low that the ice formation is subsequently restricted.

The range of IN concentrations used ranged from 0.17 L^{-1} to 17 L^{-1} covering two orders of magnitude. The very low IN levels used here are realistic in the Arctic given the observations of very low CCN concentrations e.g. Mauritsen et al. (2011) and the observations of low ice concentrations in cloud.

The higher IN concentrations of 13.6 L^{-1} and 15.3 L^{-1} produce IN runs that have a liquid water collapse as rapid glaciation of the cloud layer occurs. The Hallett-Mossop process is a well known phenomena that creates a vast number of ice nucleating particles in the form of ice splinters causing rapid glaciation, rime-splintering. The process of ice splintering occurs at temperatures between -3°C and -8°C which is within the range of temperatures of the cloud layer in our LEM simulation. Hallett-Mossop processes have been identified as the likely cause of higher observed ice concentrations than that explained by the IN concentrations in mixed phase clouds over Antarctica (Grovsnor et al. 2012). Mean ice concentrations, where the Hallett-Mossop effect was hypothesised to be operating, were up to a factor of two higher than in the standard observations. It is suggested by Grovneor et al., (2012) that the production of ice shards by rime-splintering may impact further down in the cloud layer than purely the zone in which the initial splintering occurs as the splinters are transported by cloud motions downwards into the cloud layer. The transported ice shards cause nucleation down through the profile increasing the ice concentration over the value explained by the IN concentration over an extended depth. It has been shown by Crawford et al. (2012) that the Hallett-Mossop process is capable of

increasing ice concentrations by 4 orders of magnitude. The highest ice concentrations reached in the LEM runs, where IN was set to 11.9 L^{-1} , were one order of magnitude higher than the base case 1.7 L^{-1} IN run (Table 4.4). The one order of magnitude rise in ice concentrations over the range of IN concentrations used is well within the four orders of magnitude possible according to Crawford et al. (2012). A caveat being that the highest ice multiplications are observed when drizzle is present, a case not observed in the ASCOS simulations.

The high IN concentrations of the LEM runs used in the LEM runs carried out in this thesis may be higher than typical occurrence but the literature indicates it is not unrealistic and thus our inclusion of these runs and use of these high IN concentrations is acceptable in order to cover the possible parameter space of ice concentrations.

Base IN×n	IN [L^{-1}]	LWP [g m^{-2}]	IWP [g m^{-2}]
0.1	0.17	218.1 ± 3.7	0.38 ± 0.031
0.25	0.425	159.9 ± 2.6	0.49 ± 0.018
0.5	0.85	117.2 ± 1.7	0.66 ± 0.017
1	1.7	85.4 ± 1.5	0.93 ± 0.020
2	3.4	53.2 ± 1.8	1.52 ± 0.030
3	5.1	37.7 ± 1.5	2.08 ± 0.014
4	6.8	27.6 ± 0.5	2.59 ± 0.030
5	8.5	22.1 ± 0.9	3.16 ± 0.068
6	10.2	17.0 ± 1.5	3.65 ± 0.043
7	11.9	11.7 ± 1.6	4.04 ± 0.042
8	13.6	1.0 ± 0.1	3.41 ± 0.100
9	15.3	0.8 ± 0.1	3.46 ± 0.099

Table 4.4 - Simulation end levels of LWP and IWP for the different IN multiple runs and the exact IN concentration, mean taken over the last 4 hours and error is the standard deviation.

4.4.3 3D

The runs carried out in this thesis are exclusively in 2D. Some variation in exact levels of turbulence is expected between the 2D and 3D simulations. Runs in 2D have been shown to have stronger turbulence than their 3D equivalent (e.g Moeng et al., 1996).

Pleavin (2013) ran 3D validation runs of the Morrison microphysics setup in the LEM and compared it to the 2D simulations. The Turbulent Kinetic Energy (TKE) was found to be stronger in the 2D runs than the 3D. Cloud structure, however, was consistent between the two, as were the moisture budgets. The trends of TKE with alterations in the cloud layer were consistent between the 2D and 3D runs. Conclusions drawn on the processes occurring within the cloud layer based upon a 2D run will therefore be applicable to 3D runs and real world processes. Plevin (2013) states that " *the total length of time needed to run the 3D simulation over 160 processors was more than three weeks for a 20 hour simulation*". An advantage of 2D allows multiple runs to be carried out with comparatively minimal computational expense. The 2D runs require 1 processor and take 3 to 4 days to run. The use of 2D allows a wide variety of test runs and simulations to be carried out to explore a variety of parameters.

4.5 Overview of analysis runs

4.5.1 Run progression

The LWP increases from the start of the run as the cloud layer develops stabilising after about 10 hours for the runs IN×1 to IN×7 (Figure 4.52). Runs IN×8 and IN×9 have a LWP that decreases from the start of the run towards 5 hours when the liquid cloud fully dissipates. After 5 hours of simulation time the cloud reforms in the runs IN×8 and IN×9 but LWP remains below 10 g m^{-2}. The LWP of the lower ice runs IN×0.5 and IN×0.25 stabilise after 15 hours. The highest LWP values reached are in the IN×0.1 run which levels off after 20 hours at over 210 g m^{-2}.

The level of the runs' stabilised LWP gives a range of LWP values above and below the LW radiation black-body threshold. The runs that level out at or

under 40 g m^{-2}, the LWP value where the ASCOS observations show the cloud no longer radiates as a black body, are those with an IN concentration of IN×3-9. At the highest IN values of IN×8 and IN×9 the simulations reach a 'critical' value where the liquid water in the cloud layer drops to zero as the cloud is fully glaciated.

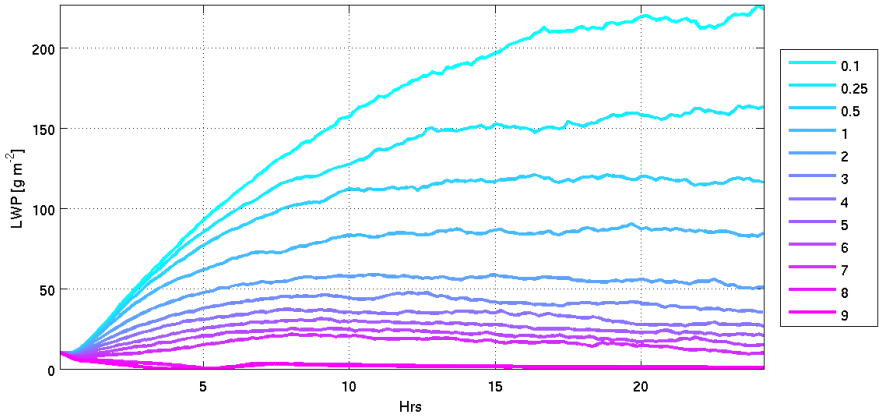

Figure 4.52 - Time series of the LWP for the full range of the IN runs demonstration the range of LWP conditions achieved. The colour indicates the multiplication of the base aka [1] case heterogeneous ice nucleation.

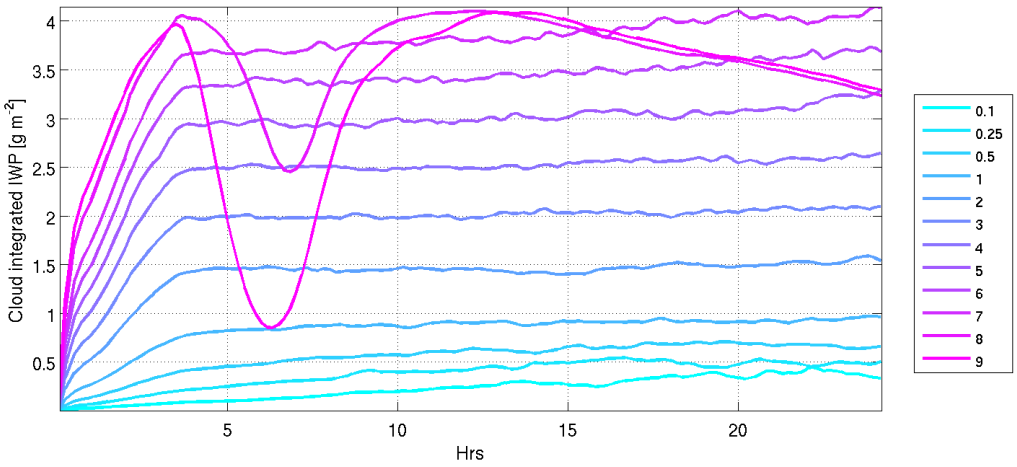

Figure 4.53 - Time series of the IWP for the full range of the IN runs demonstration the range of IWP conditions achieved.

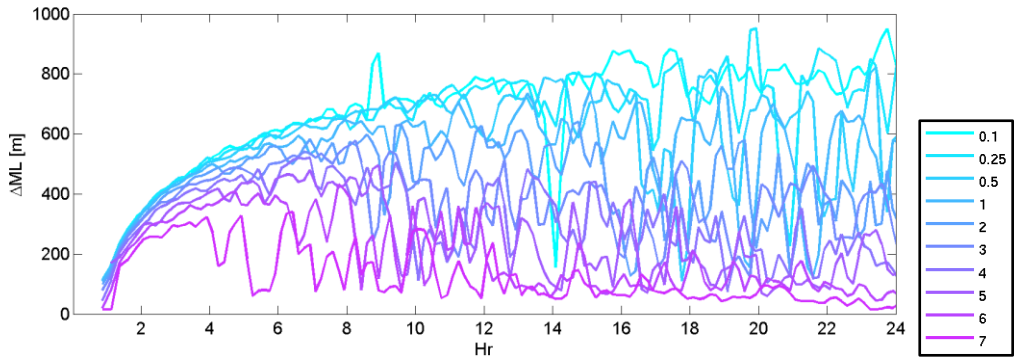

Figure 4.54 - Time series of the clouds mixed layer depth, colours are the same as Figure 4.52 but note that runs with ×8 and ×9 IN levels are not shown on this figure as their dissipation rate values never become high enough to cross the minimum 5×10^{-5} m^2 s^3 threshold.

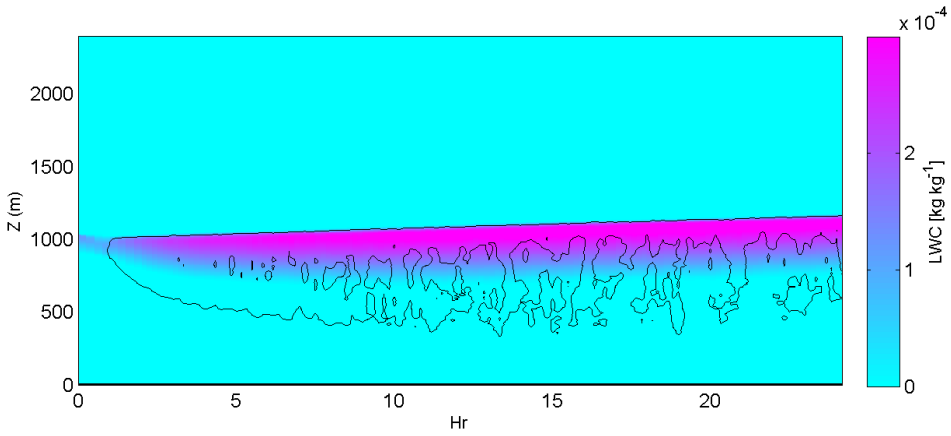

Figure 4.55 - Time height plot of cloud liquid water content (colours) with the dissipation rate limit contour of 5×10^{-5} m^2 s^{-3}. For the IN×1 run.

IWP can be seen to be relatively stable with a slight increase as the runs progress after 4 hours run time for all but the IN×8 and IN×9 runs (Figure 4.53). IWP values for the IN×8 and IN×9 runs show a different behaviour in time to the lower IN simulations. Rather than increasing quickly then having a shallow rise the high IN runs IWP drops off just before 4 hours run time, recovering between 6-7 hours to original IWP levels then reducing down to the IN×7 simulation level IWP after 24 hours. The timing of the initial drop in IWP for the high IN runs is at the point in the runs where the liquid water drops to zero. With no liquid water the ice formation is reduced and the IWP drops as the ice is removed via precipitation, sublimation and sedimentation. Recovery in the IWP begins as liquid water begins to condense out again at cloud top

and the cloud layer redevelops but then begins to drop once more. A drop in ice likely occurring as the weak turbulence fails to drive the turbulent motions required to maintain the cloud layer.

The cloud mixed layer depth for the LEM simulations was taken as the depth from cloud top to the first level beneath cloud that the dissipation rate drops under the threshold level of 5×10^{-5} m^2 s^{-3} as used by Shupe et al. (2013). The cloud mixed layer depth is greater with the highest LWP runs of IN×0.1, IN×0.25 and IN×0.5 and lowest in the high ice runs up to run IN×7 (Figure 4.54). The dissipation rate never reaches above the 5×10^{-5} m^2 s^{-3} threshold for the highest ice runs of IN×8 and IN×9 and so these runs have a mixed layer depth of zero.

a)

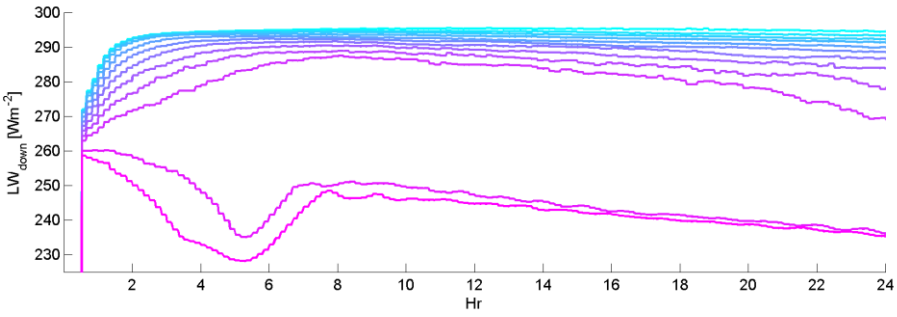

b)

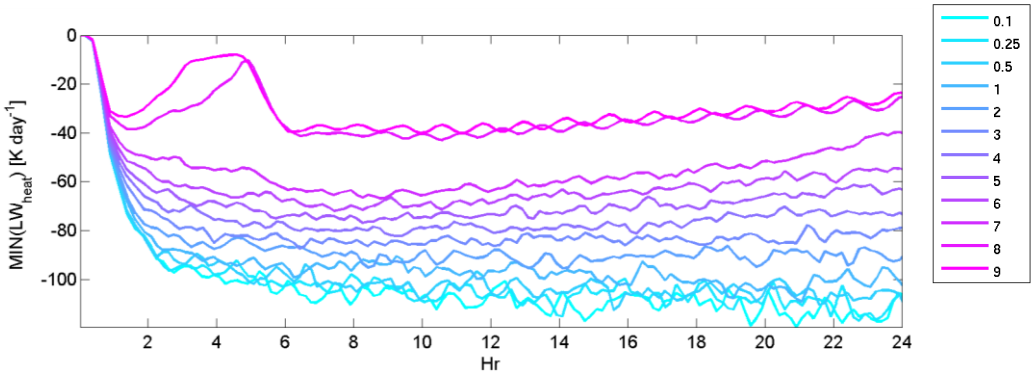

Figure 4.56 - a) Time series of the profile minimum LW down welling radiation and b) the profile peak LW cooling. Colours are the same as Figure 4.52, light blue being higher LWP.

The dissipation rate typically peaks near cloud top and drops within the cloud layer (Figure 4.55) Turbulence under the peak at cloud top can drop under the turbulent threshold within the cloud layer before increasing again towards the base of the cloud mixed layer. The mixed layer depth is calculated as the first height down the profile where the turbulent limit is first reached. Where the dissipation rate drops under the turbulent limit within the cloud layer the MLD will be shallow. When the turbulence within the cloud layer does not drop before increasing again the MLD is calculated to be much further down the profile. The variability of the height of the MLD can be interpreted as intermittent driving of cloud driven turbulence down into the boundary layer over time (Figure 4.55). The mixed layer depth variability increases after the point where the LW flux and heating rates stabilise for each run (Figure 4.56).

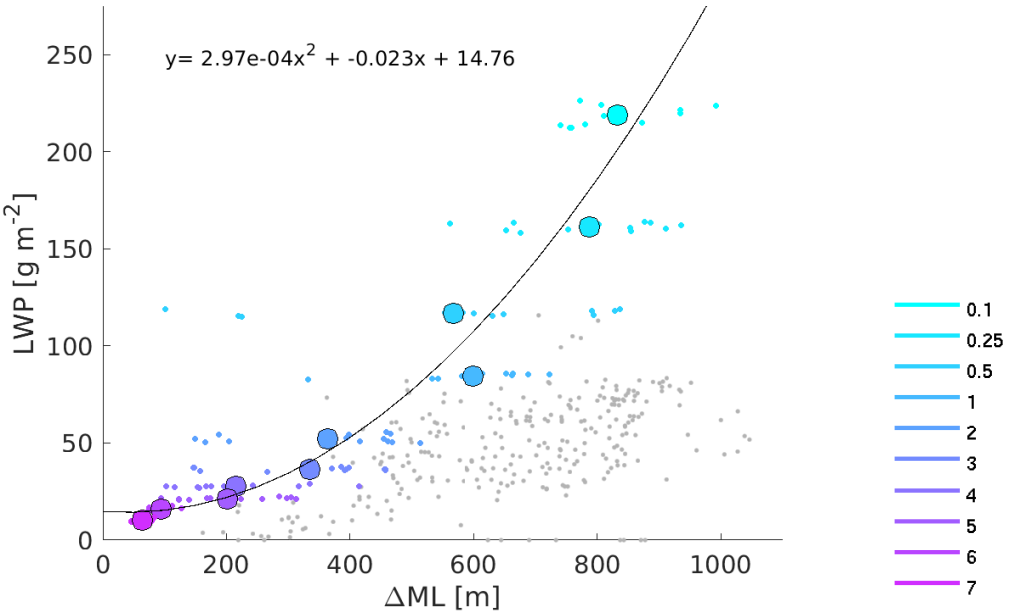

Figure 4.57 - LWP of the LEM IN runs mean profile liquid water against the mixed layer depth as calculated from the dissipation rate profiles. Small dots are the individual 10 min outputs from the last 2 hours of the 24 hour simulation, the black rimmed filled circles are the mean value of the last 2 hours of the simulation. Runs IN×8 and IN×9 are not plotted as their mixed layer depth is zero. Grey dots are ASCOS observations as used in chapters 2 and 3.

The radiation is switched on in the simulations after 30 minutes of spin up. The LW radiation flux increases rapidly for the highest LWP runs with a slower rise for the high ice runs up to IN×7 (Figure 4.56a). The LW flux for the IN×8 and IN×9 runs reduces after initiation, in line with the reduction in the liquid water over the first 5 hrs. The LW heating rates span from -20 K day^{-1} to -120 K day^{-1} (Figure 4.56b). The higher liquid water runs of IN×0.1-1all have similar LW cooling values with increasing IN×n runs having progressively lower peak LW cooling values.

4.6 Impact of LWP variation

In the observational analysis in chapters 2 and 3 changes in the LWP are found to be a dominant control over the MLD when LWP is low enough the cloud radiates as a grey-body. When radiating as a grey-body the MLD increases rapidly with a small rise in LWP. The observed LWP grey- to black-body threshold occurred around 40 g m^{-2}.

In the LEM simulations the cloud MLD increases with small increases in LWP at LWP values below 50 g m^{-2}. MLD rises from just over 50 m to just under 400 m for a rise from 10 g m^{-2} to 50 g m^{-2} (Figure 4.57). A further increase in LWP of over 150 g m^{-2} from 50 g m^{-2} gives only a further 500 m increase in MLD, the majority of which is at the lower LWP values. The behaviour of the MLD and LWP in the LEM simulations is consistent with observations.

The MLD increases with increasing LW flux up to a MLD of ~400 m, the LW flux stabilises, due to the increase of LWP over the black-body threshold at MLD deeper than 400 m, while MLD varies from ~400 m to just under 1000 m (Figure 4.58a). The LW flux relationship in the LEM and observations is consistent. The transition between grey- and black-body states is smoother in the LEM simulations than the observations. The LEM simulations are the behaviour of one cloud to altering LWP, whereas in the observations the properties of the cloud layers varied along with the LWP. The MLD increases with increasing LW cooling at all levels of LW cooling, not just those where the LW flux alters due to LWP variations (Figure 4.58b). Greater MLD is associated with greater LW cooling.

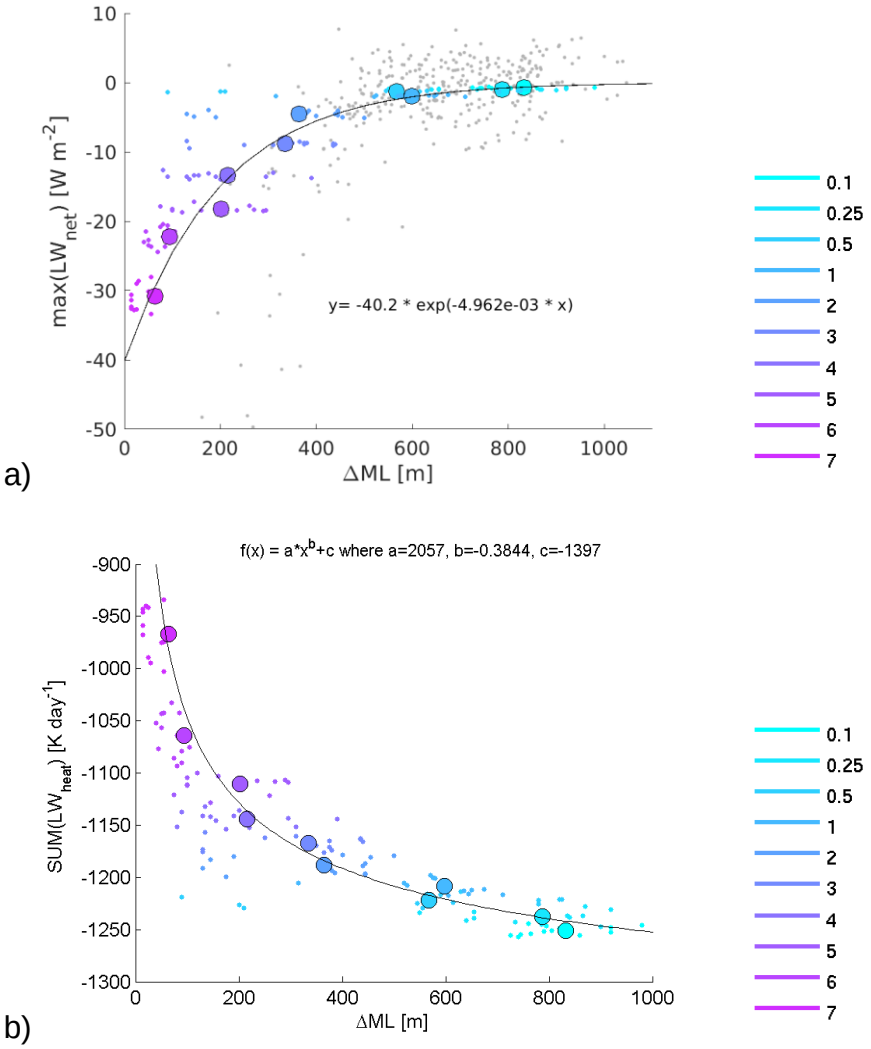

Figure 4.58 - a) Profile peak LW radiative flux vs MLD, grey dots are ASCOS observations as used in chapters 2 and 3 and b) Profile peak LW cooling vs MLD. Small dots are the individual 10 min outputs from the last 2 hours of the 24 hour simulation, the black rimmed filled circles are the mean value of the last 2 hours of the simulation.

The relationship between the cloud MLD and the LWP is consistent between the observations and the LEM simulations. The changes in LWP alter the LW radiative flux when the LWP is beneath the point where the cloud layer radiates as a black-body. When LWP is that of a grey-body cloud the changes in the LW flux due to variations in LWP alter the LW cooling, which in turn drives buoyant motions altering the MLD. Above the point where the cloud radiates as a black-body the peak LW cooling and MLD are still positively correlated but the variations in the MLD will no longer be related to LW cooling changes due to LWP variation.

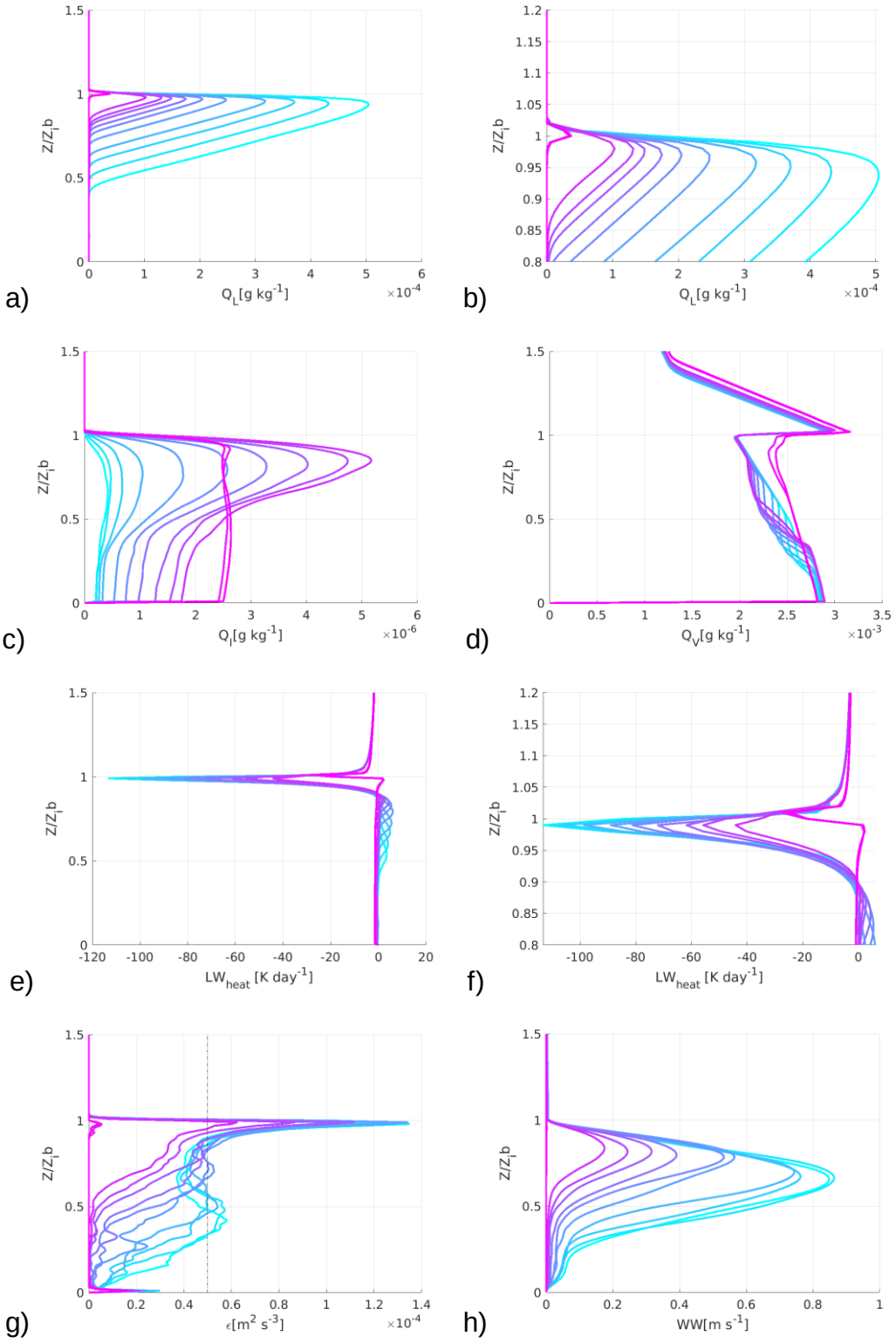

Figure 4.59 - Last hour mean domain profiles of - a) Liquid water concentrations, b) liquid water concentrations zoomed, c) Ice concentration, d) Specific humidity, e) LW heating, f) LW heating zoomed, g) Dissipation rate with dashed vertical line the dissipation rate turbulent limit, h) Vertical velocity variation. Colours indicate different IN runs as in Figure 4.56, High IN to Low IN = Magenta to Cyan.

Consistency in the behaviour between the LEM and ASCOS observations is indicative that the conclusions based on the 2D LEM runs are applicable to the real world.

4.7 Profiles of cloud properties and turbulence

Profile plots are normalised in height with the height of the base of the temperature inversion (Z_{ib}). Normalisation allows the direct inter-comparison of key features within the profiles that would otherwise be at different heights and depths.

The lower the IN fraction the deeper the cloud layer and the greater the peak liquid water concentrations (Figure 4.59a). The high ice runs show peak ice water concentrations over 5 times that of the base case and show a relatively narrower peak compared to the base case and high LWP runs (Figure 4.59b).

The specific humidity above cloud is higher in the higher ice runs as the inversion aloft has been eroded away less by 24 hours of run time than the low ice runs as cloud top rises at a slower rate in the high ice runs (Figure 4.59c). The cloud top is lower in the profile at the end on the run in the higher ice runs than the low ice runs as the greater turbulence in the low ice runs entrains more air from aloft and cloud top rises further in the 24 hours of the simulation. The faster rise of cloud top in the lower ice runs erodes away the specific humidity inversion aloft at a faster rate than the high ice runs. The drop off of ice and liquid concentrations in the high ice runs not due to the unavailability of water vapour. The high ice runs (IN×8 and IN×9) are not water vapour limited so there must be a different reason for cloud collapse and LWP reduction after the cloud layer reforms.

The profile peak LW cooling is weakest in the higher the IN×n runs (Figure 4.59d). The LW peak cooling increases non-linearly with a reduction in IN×n and at IN×2 and lower the peak cooling is near identical. The LW cooling peak is located just under the temperature inversion base for all of the runs excluding IN×8 and IN×9 (Figure 4.59d). Cooling occurs over a similar depth of all the runs but the peak LW cooling reduces broadening the cooling profile, and subsequently impacting the buoyancy fluxes. Cooling will also be affected by the variations in the humidity profile above cloud. The higher humidity

above the cloud layer the more the layer at cloud top is warmed by the LW emitted from the water vapour aloft and the lower the potential net LW cooling to space.

The dissipation rate peak values get weaker as the IN×n increases and the dissipation rate 5×10^{-5} m^2 s^{-3} is reached further down through the profile (Figure 4.59e). The dissipation rate drops beneath the turbulent limit mid way through the cloud layer in the highest LWP runs of IN×0.1, IN×0.25 and IN×0.5 before increasing again in the region of cloud base.

Peak vertical velocity variance increases with increasing LWP, both under and above the LWP where the cloud layer begins to radiate as a black-body. The vertical velocity variance peaks roughly 2/3 of the way down the liquid cloud layer under the peak in liquid water concentrations (Figure 4.59a). Deeper, higher cloud layers, with less ice, have greater LW peak cooling and stronger and deeper-reaching turbulent mixing.

A higher proportion of the cloud extends into the temperature inversion in the runs IN×8 and IN×9 than in the other IN×n runs (Figure 4.59a). As a consequence of the higher extension of the cloud into the inversion the LW cooling peak is also shifted up into the inversion(Figure 4.59d). There is a shift in behaviour between the IN×7 and IN×8 runs and the shift of LW cooling further up into the temperature inversion may be a contributing factor. The impact of the extension of the cloud layer up into the inversion is investigated further in Chapter 5.

4.8 Conclusions

Variation of the amount of heterogeneous ice nucleation occurring in the runs via modification of the IN concentration was used to give a range of LEM simulations with different LWP's while keeping the initial thermodynamic profiles constant.

The hypothesis that the LEM can simulate an appropriate range of LWP vales was proved to be correct with simulations carried out with LWP ranging from 0.8 g m^{-2} (IN×9) to 218.1 g m^{-2} (IN×0.1) (Table 4.4). The simulations were run with a base case IN concentration of 1.7 m^{-1} and bas case IN multiples of

IN×0.1, 0.25, 0.5, 1, 2, 3, 4, 5, 6, 7, 8, and 9. The modelled cloud MLD increases with increasing LWP at LWP values below 50 g m^{-2}, where the cloud is radiating as a grey-body. The response of the cloud MLD to LWP is the same in the LEM simulations as in the ASCOS observations.

Analysis of the MLD in relation to the LWP demonstrated a comparable trend between observations and simulation, with an increase in LWP resulting in a rise in MLD which was greatest when the LWP was under the black-body level of LWP ~40 g m^{-2}. The peak LW cooling and MLD are correlated with higher peak LW cooling resulting in deeper MLD generation though scatter in the MLD with LW cooling is greater at greater MLD. The response of the MLD to increased LWP, the resultant changes in LW flux, and cooling rates is the same in the LEM simulations as in the observations. The comparable response of the cloud layer to variations in LWP give confidence in the findings of the more in depth analysis of the behaviour of the simulated cloud.

The factors identified that add to the scatter of the MLD via modification of the generated turbulence through LW cooling not due to variations in the LWP are:

- Humidity profile aloft - higher humidity above the cloud increases down welling LW radiation at cloud top, offsetting some of the upwelling LW radiation, consequently reducing the net cooling. The reduced net LW cooling reduces the turbulence caused by buoyant motions attributable to cooling.
- Broadening of the cooling peak / liquid water distribution - In the runs here the more tenuous the cloud the greater the relative depth the LW cooling extends over, with a resultant shallower peak in LW cooling and consequently weaker down drafts and cloud driven turbulence.
- Extension of cloud into the inversion - LW cooling is observed to shift up into the inversion with increased relative extension of liquid cloud into the inversion. The impact of the moment of LW cooling up above the base of the temperature inversion on the cloud driven turbulence generation is unknown at this time.

The influence of the humidity aloft, liquid water distribution and the shape of the LW cooling peak are all factors that occur globally and are well studied.

The extension of the cloud layer into the temperature inversion is a unique feature of the Arctic atmosphere and its impact upon the cloud layer not well understood. Consequently it would improve our understanding of the Arctic stratocumulus topped boundary layer and the depth of its cloud mixed layer to investigate the influence of the extension of the liquid cloud layer up into the inversion upon the depth of the cloud mixed layer and turbulence generation within the cloud layer.

5 LEM investigation into the impact of liquid cloud extension above the temperature inversion in Arctic Stratocumulus

5.1 Introduction

In the Arctic the cloud top is observed to extend above the base of the temperature inversion and into the humidity inversion aloft (e.g. Solomon et al., 2011, 2014), features not observed in stratocumulus at lower latitudes. Extension of cloud up above the base of the temperature inversion has been linked to the unexpected persistence of mixed phase clouds and increased cloud lifetime (Solomon et al. 2011). The layer of cloud that extends up into the temperature inversion has been observed to be a region of positive vertical velocity skewness, indicating a reduction in buoyancy flux (Sedlar and Shupe, 2014). Cloud layers in the mid-latitudes have a peak vertical velocity variance near cloud top whereas the cloud layers in the Arctic that extend up into the temperature inversion have been observed to have a peak vertical velocity variance 75-150 m below cloud top, likely due to a lack of turbulence generation in the layer extending into the cloud (Sedlar and Shupe, 2014). Sedlar et al., (2012) found that the extension of cloud up into the temperature inversion altered the peak LW cooling.

There is a paucity of research into the influence of the extension into the inversion upon the cloud layer and so its influence on cloud driven turbulence and boundary layer properties is not well known. LW cooling and the resultant buoyancy driven turbulent motions has been established as a key factor in the depth of cloud driven turbulence and consequently the coupling state of the boundary layer; anything that may influence that cooling in magnitude or structure may have an influence upon the cloud generated turbulence.

Work in previous chapters has highlighted the dominant control over the cloud mixed layer and cloud driven turbulence as that of LW cooling due to variations in the cloud layer LWP at low LWP. The influence of LWP is significant under ~50 g m^{-2} where the cloud radiates as a grey-body. The variation in cloud driven turbulence and cloud mixed layer depth is variable

and shows scatter not explained purely by LWP and peak LW cooling variation. There are likely to be multiple influences on the cloud driven turbulence aside from the dominant influence of LWP that are hard to study in the observational data due to the co-variance of cloud properties and overwhelming control of LWP below its black-body threshold.

5.1.1 Hypotheses

We hypothesise that the depth of the extension of the cloud layer into the temperature inversion aloft impacts the depth of the cloud mixed layer and the subsequent turbulent structure of the boundary layer. The current hypothesis to be tested here is that the extension into the temperature inversion of cloud top somehow inhibits the generation of turbulence.

5.1.2 Aims

This chapter will investigate how the variation in the amount of cloud that extends above the base of the temperature inversion impacts the cloud driven turbulence and to characterise the cloud behavioural response to the extension of cloud top into the temperature inversion. The aims of this chapter are to:

- Design a case where the extension into the inversion can be varied with the LWP not significantly altered between the extension simulations.
- Examine the influence of the extension of the cloud top into the temperature inversion upon cloud mixed layer depth (MLD), boundary layer development and turbulent profiles.
- Determine the response of different extensions into the inversion to variations in ice nuclei (IN) concentrations. The point in these runs is to see if and how the scatter in cloud-driven turbulence co-varies due to microphysics changes and extension into the inversion. Does the extension into the inversion add to the response of the turbulence to low LWP, negate it, or have no influence?

5.1.3 Case design

The base case used here is identical to the base case as used for the IN×n LWP variation runs used in chapter 4. The constants used are as those in Chapter 4 Table 4.3. To investigate the impact of the variation of cloud top

extension into the inversion the base case run has to be modified to give a range of cloud top extensions into the inversion.

As with the previous LEM work the runs are all carried out in 2D to allow a wide range of parameters to be investigated. The case design runs investigated the variation of the cloud extension into the temperature inversion caused by varying the humidity profile at and above cloud top.

Three different temperature and humidity profiles were run. The difference between the base case cloud top extension into the inversion and the extension of the modified profiles was then compared. A list of the completed runs is available in Table 5.5.

The humidity increase above the temperature inversion is a distinctive Arctic boundary layer phenomenon. For the initial state humidity profile, modifications to the height at which the increased humidity extends was altered (Figure 5.60). A range of three different humidity extensions were run, with the strength of the humidity inversion kept constant between runs at 3.5 g kg^{-1}. The base case humidity inversion extended up to 895 mb ($Base_{norm}$) the variations were 885 mb (Mid_{norm}), 865 mb ($High_{norm}$) and 835 mb (Top_{norm}).

Run name	***Q_v inversion top height [mb]***	***IN × of base case***
$Base_{norm}$	895	1
Mid_{norm}	885	1
Top_{norm}	835	1
$High_{norm}$	865	1
$High_{wet}$	865	0.1
$High_{ice}$	865	7
Mid_{ice}	885	7
Mid_{wet}	885	0.1
$Base_{wet}$	895	0.1
$Base_{ice}$	895	7

Table 5.5 - * The base case standard run. Qv Humidity modification runs. IN runs with modified IN levels relative to the base case levels of IN.

5.1.4 Evaluation of case design runs

For the following discussion the extensions of the inversion are referred to as: 895 mb - Base, 885 mb - Mid, 865 mb - High, 835 mb - Top. The IN variation cases are denoted by 'Norm' for the IN×1 cases, 'Ice' for the IN×7 runs and 'Wet' for the IN×0.1 runs with the cases denoted with the subscript 'X_{norm}', 'X_{ice}' or 'X_{wet}'. If not explicitly stated as an alternative inversion value 'the inversion' refers to the temperature inversion.

Cloud top is higher in the Mid_{norm}, $High_{norm}$ and Top_{norm} runs than in the Base case run $Base_{NORM}$ by 40-88 m. The four different extensions above the inversion levels simulated resulted in a cloud top extention at the end of the 24 hour runs of: 25.1 m, 29.5, 54.6 m and 59.1 m using the 895 mb (Base), 885 mb (Mid), 865 mb (High) and 835 mb (Top) Q_v extensions respectively (Table 5.6).

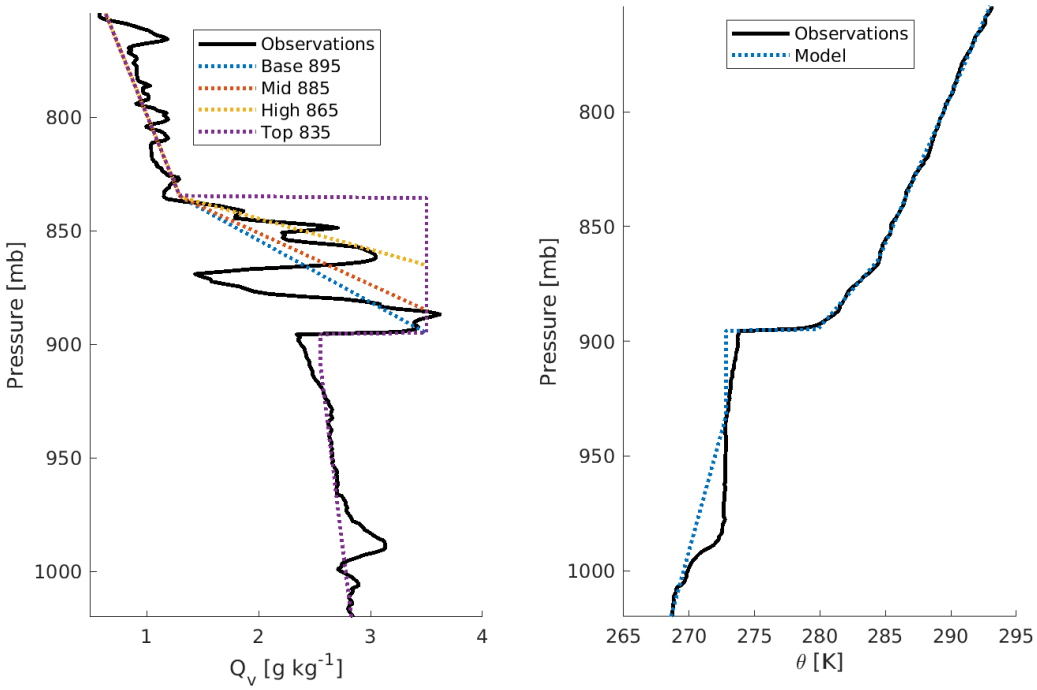

Figure 5.60 - [left] The variation of the initial specific humidity profile from the base case run $Base_{NORM}$(blue). Inversion extended aloft to 885 mb Mid_{NORM} (red), 865 mb $High_{NORM}$ (yellow) and 835 mb Top_{NORM} (purple). [right] The initial theta profile for these runs is as the base case profile theta shown in blue.

The greatest rise in cloud top is seen in the runs with higher inversion upper limits ($High_{norm}$ and Top_{norm}). Greater humidity extension aloft results in faster cloud top rise.

There is an increase in extension of liquid cloud top further above the base of the temperature inversion with greater extension of the humidity profile aloft. There is a near 30 m jump in height of the extension of cloud top into the inversion between Mid_{norm} and Top_{norm} where the extension of Q_v extends to 885 mb and 835 mb respectively. There is a 4.5 m difference, approximately one model level, between the Top_{norm} 835 mb and $High_{norm}$ 865 mb runs (Top_{norm} and $High_{norm}$) and so the large difference in the height of the humidity inversion between the two appears to have little impact on further extension of cloud above the humidity inversion. The LWP of the extended humidity runs Mid_{norm}, $High_{norm}$ and Top_{norm} were within 5% of the base case value and above the LEM base case 'grey-body' LWP threshold of 50 g m^{-2}. The IWP was higher in the extended humidity extension runs than $Base_{norm}$, increasing with increasing extension of cloud into the temperature inversion.

Run	***Cloud top [m]***	***$Z_{ctop-inv}$ [m]***	***LWP [g m^{-2}]***	***IWP [g m^{-2}]***
$Base_{norm}$	1179	25.1	71.9	0.79
Mid_{norm}	1209	29.5	69.3	0.83
Top_{norm}	1259	59.1	75.3	0.99
$High_{norm}$	1267	54.6	76.1	1.00
$High_{wet}$	1261	53.6	236.5	0.15
$High_{ice}$	1235	55.9	12.5	4.78
Mid_{ice}	1190	33.8	7.1	3.87
Mid_{wet}	1211	32.5	206.1	0.29
$Base_{wet}$	1182	26.7	189.1	0.29
$Base_{ice}$	1145	27.9	4.8	3.58

Table 5.6 - The last hour mean height of the liquid cloud top and the last hour mean height difference between the temperature inversion base (inv) and liquid cloud top (ctop). Note that IWP are given as $\times 10^{-3}$ values.

Overall the humidity modified profiles show a distinct trend in greater liquid cloud extension above the inversion with increased extension into the humidity inversion (Table 5.6, Figure 5.61). The small difference between runs Top_{norm} and $High_{norm}$ extensions above the base of the temperature inversion indicates that the Q_v profile inversion upper limit is not a limiting factor to cloud top encroachment once the humidity inversion extends to a height of 865 mb or above in this setup. The liquid water path remained close to the $Base_{norm}$ case for all the humidity extension runs with the Norm level IN (Figure 5.62).

There is a clear change in extension of cloud top into the temperature inversion with higher Q_v extension with no significant change in cloud liquid water path, though the LWP does not indicate how the liquid water is distributed in the profile.

5.1.4.1 IN variation runs

Examination of the variation in LWP and IWP with differing extensions of cloud above the base of the temperature inversion shows that there is a potential impact upon the cloud microphysics.

A range of three different IN concentrations were used at three (Base, Mid, High) Q_v extensions, the base case concentration level of 1.7 L^{-1}, low IN runs at 0.1 of the base case level (Wet) and high IN runs with 7 times the base case IN (Ice), the setup of the runs is summarised in Table 5.5. The high IN runs are known as 'Ice' and the low IN runs as 'Wet'.

The Ice runs ($Base_{ICE}$, Mid_{ICE} and $High_{ICE}$ at 895, 885, and 865 mb Qv limits respectively) show the expected increase in IWP and decrease in LWP. Higher IWP and LWP values are seen with increased extension above the base of the temperature inversion (Table 5.6). The Wet runs ($Base_{WET}$, Mid_{WET} and $High_{WET}$ at 895, 885 and 865 mb Qv limits respectively) have raised LWP and lower IWP in comparison to the Norm IN case. With higher IN the runs IWP and LWP are higher the further the extension of the liquid cloud layer above the base of the temperature inversion. The cloud tops are higher in the Wet runs for the same extension of Qv in comparison to the standard IN and Ice runs. The extension of cloud top above the temperature inversion base is similar between runs with the same initial Qv profile irrespective of the IN variation.

5.2 Time series analysis

At the start of the run all Q_v profiles were initialised with liquid cloud top at 5 m under the base of the temperature inversion (Figure 5.61). The development of cloud above the base of the temperature inversion occurs within the first hour of the simulation. During initial spin up (the first 4 hours) the Ice and Norm IN runs increase their encroachment of liquid cloud top above the temperature inversion base at the same rate, while the Wet runs extension development is slower (Figure 5.61). After the 5 hour mark a few meters in difference in the extension of liquid above the inversion base can be seen between similar initial Q_v profile setups with varying IN concentrations. The extension into the inversion of the liquid cloud top appears to be robust in terms of influence from IN variation and its impacts upon cloud development.

The $Base_{norm,Ice,Wet}$ case extension runs ($Base_{NORM}$, $Base_{WET}$ and $Base_{ICE}$) are the runs with the shallowest extension of liquid water above the temperature inversion base (Figure 5.61). The $Base_{wet}$ run ($Base_{WET}$) has the highest variability of extension into the inversion. The runs with an extension Mid show increased extension into the inversion in comparison to the Base case. The extension of liquid cloud above the temperature inversion for the Mid run decreases from a peak at 10 hours of around 40-45 m to 30-35 m during the last hour. It is probable that the reduction in extension during the later part of the run is because the upper limit of the Mid 885 mb humidity extension has been reached while the temperature inversion continues to rise due to entrainment. A drop in humidity aloft then results in the extension of liquid cloud into the inversion being gradually eroded. The highest extension Q_v profile extension runs of up to 865 mb (High) and 835 mb (Top) show little difference in their evolution of the extension of liquid cloud above the temperature inversion throughout the 24hr simulation. There is a rise in cloud top between run hours 5-17 of 5 m with the liquid cloud top rising roughly another 15 m over the last seven hours of the simulation ending with liquid cloud top between 50m and 60 m above the temperature inversion base. The change in the rate that liquid cloud extends above the temperature inversion base after 17 hours of run time points to a shift in the cloud and or boundary layer stability and structure part way through the run.

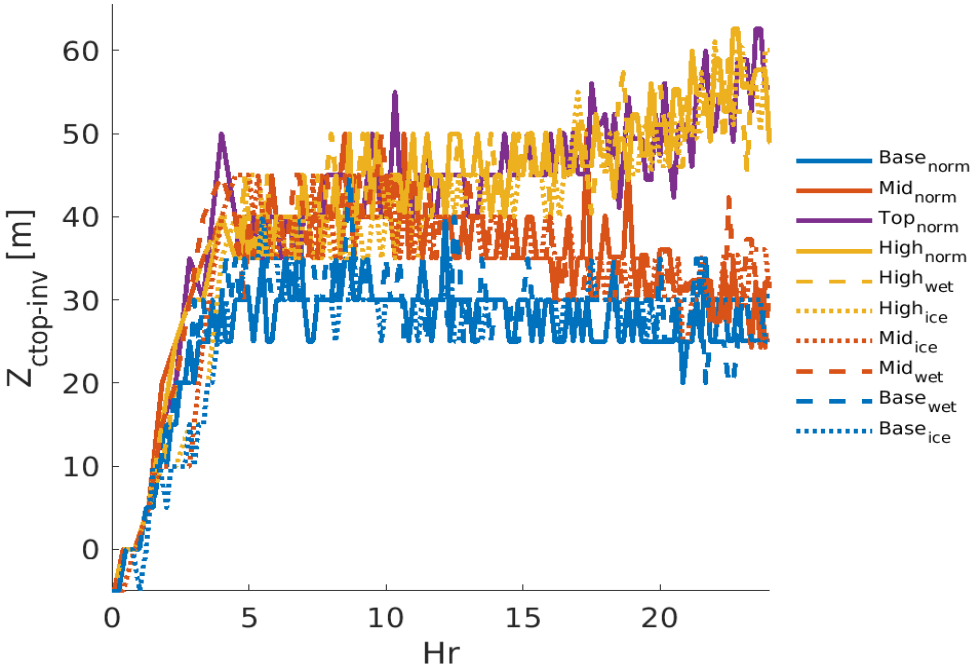

Figure 5.61- Time series of extension of liquid cloud top (ctop) above the base of the temperature inversion (inv) for the runs used in detailed analysis.

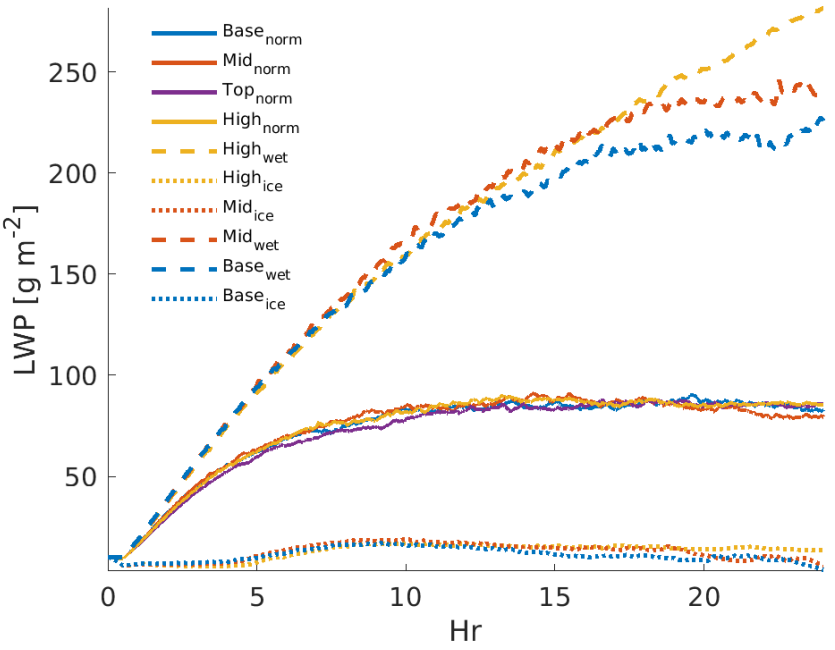

Figure 5.62 - Time series showing the development of the column LWP for the different initial humidity profiles (extension into the inversion) and IN concentrations.

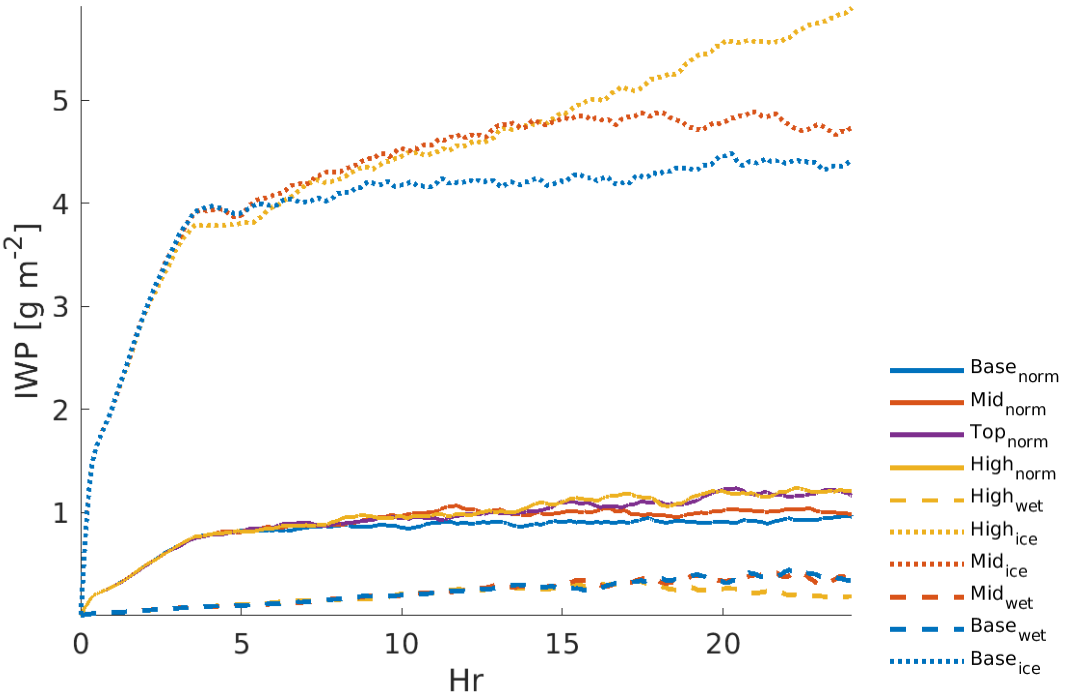

Figure 5.63 - Time series showing the development of the column IWP for the different initial humidity profiles (extension into the inversion) and IN concentrations.

The Ice runs ($High_{ICE}$, Mid_{ICE}, $Base_{ICE}$) all reside within the 'grey-body' tenuous cloud regime throughout the run (Figure 5.62). The spread in LWP between the high IN runs is within 10 g m^{-2} but as they are in the 'grey-body' zone for LW radiation they have a wide range of LW cooling peak values, the last hour mean peak LW cooling being -29.4, -49.0 and -82.7 K day^{-1} for $High_{ice}$, Mid_{ice} and $Base_{ice}$ respectively. Consequently the IN runs have potentially varying cloud mixed layers and turbulence values. All the standard IN runs are well within the range of LWP associated with black-body radiation and so the variation in LWP itself is unlikely to have an impact upon cloud driven turbulence. The Wet runs show a very definite separation in LWP at the end of the simulations. At the end of the run time the Wet runs have a range of LWP of over 50 g m^{-2}. The response of the cloud layer in low IN conditions is altered by the initial Q_v profile modifications.

There is clear differentiation in the IWP between the Ice, Norm and Wet runs (Figure 5.63). Of the Ice runs ($High_{ICE}$, Mid_{ICE} and $Base_{ICE}$) IWP concentrations at the end of the run time span 4-6 × 10^{-3} kg m^{-2}. The highest ice concentrations are observed in run $High_{ice}$, which is the high IN run with

the furthest extension into the inversion. In run $High_{ice}$ ice concentration levels in terms of IWP never reach a steady level during the 24 hours of the run. The base level IN runs IWP's are higher for the runs with Top_{norm} and $High_{norm}$ (runs Top_{NORM} and $High_{NORM}$).

5.3 Impact of the variation of extension of cloud above the temperature inversion

The structure of liquid water can impact the depth that radiative cooling occurs over (e.g. Garret et al., 2002) and so alter the buoyancy and turbulence production. The radiative cooling profiles and their evolution are examined alongside the profiles of cloud liquid, ice concentrations, specific humidity and turbulence in terms of dissipation rate and vertical velocity variance.

5.3.1 Q variables

5.3.1.1 Evolution of the Norm levels of IN runs

5.3.1.1.1 LWP

The upper relative limit of the extension of liquid water above the inversion is higher the greater the extension of the humidity inversion aloft (Figure 5.64e,f). The LWP time series (Figure 5.62) for the Norm cases show marginally higher (but small at 5%) LWP values for the $High_{norm}$ and Top_{norm} runs in comparison to the $Base_{norm}$ and Mid_{norm} towards the end on the 24 hour simulation. The slight difference in LWP values is attributable to the increased liquid water content above the temperature inversion in the $High_{norm}$ and Top_{norm} runs as the simulations progress (Figure 5.64b,d,f).

5.3.1.1.2 IWP

At 12 hours into the Norm runs there is little observable difference between the IWP in the Mid_{norm}, $High_{norm}$ and Top_{norm} runs (Figure 5.63 and Figure 5.65a,b). The Top_{norm} run at 12 hours has a reduced ice concentration throughout the profile at both peak concentrations and in the sub-cloud layer (roughly under Z/Zib of 0.5). Six hours later at 18 hrs of run time the runs Top_{norm} and $High_{norm}$ are still matched in terms of IWP and profile, and remain so at the 24 hour point (Figure 5.65c,e). At 18 hours the Mid_{norm} run has reduced ice water content closer to the values of that in $Base_{norm}$. As the IN

concentration is the same for all 4 Norm IN runs the increase in IWP in the lower half of the profile with further extension into the inversion must be due to the response of the cloud layer to the variation in Q_v.

5.3.1.1.3 Specific humidity

The humidity inversion peak value decreases from the 3.5 g kg^{-1} as cloud top encroaches upon the Q_v extension (Figure 5.66). The humidity inversion has already begun to be eroded for Top_{norm} (895 mb extension) at 12 hours (Figure 5.66a). The cloud top extension above the temperature inversion for run Mid_{norm} decreases after ~10 hrs of simulation time (Figure 5.61) as Q_v erosion aloft limits liquid cloud top extension (Figure 5.66a,c,d). The humidity inversion has not been fully eroded at 24 hours for either the Top_{norm} or $High_{norm}$ runs (Figure 5.66a,c,d), and no difference between the liquid cloud top extensions is observed between those two runs.

5.3.1.1.4 Detailed look at the 23-24 hour Q profiles

The $High_{norm}$ and Top_{norm} runs show more ice present under cloud base but similar amounts in cloud to the runs $Base_{norm}$ and Mid_{norm} (Figure 5.65e). Peak ice water content is located under the height in the profile peak in liquid water content for all runs. The ice primarily forms under the height of the layer of super cooled water that resides at cloud top, as observed in Shupe et al. (2012). More liquid water available at cloud top has the potential to allow for more ice formation and sedimentation to the lower layers. The peak in ice concentration for all runs is just under the profile peak in liquid water concentration.

For Norm runs the liquid water profiles are of a similar shape and peak concentration underneath the base of the temperature inversion. The peak in liquid water occurring under the inversion base at the same relative depth for all Norm extensions into the inversion (Figure 5.64e). The extension of cloud above the base of the temperature inversion is higher in the Top_{norm} and $High_{norm}$ runs than the Mid_{norm} and $Base_{norm}$ runs (Figure 5.64f).

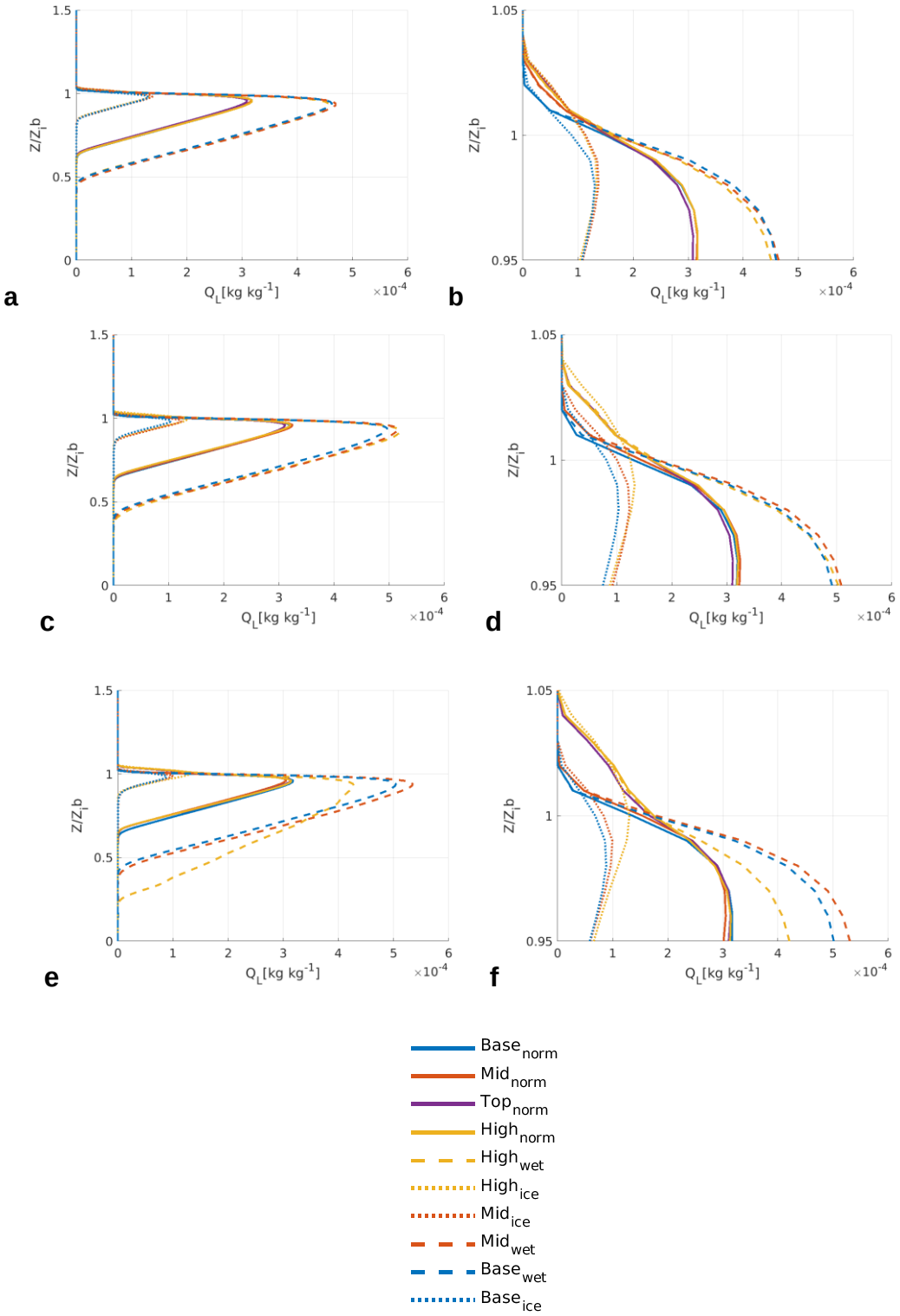

Figure 5.64 - Mean profiles of liquid water mixing ratio from a,b) 12hrs c,d)18hrs e,f)24 hrs, normalized in height relative to the base of the temperature inversion (Z_{ib}). Plots b, d and f are zoomed versions of a, b and c respectively. A value of Z/Z_{ib} equal to 1 being the inversion base and 0 being the surface.

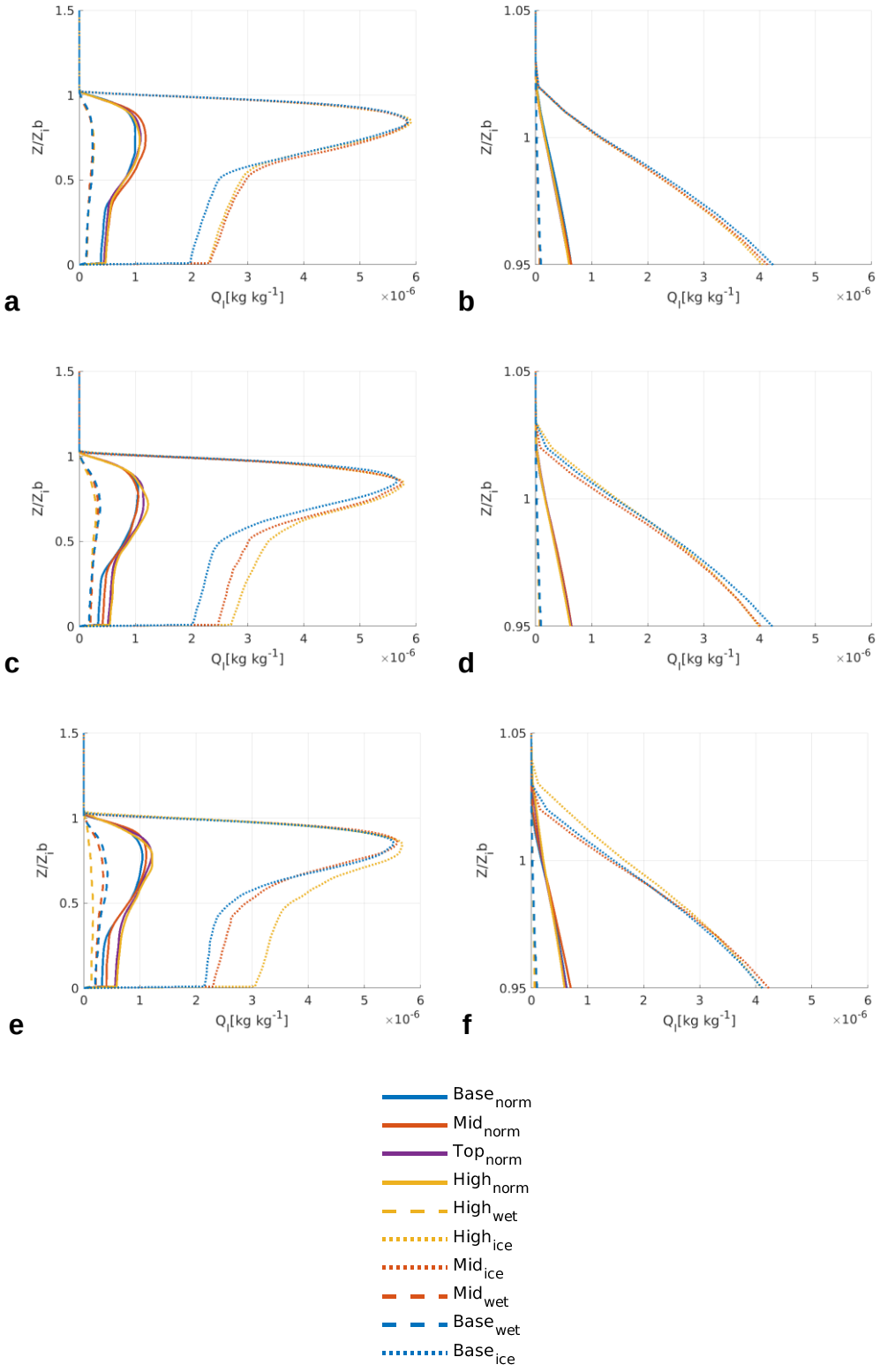

Figure 5.65 - Mean profiles of ice mixing ratio from a,b) 12hrs c,d) 18hrs e,f) 24 hrs, normalized in height relative to the base of the temperature inversion (Z_{ib}). Plots b, d and f are zoomed versions of a, b and c respectively. A value of Z/Z_{ib} equal to 1 being the inversion base and 0 being the surface.

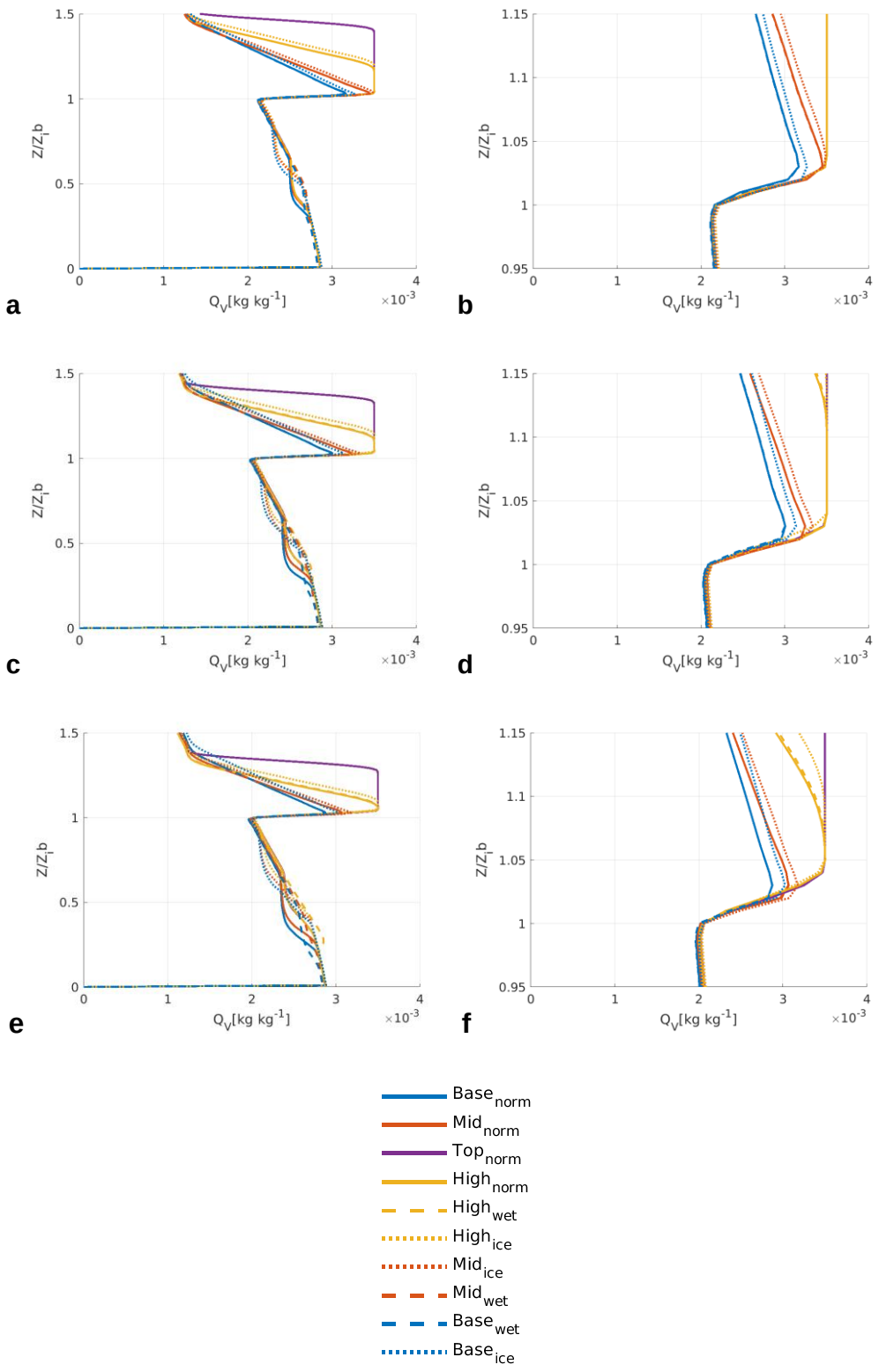

Figure 5.66 - Mean profiles of specific humidity from a,b) 12hrs c,d)18hrs e,f)24 hrs, normalized in height relative to the base of the temperature inversion (Z_{ib}). Plots b, d and f are zoomed versions of a, b and c respectively. A value of Z/Z_{ib} equal to 1 being the inversion base and 0 being the surface.

The normalised profiles of humidity demonstrate that as the cloud layer entrains air and grows upwards into the humidity inversion the humidity inversion depth is eroded (Figure 5.66e,f). At 24 hours the inversion for $Base_{norm}$ and Mid_{norm} have been eroded away from the 3.5 g kg^{-1} peak with $Base_{norm}$ (895 mb) having lower water vapour concentrations aloft than Mid_{norm} (885 mb). For the Norm liquid level runs where encroachment into the inversion varies, in-cloud specific humidity's are slightly lower for the $Base_{norm}$ and Mid_{norm} runs than for the $High_{norm}$ and Top_{norm} runs. The vertical boundary of liquid water extension into the inversion is not limited by the height of the humidity inversion between $High_{norm}$ and Top_{norm} runs so the liquid water extension aloft is the same in both runs.

5.3.1.2 IN variation runs: Q variables

The highest liquid water concentrations are in the Wet runs Mid_{wet} and $High_{wet,}$ Mid_{wet} having the highest peak liquid water concentrations during the last hour of the run (Figure 5.64e,f). The run $High_{wet}$ has the deepest extension of liquid water down through the boundary layer. The Ice runs have the lowest liquid water concentrations and show a peak in liquid water at or just under the base of the temperature inversion. The $High_{ice}$ run has a higher peak in liquid water in both relative height and concentration than the Mid_{ice} and $Base_{ice}$ runs. The peak in liquid water occurring at the inversion in $High_{ice}$ and at a Z/Zib of 0.98 in the Mid_{ice} and $Base_{ice}$ runs at 24 hours run time (Figure 5.64f).

The Wet run Mid_{wet} has higher ice concentrations than $High_{wet}$ (Figure 5.65e). The run $High_{wet}$ has no discernable peak in ice water concentration just a steady rise from the base of the inversion to the surface. $Base_{wet}$ and Mid_{wet} have a broad peak in ice concentrations consistent with the height of the peak ice concentrations in the Norm IN runs. Above cloud the Ice runs show less erosion of the Qv inversion in 24 hour simulation time than the Wet runs for the same extension into the inversion (Figure 5.66e,f). The cloud layers in the low Ice runs entrain less and cloud top rises at a slower rate.

5.3.2 Radiation fluxes

As an overview at 24 hours of simulation time the peak radiative cooling for $Base_{norm}$ and Mid_{norm} is greater, sharper and lower down in the profile than the $High_{norm}$ and Top_{norm} runs (Figure 5.67e,f). The runs $High_{norm}$ and Top_{norm} have

a LW radiation peak above the temperature inversion base and have a broader peak than Mid_{norm} and $Base_{norm}$. There is a slight secondary peak in the $High_{norm}$ and Top_{norm} runs at the height coincident with that of the peak cooling for the $Base_{norm}$ and Mid_{norm} runs at 24 hours (Figure 5.67f). Further extension into the inversion acts to extend the LW cooling up into the inversion and reduces the peak cooling value.

To elaborate the peak LW cooling decreases after the initial spin up for the cloud top extension runs $High_{norm}$ and Top_{norm} until about 15 hours into the simulation.

After 15 hours of simulation time there is a linear increase in the peak LW cooling for both $High_{norm}$ and Top_{norm} (Figure 5.68). The increase and difference between the runs partly due to the narrowing of the LW peak as the cooling further shifts into the inversion (Figure 5.67b,d,e). As the runs progress the peak cooling becomes narrower and stronger.

In general extension of the liquid cloud layer above the temperature inversion base alters the structure of LW cooling within the cloud. The lower the extension of liquid cloud into the temperature inversion the higher the peak cooling and the further the peak is down the profile. Deeper extensions of cloud above the base of the temperature inversion give rise to broader LW peaks that span the temperature inversion base with lower peak cooling values, until the point the LW cooling shift further up into the inversion and the LW peak value increases.

5.3.2.1 IN variation runs: Radiation

Peak cooling for the Wet runs is located at the same height as that seen in the Norm level IN runs (Figure 5.67). For the Wet runs the higher into the inversion they extend the weaker the peak LW cooling. Peak cooling for the Ice runs is significantly less than for the Norm and Wet runs. LWP values for the Ice are within the grey-body radiative range(sun 50 g m^{-1}) where changes in the clouds LWP have an impact upon the LW cooling.

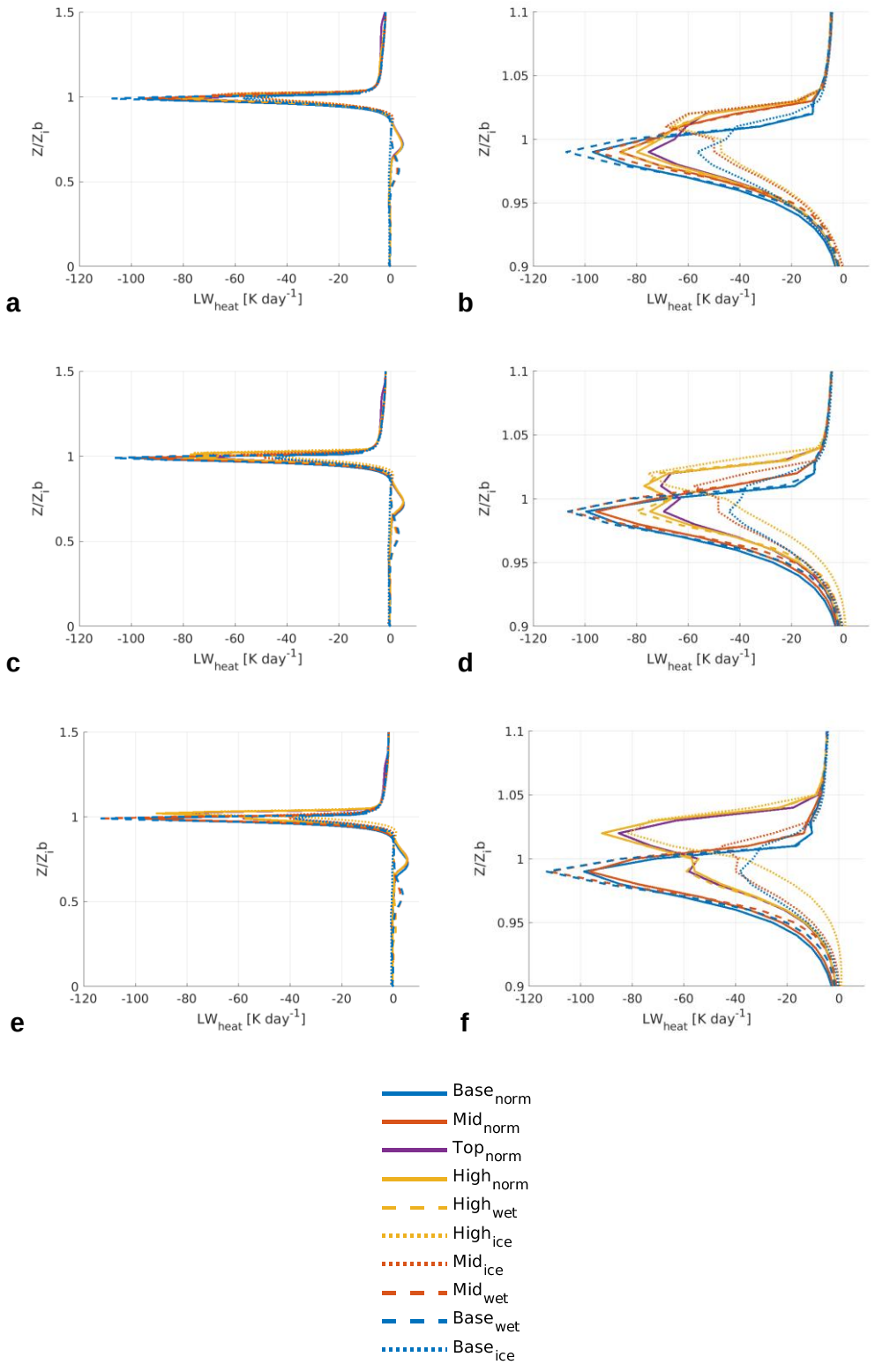

Figure 5.67 - Mean profiles of LW heating from a,b) 12hrs c,d)18hrs e,f)24 hrs, normalized in height relative to the base of the temperature inversion (Z_{ib}). Plots b, d and f are zoomed versions of a, b and c respectively. A value of Z/Z_{ib} equal to 1 being the inversion base and 0 being the surface.

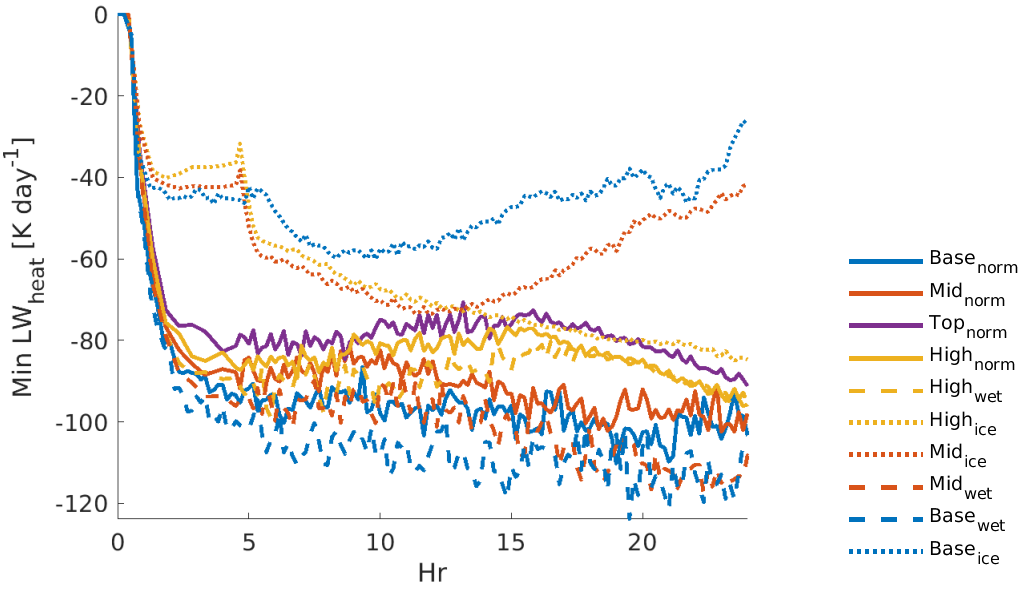

Figure 5.68 - Time series of the peak in cooling in the profile for the length of the entire run length.

The development of the LW cooling peak values through the simulation for the Wet runs follows the trends of the Norm IN runs (Figure 5.68). In the wet runs the higher the extension of cloud top into the inversion the weaker the LW cooling, $High_{wet}$ having a weaker peak cooling in comparison to Mid_{wet} which has weaker peak LW cooling to $Base_{wet}$.

The Ice runs show stronger peak LW cooling the deeper the extension of cloud into the inversion lowest at $Base_{ice}$ highest at $High_{ice}$. Extension into the inversion has an altered LW cooling response at higher and lower IN concentrations, more ice resulting in stronger cooling with greater extension into the inversion and lower levels of ice associated with greater cooling with less extension into the inversion (Figure 5.67).

There are two separate regimes of responses to variation in extension of liquid cloud above the inversion (Figure 5.69). Regime one is a rise in LW cooling with greater extension into the inversion for high IN concentrations as in the Ice cases. The other being a drop in cooling with increase in extension depth for low and standard level IN runs in the Norm and Wet cases.

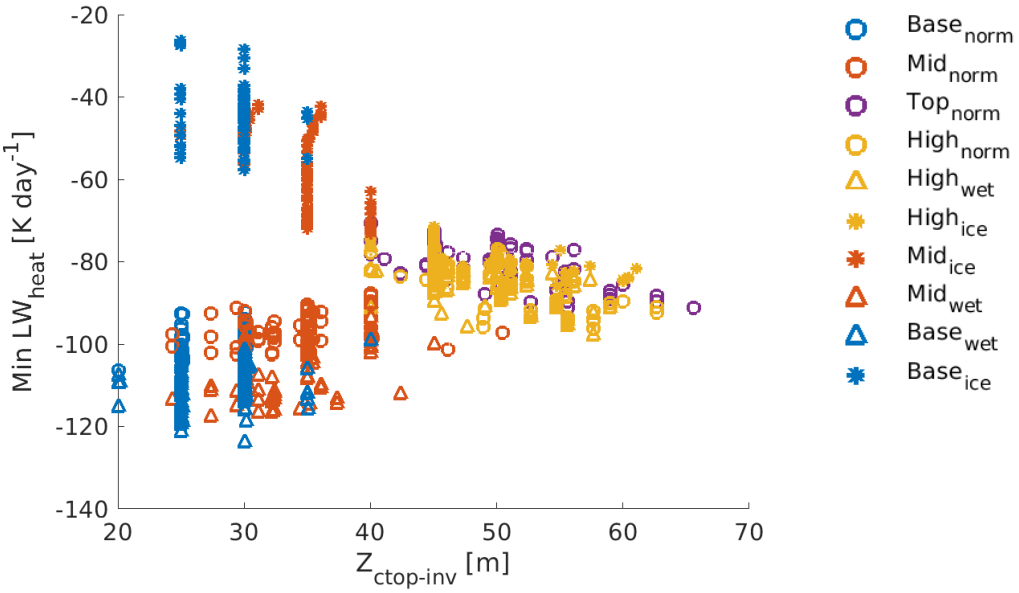

Figure 5.69 - The final 12 hours of 10 min average LW heating against the depth liquid cloud extends above the base of the temperature inversion ($Z_{ctop-inv}$). Colours of the points indicate the top of the humidity inversion extension, cyan (base case) 895 mb, blue 885 mb, purple 865 mb and magenta 835 mb. The shape of the points indicate the IN multiplication factor, ○ represents the base level of IN as used in the base case, △ represents 0.1 times the base IN, ✳ represents 7 of the base case IN.

The drop in LW cooling with increased extension into the inversion is explained by the shift in the height of the LW peak. The LW peak reduces due to the greater depth that the LW peak extends over as cloud extends further into the inversion. The increase in LW cooling with extension depth as with the extensions of Q_v to 865 mb and 835 mb is due to the narrowing of the peak in cooling as it fully shifts above the inversion.

At the lower Q_v extensions of 895 mb and 885 mb the different IN variations alter the response of the LW cooling to the extension into the inversion. The Ice runs LWP are in the 'grey-body' range and so variations in LWP at this stage will alter the LW response, the higher into the extension runs have slightly higher liquid water aloft and so will have greater LW radiative cooling due to the increased water that condenses with higher extensions into the inversion.

The Norm and Wet runs have a LWP within the black-body LWP range. As the $High_{norm,wet}$ and Top_{norm} runs shift their cooling peak up into the inversion the

peak value drops as the depth cooling extends over increases (Figure 5.67b-d). As the cooling shifts further up into the inversion in the $High_{norm,wet}$ and Top_{norm} runs the LW cooling peak narrows and the peak values increase again (Figure 5.67d-f) but the original LW peak was already at the black-body LW cooling value so the peak LW values do not increase beyond the starting value once the cooling moves further up into the inversion.

5.3.3 Potential temperature tendency due to microphysics

A positive value for temperature tendency due to microphysical changes indicates that condensation and or freezing is occurring. Latent heat is released as the water changes to a lower energy phase, the converse being true for changes to a higher energy state by evaporation.

The peak warming tendency due to microphysical changes for all runs is at the height of the peak radiative cooling (Figure 5.67, Figure 5.70). The large positive peak in the potential temperature tendency is due to the release of latent heat from the condensation of water vapour due to radiative cooling. The heating from condensation will offset part of the cooling from LW emission. The peak warming tendency is slightly greater for the $High_{norm}$ and Top_{norm} runs than the Mid_{norm} and $Base_{norm}$ runs and over a greater depth. The LW cooling peak is weaker in the $High_{norm}$ and Top_{norm} runs than the Mid_{norm} and $Base_{norm}$ and so the warming will offset more of the cooling in the $High_{norm}$ and Top_{norm} runs.

The region around the base of the temperature inversion and where the peak LW cooling is located (Figure 5.67) is the location of the peak warming due to microphysical changes in the profiles of the temperature change due to microphysics at 12,18 and 24 hours (Figure 5.70). At cloud top the warming is mostly due to the condensation of water caused by the cooling due to the LW forcing in the high humidity aloft. The shape and evolution of the warming around the inversion base height is paralleled by the shape and evolution of the LW cooling profiles. Half way down the relative boundary layer height there is a smoother secondary peak in cooling due to phase changes, the lower peak being primarily attributable to the sublimation and melting of ice crystals.

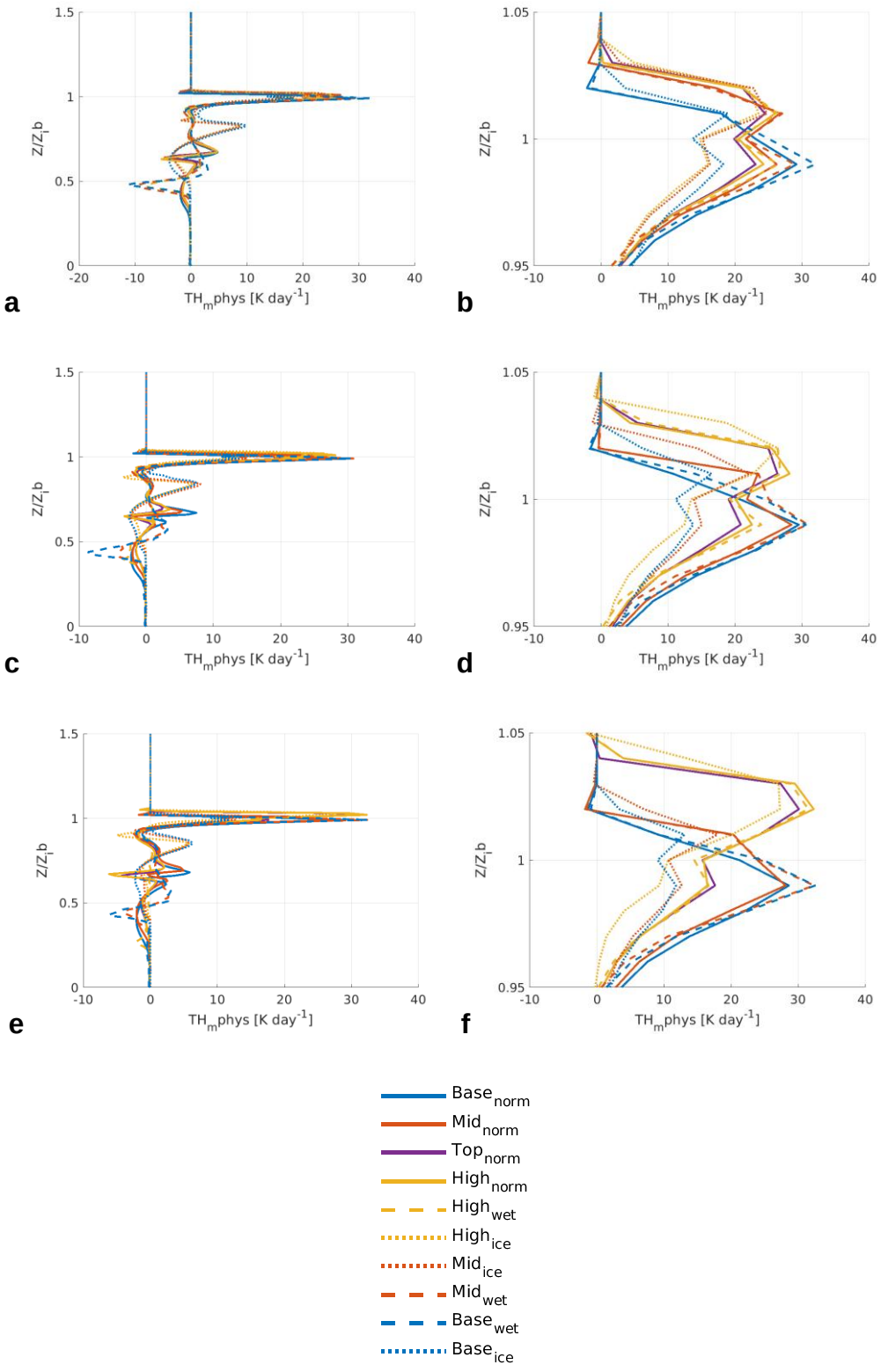

Figure 5.70 - Mean profiles of The potential temperature tendency due to changes in the microphysics, water phase from a,b) 12hrs c,d)18hrs e,f)24 hrs, normalized in height relative to the base of the temperature inversion (Z_{ib}). Plots b, d and f are zoomed versions of a, b and c respectively. A value of Z/Zib equal to 1 being the inversion base and 0 being the surface.

5.3.3.1 IN variation: Potential temperature tendency

The Wet runs have only slightly greater peak heating due to changes in the microphysics than the equivalent cloud top extension (High, Mid, Base) Norm IN runs (Figure 5.70). Increased liquid water production aloft is minimal and all Qv levels for the Wet runs (High, Mid, Base) show similar percentage rises in LWC and time series responses relative to their Qv Norm IN case equivalent (Figure 5.64b,d,f).

The Ice runs have reduced peak warming due to microphysics changes in comparison to equivalent cloud top extension (High, Mid, Base) Norm IN runs (Figure 5.70). The two runs $Base_{ice}$ and Mid_{ice} are roughly 2×10^{-4} K s^{-1} less than the $Base_{norm}$ and Mid_{norm} runs. The response of the $High_{ice}$ run ($High_{ICE}$) is a smaller reduction in peak warming due to microphysics changes than the $Base_{ice}$ and Mid_{ice} runs. The liquid water production is greater in the $High_{ice}$ run than the $Base_{ice}$ and Mid_{ice} runs. The extension into the inversion acts as a factor for promoting the production of liquid water from water vapour in the cloud layer above the inversion.

The change from Ice to Norn to Wet case liquid levels results in slightly greater heating due to microphysical changes as a result of greater levels of condensation. Condensation is inhibited by the presence of IN as more water vapour is taken up to grow ice than water due to the vapour pressure difference (the Wegener–Bergeron–Findeisen process) .

In the Ice cases the response of warming due to microphysics changes is different between the $Base_{ice}$, Mid_{ice} runs and the $High_{ice}$ run at 24 hours. The warming is reduced substantially relative to the $Base_{norm}$ (3.33×10^{-4} K s^{-1}) and Mid_{norm} (3.26×10^{-4} K s^{-1}) runs for the $Base_{ice}$ (1.52×10^{-4} K s^{-1}) and Mid_{ice} (2.08×10^{-4} K s^{-1})runs. The warming due to microphysics is only slightly reduced for the $High_{ice}$ (3.68×10^{-4} K s^{-1}) run relative to $High_{norm}$ (3.76×10^{-4} K s^{-1}). More of the LW cooling is going into the production of liquid water in the $High_{ice}$ run than to LW cooling once the Ice runs cloud top and cooling peak extends fully into the inversion.

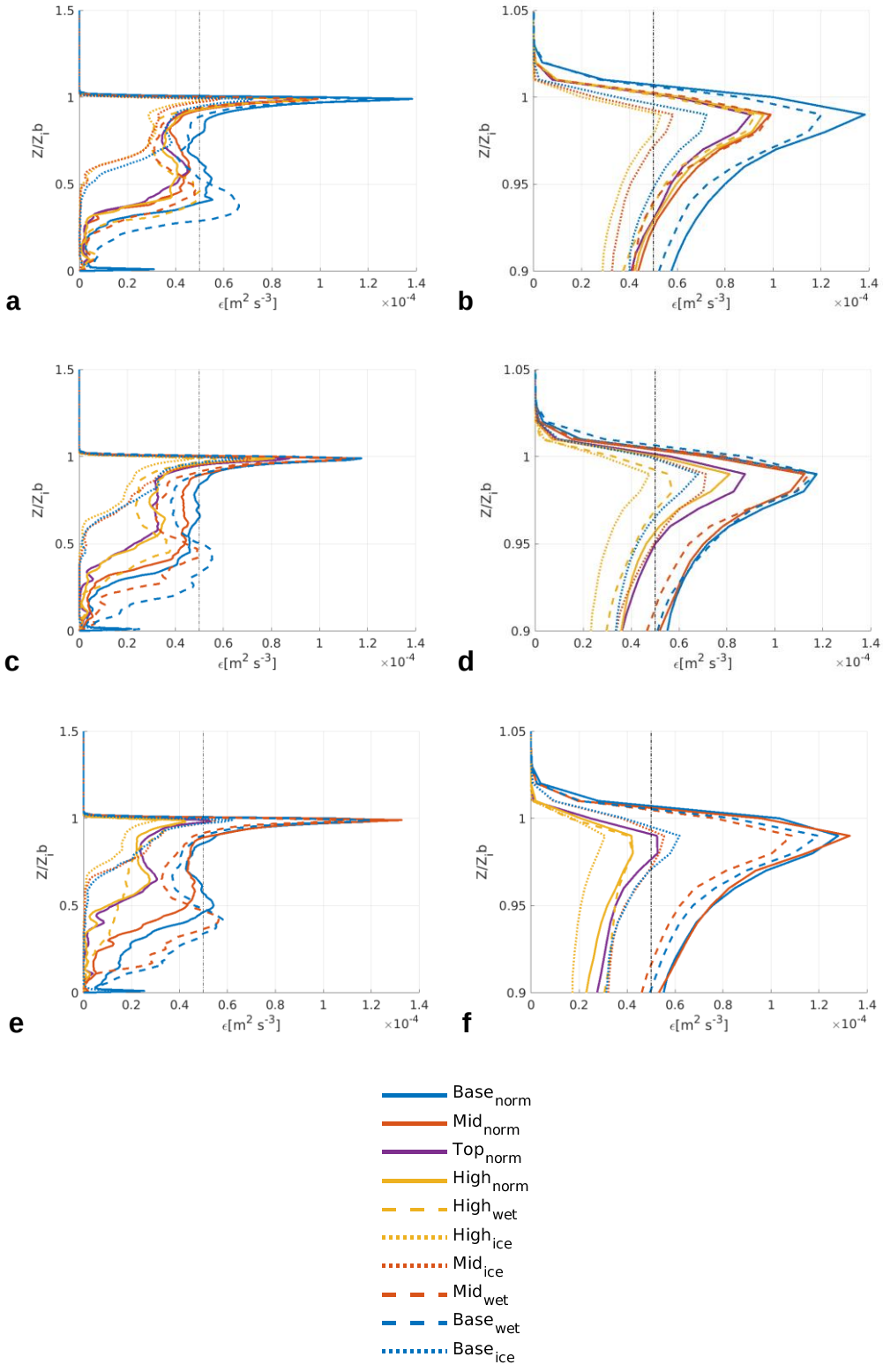

Figure 5.71 - Mean profiles of the dissipation rate from a,b) 12hrs c,d)18hrs e,f)24 hrs, normalized in height relative to the base of the temperature inversion (Z_{ib}). Plots b, d and f are zoomed versions of a, b and c respectively. A value of Z/Zib equal to 1 being the inversion base and 0 being the surface.

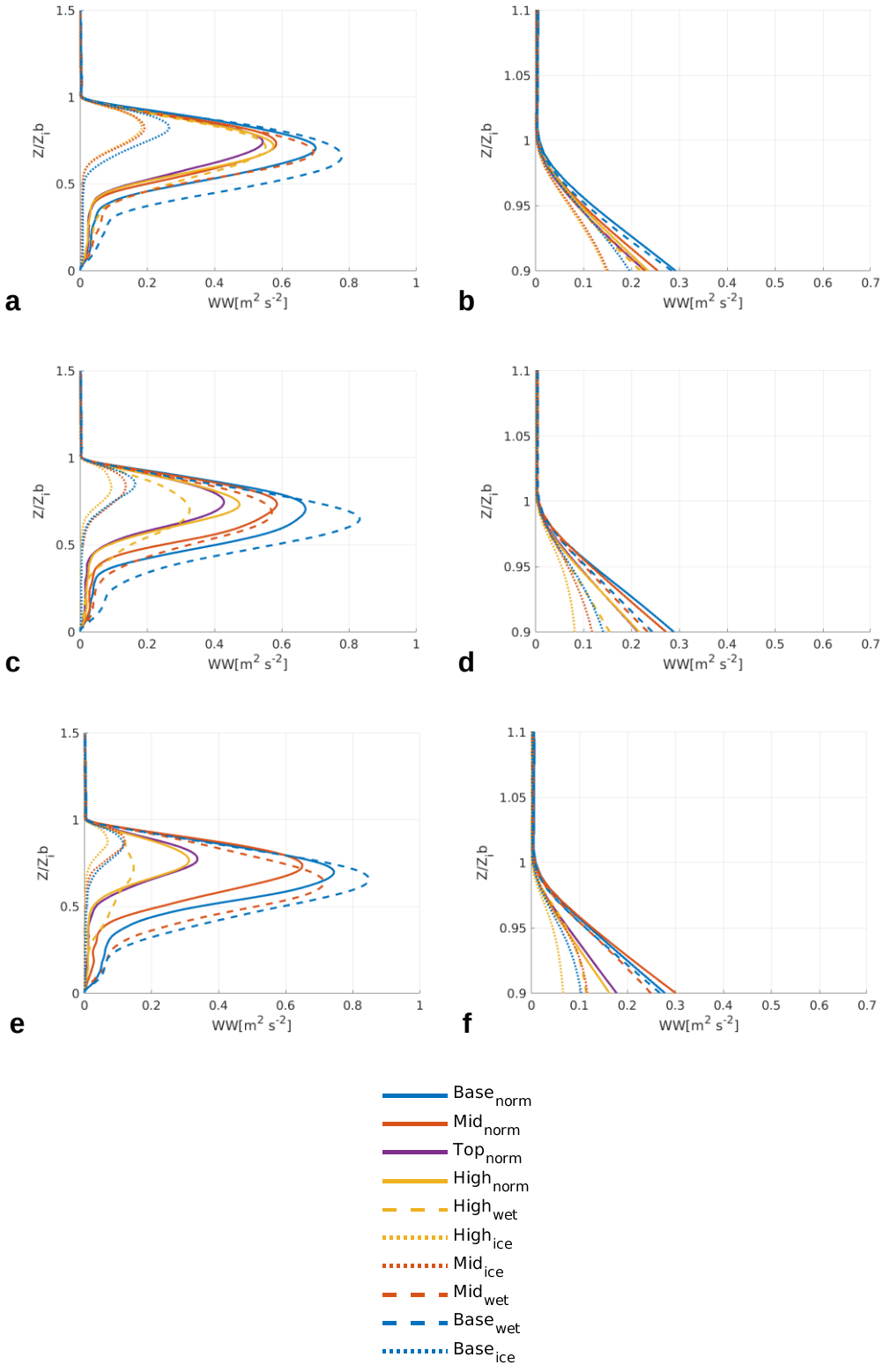

Figure 5.72 - Mean profiles of vertical velocity variance from a,b) 12hrs c,d)18hrs e,f)24 hrs, normalized in height relative to the base of the temperature inversion (Z_{ib}). Plots b, d and f are zoomed versions of a, b and c respectively. A value of Z/Zib equal to 1 being the inversion base and 0 being the surface.

5.3.4 Turbulence

Here the dissipation rate profiles and the vertical velocity variance profiles are examined to provide insight into the behaviour of the turbulence in response to variation in the extension of cloud top into the temperature inversion. Dissipation rate is used in the previous chapters as a proxy for turbulence intensity and so is examined here to show equivalence between the conclusions in terms of dissipation rate and vertical velocity variance.

5.3.4.1 Dissipation rate

Peak dissipation rate for all Ice, Norm and Wet cases is located just under the base of the temperature inversion. Dissipation rates then decrease in the cloud layer to varying extents with the sub-cloud behaviour variable between the Ice, Norm and Wet runs (Figure 5.71).

The Top_{norm} and $High_{norm}$ runs show lower dissipation rates than the Mid_{norm} and $Base_{norm}$ runs throughout the profile depth. The general shape of all the Norm runs is similar in structure with a sharp peak at the inversion base followed by a decline of dissipation rate throughout the cloud layer with a secondary boarder peak in the region of the liquid cloud base and area of LW warming.

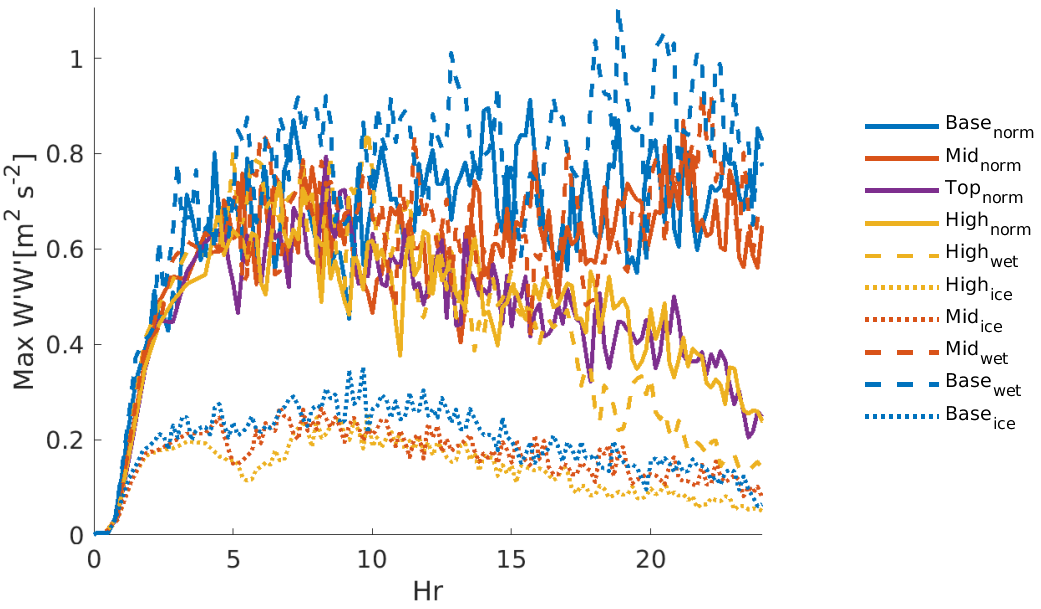

Figure 5.73 - Evolution in time of the peak vertical velocity variance.

The Top_{norm} and $High_{norm}$ runs have a shallower cloud layer and so the dissipation rate trends towards zero at a relative height of ~0.6 to 0.4 Z/Zib at 24 hours(Figure 5.71e) and remains at a sub 0.05×10^{-4} $m^2 s^{-3}$ to the surface. Little difference is seen in the shape or magnitude of dissipation rate between Top_{norm} and $High_{norm}$. The Mid_{norm} and $Base_{norm}$ runs peak at ~1.2×10^{-4} $m^2 s^{-3}$ dropping to just under 0.5×10^{-4} $m^2 s^{-3}$ through the cloud layer for $Base_{norm}$ and Mid_{norm}. The Mid_{norm} relative to $Base_{norm}$ shows weaker dissipation rates throughout the profile under the peak.

5.3.4.2 Vertical velocity variance

The higher Top_{norm} and $High_{norm}$ both have reduced vertical velocity and dissipation rate magnitudes throughout their profiles in comparison to Mid_{norm} and $Base_{norm}$ (Figure 5.72). Mid_{norm} exhibits a weaker peak in vertical velocity variance than $Base_{norm}$ which has a shallower extension above Z_{ib}. Increased extension into the inversion is associated with a reduction in cloud driven turbulence.

There is a clear variation in w'w' between the four Norm runs ($Top_{norm,}$ $High_{norm,}$ Mid_{norm} and $Base_{norm}$) over the evolution of the runs. At 12-13 hours into the runs $Base_{norm}$, has the highest peak in w'w' with higher values throughout the profile depth (Figure 5.72a). Peak w'w' at 12 hrs is roughly 3/4 of the way up the boundary layer. Peak w'w' values dropping off until just under half way down the boundary layer at which point there is only a slight decrease in w'w' until just above the surface at which point w'w' goes to zero. As the Norm runs progress the difference between the Top, High, Mid, $Base_{norm}$ runs increases. At 18 hrs the mean w'w' profiles for Top_{norm} and $High_{norm}$ have decreased in peak strength(Figure 5.72c). The shallower extension run of Mid_{norm} has increased w'w' to a similar magnitude as $Base_{norm}$, which has itself decreased. The w'w' peak of run $Base_{norm}$ remains at a lower relative height than the other three Norm runs. At the end of the simulation the higher into the inversion runs of Top_{norm} and $High_{norm}$ have w'w' peak values at roughly half their value at 18 hrs. The height of the peak for Top_{norm} and $High_{norm}$ has raised slightly and the peak w'w' has dropped for Mid_{norm} and $Base_{norm}$ runs at 24 hours (Figure 5.72e).

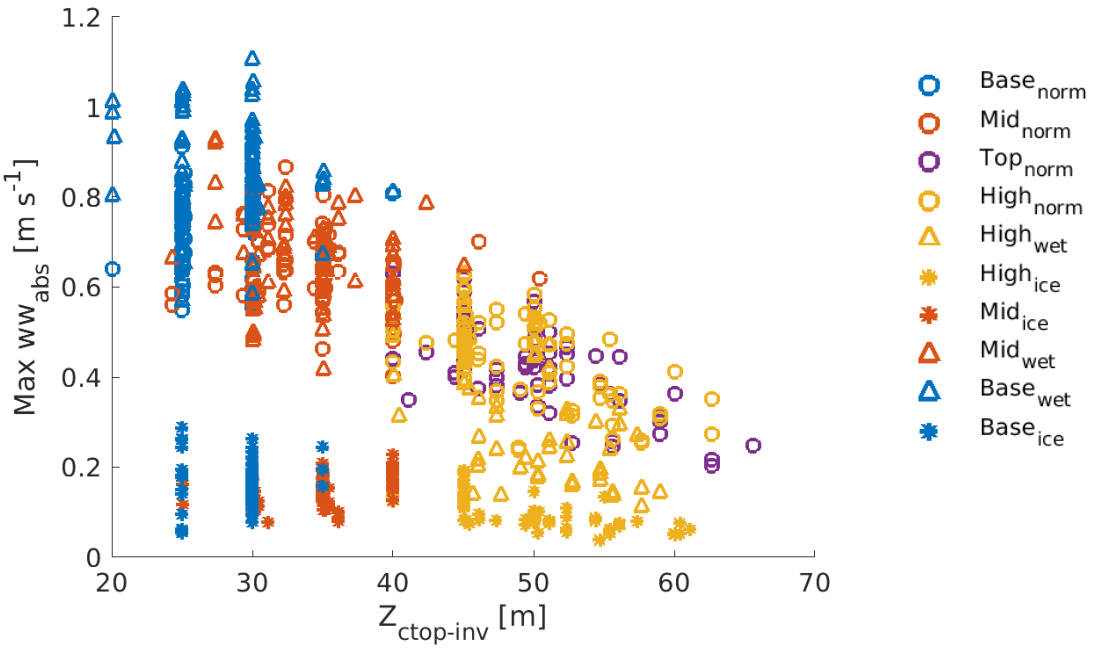

Figure 5.74 - Peak vertical velocity variance vs the depth of the extension of cloud into the inversion.

The time series of peak w'w' for the Top_{norm} and $High_{norm}$ runs peaks at 7-8 hrs then decreases, with the rate of decrease increasing after 20 hours (Figure 5.73). The Mid_{norm} run follows the same shape as the Top_{norm} and $High_{norm}$ runs until ~10 hrs at which point the w'w' of Mid_{norm} run increases to a level just under that of $Base_{norm}$. The $Base_{norm}$ has the highest w'w' values of all the Norm runs.

There is a clear negative correlation between extension of the liquid cloud layer above the base of the temperature inversion and the vertical velocity variance (Figure 5.74). It is clear that the impacts that Qv extension has upon the cloud layer reduces the cloud driven turbulence and is a significant factor that could alter the boundary layer turbulent structure all other factors being equal. Turbulence is weaker and peaks higher up in the profile the higher cloud top extends above the base of the temperature inversion, in line with the behaviour of peak in liquid water content and LW cooling profiles.

5.3.4.3 IN variations: Vertical Velocity Variance

To summarise the magnitude of w'w' is reduced in all the Ice runs relative to their Norm (High,Mid,Base) equivalent runs (Figure 5.72). The w'w' profiles are similar in both shape and magnitude between the $Base_{ice}$ and Mid_{ice} runs.

The $High_{ice}$ run shows reduced w'w' peak magnitude and a peak higher up the profile in comparison to the $Base_{ice}$ and Mid_{ice} runs.

The Wet runs of $Base_{wet}$ and Mid_{wet} w'w' profiles are at a higher magnitude than the $Base_{norm}$ and Mid_{norm} runs. The w'w' profile for the $High_{wet}$ run is weaker than the $High_{norm}$ run and has a different shaped profile at 24 hours (Figure 5.72e). The w'w' profile for $High_{wet}$ is the same shape and magnitude as the $High_{norm}$ run at 12 hours (Figure 5.72a) and reduces in magnitude and changes shape, broadening, as the runs progress (Figure 5.72a-c-e).

5.4 Conclusions

In the Arctic mixed phase stratocumulus the cloud liquid water often extends above the temperature inversion at boundary-layer top and so cooling begins above the base of the temperature inversion, where it would start for a mid-latitude pure water stratocumulus cloud. Cooling therefore begins above the temperature inversion base, altering the cooling profile relative to that of a mid-latitude stratocumulus cloud.

Through the use of a series of LEM simulations, with adapted specific humidity profiles the depth of cloud top extension into the temperature inversion was modified. The variation of depth of cloud extension was related to turbulence, cloud LW heating rates and liquid and ice water contents.

The specific humidity above the temperature inversion was a limiting factor in the extension of cloud top above the base of the temperature inversion when the humidity extension is lower than 865 mb. Above the 865 mb extension level the temperature profiles the limiting factor in these runs achieving super saturations in the layer above the cloud. The humidity inversion aloft was altered to give a range of cloud top extension into the inversion of 25.1 m to 59.1 m during the last hour of the simulation.

The higher the extension of cloud top above the temperature inversion base the greater the concentration of liquid water within the inversion. The greater the concentration of liquid water within the inversion the greater the LW cooling within the inversion. LW cooling within the temperature inversion primarily results in condensation rather than a temperature decrease. The

condensation occurring due to LW cooling results in latent heating offsetting a portion of the temperature decrease from LW cooling. The LW cooling within the inversion does therefore not primarily result in buoyancy driven turbulence generation.

The cloud that extends into the inversion was found to exhibit little to no vertical velocity variance *w'w'*, with non zero *w'w'* values beginning at the base of the temperature inversion and increasing down into the cloud layer. The impact upon vertical velocity and turbulence of the extension into the inversion is a novel finding confirming the hypothesis laid out at the start of this chapter. Greater LW cooling within the inversion results in less LW cooling under the inversion as the LW black-body limit (integrated down from cloud top) is reached further up within the cloud layer. Cooling that does occur under the inversion is shifted upwards in the profile towards the temperature inversion base. Consequently the peak in *w'w'* is higher up within the profile the greater the liquid cloud extension into the inversion. A peak *w'w'* higher up in the profile will result in the same strength *w'w'* reaching relatively less far down the boundary layer than a profile with a peak *w'w'* lower down into the boundary layer.

Turbulence generation within the inversion was not notable despite LW cooling within the layer taking place, LW cooling being the main driver of cloud driven turbulence. Examination of the variation in potential temperature tendency due to changes in the microphysics indicated that condensation was being driven by the LW cooling to the expense of temperature change within the temperature inversion, resulting in lower levels of buoyancy driven turbulence within the inversion than expected

The variations in cloud top extension into the temperature inversion impacts the cloud ice water content. Cloud ice forms from the layer of super-cooled water at cloud top. Increases in liquid water within the inversion occurs as more droplets form as LW cooling increases condensation within the humidity inversion above the base of the temperature inversion. An increase in the amount of water at cloud top results in greater ice production. The increased cooling near cloud top and greater liquid water content contributes to increased ice water content throughout the profile.

In the Ice runs, where the IN was set to 7 times the levels of the Norm case IN, the increased extension of cloud top into the inversion increased the peak LW cooling. The Ice runs have a liquid water content within the grey-body LWP range (sub 50 g m^{-2}) and so their radiative properties are particularly sensitive to shifts in liquid water content. The increased extension of liquid cloud above the temperature inversion increases the liquid water content aloft as more condensation occurs. As a result of the increased liquid water concentrations aloft the LW cooling peak shifts up into the inversion and increases in magnitude. The cloud driven turbulence of the Ice runs still decreases with increased extension of cloud top into the inversion despite the raise in LW cooling magnitude. The LW cooling percentage under the temperature inversion, that primarily drives temperature change and buoyancy-driven turbulent motions, decreases as the LW cooling shifts further up into the inversion. The LW cooling peak within the inversion drives increased condensation rather than turbulence so even thought the profile peak LW cooling is stringer the peak *w'w'* will be weaker with increasing cloud extension into the inversion. It is therefore the case that two cloud profiles may have the same peak levels of LW cooling but one may have weaker cloud driven motions due to the location within the cloud of the peak in the cooling profile due to variations in the extension of the cloud liquid water profile into the inversion.

6 Conclusions

This project has improved our understanding of the dynamical behaviour of Arctic Stratocumulus by using observational data from the Arctic Summer Cloud Ocean Study (ASCOS) campaign and idealised simulations carried out using the UK Meteorological Office Large Eddy Model (LEM).

6.1 Observational findings

Observational data collected during ASOCS was analysed to give an overview of the dominant controls over the depth that cloud driven turbulence could reach down into the boundary layer from cloud top. This provides an idea of the strength of any generated turbulence and the coupling state - whether or not the surface and cloud layers are turbulently linked -of the boundary layer profile.

The depth of the cloud mixed layer extension down from cloud top into the boundary layer was calculated from the dissipation rate profiles derived from the MMCR retrievals. A turbulent threshold of 5×10^{-5} m^2 s^{-3}, the dissipation rate coincident with cloud top where cloud driven turbulence ceases, was applied, with dissipation rates lower than the threshold value classed as non-turbulent. The cloud mixed layer depth was calculated as the point at which the dissipation rate first dropped under the turbulent threshold beneath cloud top.

The dissipation rate decoupling criteria of 5×10^{-5} m^2 s^{-3} agreed well with the timing of decoupling and the percentage occurrence of decoupling from the alternative measures of decoupling in terms of the lifting condensation level. The week during ASCOS from the 25th August to the 1st of September 2008 was deemed to be decoupled 68.8% of the time according the dissipation rate, agreeing with the percentage of decoupling from Shupe et al., (2013) and Sotiropoulou et al., (2014).

Frequency density plots of the specific humidity profiles showed that when decoupled the humidity peaks near to the surface beneath the base of the cloud mixed layer, with humidity decreasing within the cloud mixed layer.

Decoupled conditions restrict transport of water vapour from the surface to the cloud layer.

The depth of the cloud mixed layer was examined in relation to the cloud geometry, ice water path and liquid water path (LWP). The cloud mixed layer depth was found to be most sensitive to the changes in LWP at LWP values lower than 40 g m^{-2}. A change in the LWP under 40 g m^{-2} elicited a substantial change in the cloud mixed layer depth from 180-400 m. At LWP values over 40 g m^{-2} the MLD varies between 400-1200 m but the LWP value is unrelated.

Liquid water is the dominant control over cloud radiative flux. The down welling LW flux at the surface rises from ~238 W m^{-2} to 295 Wm^{-2} at LWPs of 0-40 g m^{-2}, stabilising at ~300 W m^{-2} LWP values above 40 g m^{-2}. Normalisation of the down welling LW flux with the LW flux emitted by the cloud base showed that the clouds with a LWP under 40 g m^{-2} were radiating as a grey-body. Clouds radiating as a grey-body have radiative fluxes that are sensitive to changes in LWP, where as clouds radiating as a black-body do not.

The change in the radiative state of the cloud between the grey and black states is a significant one in terms of accurately predicting and diagnosing changes in surface energy budgets. Clouds, when radiating as grey bodies are sensitive to small changes in LWP that would not impact the radiation emitted by a cloud with a higher LWP. The inaccurate diagnosis of the low LWP clouds, even by a few g m^{-2}, will alter the surface energy budget a disproportionately large value compared to the same LWP change to cloud with LWP in the black-body range.

The change in cloud mixed layer depth in the observations was hypothesised to be due to variations in the LW cooling occurring at cloud top. The profiles of the radiative fluxes were not available in the observational data and so they were modelled using the Edwards-Slingo radiation code. The relationship of the profile peak in LW flux from the Edwards-Slingo radiation code with LWP matches the trend seen in the surface LW flux with the LWP. The peak LW cooling rate increases with rising LWP up to a LWP of 40 g m^{-2}, above which changes in LW cooling are unrelated to the LWP. The cloud mixed layer depth increases with increasing LW cooling at all levels of LW cooling but the scatter

in the relationship increases at LW cooling values where the cloud's LWP is above the black-body threshold.

6.1.1 Richardson number

The profiles of the gradient Richardson number during ASCOS were calculated by Dr Guylaine Canut and provided an alternative view of the turbulent structure of the boundary layer. The gradient Richardson number breaks down the boundary layer into turbulent and non-turbulent layers. The peak in LW cooling and the peak in the temperature gradient is located roughly a third of the way down into the cloud layer. The layer containing the LW cooling and the top of the cloud layer has a gradient Richardson number indicating it is non-turbulent with the turbulent Richardson number classifications beginning just under the peak in LW cooling and the peak in the temperature gradient and continuing down the profile until a point that is predominantly consistent with the depth of the dissipation rate turbulent threshold.

The conclusion from the Richardson number profiles is that the cooling that occurs within the top third of the cloud layer above the temperature inversion does not produce turbulence.

6.2 LEM findings

Observational data is complicated to unravel due to the number of possible co-variables that occur in real world data. In order to unpick finer trends and causes in variation in the cloud mixed layer depth and the behaviour of cloud driven turbulence a series of idealised Large Eddy Model (LEM) simulations with a range of different LWPs were carried out.

The LEM was run in 2D with the Morrison's Microphysics scheme. The base case simulation was initialised using the radiosonde profiles from 11am on the 28th of August 2008. A range of simulations with ice nuclei concentrations from 0.1 times the base case IN level (base IN, 1.7 L^{-1}) to 9 times the base level IN were run achieving a LWP range of 224 g kg^{-2} to 6 g kg^{-2}.

The cloud mixed layer depth and strength of the turbulence generated in the LEM simulations matched the trend seen in the observational data, with the

cloud mixed layer depth varying with LWP up until the point the cloud radiates as a black body. In the case of the LEM simulations the LWP pivot point between grey- and black-body was around 50 g m^{-2}.

The consistency between the observational finding and the LEM IN modification simulations is indicative that any finer trends observed in the LEM simulations regarding the behaviour of the cloud mixed layer depth is likely to be valid for the real world. Finer controls on the levels of peal LW cooling in cloud, other than the LWP, were identified as: Changes to the humidity profile aloft and the subsequent change to the net LW cooling at cloud top as the LW warming from above changes, the sharpness of the LW cooling peaks and the extension of liquid cloud and LW cooling above the base of the temperature inversion.

A range of simulations were carried out to investigate the impact of the extension of cloud top above the base of the temperature inversion. In the simulations carried out the controlling factor on the depth of the extension of cloud top above the base of the temperature inversion was the depth that the increase in humidity inversion stayed at the peak value of 3.5 g kg^{-1} aloft. The extension of the cloud top into the temperature inversion ranged from 25.1 m to 59.1 m in the LEM simulations with the top of the humidity inversion ranging from 895 mb to 835 mb.

The presence of the humidity inversion above cloud top results in super-saturation within the temperature inversion, extending cloud top aloft. The cloud is sustained within the inversion because the LW cooling that occurs above the temperature inversion base primarily drives condensation. Less of the LW cooling that occurs within the inversion results in buoyancy driven motions than if the same level of LW cooling were to occur under or at the base of the temperature inversion. The greater the extension of cloud above the base of the temperature inversion the more LW cooling within the inversion and consequently the less cooling at and under the temperature inversion base. In cloud turbulence can therefore be weaker in one cloud than another with the same peak LW cooling value if the LW cooling peak for one cloud occurs above the base of the temperature inversion and the other under.

6.3 Cloud mixed layer depth parameterisation

The observational data in Chapter 2 allows the derivation of a basic parameterisation for the depth of the cloud mixed layer based upon the liquid water path, Figure 2.27. The parameterisation of MLD is divided based upon whether or not the cloud layer is radiating as a black- or grey-body. Where the cloud layer is radiating as a grey body the MLD_{GB} is calculated as:

$$MLD = \frac{(LWP_{GB} + 1.362)}{0.0485},$$

Equation 6.12

where LWP_{GB} is the cloud layers LWP when the cloud is radiating as a grey-body. If the cloud layer is radiating as a black-body the LWP_{GB} is capped at the largest LWP where the cloud still radiates as a grey-body. Once radiating as a blackbody variations in LWP no longer impact the parameterised MLD. In the ASCOS case the maximum LWP_{GB} = 40 g m^{-2}, as a result for LWP values at or above the maximum LWP value the MLD_{BB} is equal to 852.82 m (2dp).

The calculated MLD is the depth beneath cloud top that the MLD has the potential to reach down into the boundary layer. To be of most use as a parameterisation that could describe when the boundary layer is coupled the height above the surface that the lowest level the MLD reaches, Z_{MLD}:

$$Z_{MLD} = Z_{ctop} - MLD,$$

Equation 6.13

the cloud mixed layer depth cannot be greater than the height of the cloud above the surface so:

$$if\ Z_{MLD} < 0\ then\ Z_{MLD} = 0,$$

Equation 6.14

where Z_{ctop} is the height of cloud top. A coupled boundary layer is indicated by a Z_{MLD} of 0 m and/or if the height of the surface mixed layer (SML) is equal to or higher than the Z_{MLD}.

$$Coupled = Z_{MLD} \leq Z_{SML},$$

Equation 6.15

or

$$Coupled = Z_{MLD} = 0,$$

Equation 6.16

The calculation of the depth of the SML in the Arctic is beyond the scope of this thesis and we suggest further research is required to find an appropriate low computational cost parameterisation following on from the work carried out by Brooks et al. (2017).

The parameterisation for MLD is functional but has limitations. The function as it stands only alters the clouds MLD when the cloud is deemed to be radiating as a grey-body and so once at the critical LWP the MLD is static. A static MLD at black-body LWP values is not realistic as other factors such as advection, large scale motions and subtle factors such as the extension of cloud top into the temperature inversion are capable of modifying the MLD. The impacts of other factors than LWP upon the MLD are beyond the scope of this thesis and so are not currently taken into account.

The parameterisation described here is derived from only one week of data from one location. The parameterisation would benefit from testing against other observational data sets and the inclusion of data gathered from different seasons and locations. We currently have no way of knowing how applicable the MLD parameterisation would be for single layer stratocumulus nearer to the coast of during the dark winter months.

Additional modelling using LEM simulations in 3D under diverse conditions, e.g. winter stratocumulus cloud may provide some clarification as to the similarity of the MLD behaviour under more variable conditions but theses simulations would also need to be viewed alongside observational data in order to ensure that the modelled clouds showed appropriate behaviour. Specifically 3D runs will be required for testing the exact depth the MLD reaches rather than 2D as though the behaviour is comparable between 2D and 3D runs the strength of turbulence, and hence the exact depth of the MLD, is altered between 2D and 3D. Further modelling in 3D will also enable the parameterisation to be enhanced by adding the degree of transport up into the MLD from the surface. A current suggestion is to restrict the mixing of surface layer emissions e.g. aerosol and water vapour above the MLD base,

but this is not a realistic scenario as a small amount of mixing will occur even during decoupling. Further modelling and examination of observations will be required to find an appropriate fraction of transport during decoupling. We suggest a combination of transport modelling and if possible, aerosol profiles taken during decoupled conditions to examine the concentrations above and under the cloud MLD.

6.3.1 Relevance to Climate and Forecast models

Operational forecast models and climate models do not have fine enough grid scales to directly resolve the turbulence within the cloud and boundary layer or the extension of cloud top into the temperature inversion. Modelling results here have indicated that even a modest extension of the cloud top into the temperature inversion alters the LW cooling profile of the cloud layer and the amount of buoyancy driven turbulence able to be generated. Extension into the inversion has also been shown to modify the amount of liquid water and ice produced by the cloud layer, as LW cooling in the temperature inversion results in more condensation than temperature change. Given the impact of extension of cloud layer into the inversion and the inability of forecast and climate models to simulate the extension directly further work is required to parameterise its impact upon the cloud LW cooling profiles and subsequent alterations to the liquid and ice water profiles and turbulent structure. Climate and forecast models frequently model the boundary layer as too well mixed e.g. Birch et al., (2009). The impact of coupling being too frequent is too great a level of transport from the surface up to the cloud layer, giving rise to too great a level of aerosol and water vapour at cloud level. The parameterisation of MLD derived in this thesis aims to help correct the error of over predicting the boundary layer as too well mixed by indicating when the cloud and surface are not likely to be coupled. The MLD parameterisation outlined in this thesis uses only LWP to give an idea of if the cloud and surface are turbulently coupled. The LWP is a standard model variable and the parameterisation is simple so will be of low computational cost, a benefit for addition to models. With a diagnosis of coupled or decoupled the transport from the surface can be modified, crudely in this first version of the parameterisation but this can be enhanced in the future. The more accurate the representation of the aerosol and water vapour the more accurate the simulated cloud microphysical

properties e.g. LWP and the more reliable the model surface heating rates become, a key output in particular for climate simulations aiming to predict the future speed and magnitude of climate change. Accurate climate model being necessary in order for policy makers to make decisions with confidence.

6.4 Recommendations and further work

The in-cloud driven turbulence has been shown to be sensitive to variations in the LWP at LWP levels where the cloud would be radiating a grey-body and the extension of cloud top above the base of the temperature inversion and into the humidity inversion. It is recommended that the findings from this thesis are built upon and parameterisations are designed to describe the cloud dynamical response appropriately for inclusion into non-cloud resolving forecast models and climate simulations.

In order for these parameterisations to be designed a wider range of LEM simulations in both 2D and 3D need to be carried out. The simulations should expand upon the parameter space explored here and the 3D simulations chosen carefully to verify and correctly scale any parameterisations.

Any parameterisations of the depth of cloud driven turbulence, the height cloud top extends into the inversion and the consequent changes to the boundary layer turbulent and microphysical structure will require validation by testing on observational data.

The ASCOS data is from one week in one year at one location and so does not have a wide enough spread of observations to allow any fine trends to be unpick from the scatter. The variation in cloud dynamics with variation of the extension of cloud top above the base of the temperature inversion exists alongside a range of variations in the cloud microphysical properties and so a large data set will be required for observational trends to become apparent in the statistics.

In order to confirm that the behaviour observed in the LEM simulation is real and to test any parameterisations a wider range of observations of the Arctic stratocumulus topped boundary layer is required. The observational data set required will need to have similar retrievals to the ASCOS campaign in terms

of full boundary layer profiles of turbulent and microphysical structure should be analysed if available. Ideally a series of locations around the Arctic from the full annual cycle. If such a data set is not available it is recommended that such a campaign is carried out.

As points of interest it would be beneficial to carry out a series of small scale LEM experiments looking at:

- How the small diurnal cycle impact cloud driven turbulence and the behaviour of the cloud layer with variable extension of cloud into the inversion.
- If a decoupled cloud layer recouples how does it respond and the converse. Do cloud layers maintain the switch between coupled and decoupled? Is it a sharp transition, is it more of a gradual shift or does the cloud layer then oscillate between coupled and decoupled and what impact does this have upon the cloud properties and lifetime?

6.4.1 Adding a tracer

Aerosol emitted from the surface in the central Arctic is theorised to be an important source of CCN and IN, especially during the aerosol limited summer months. Surface emitted aerosol are only able to act as CCN and IN if they are able to reach the height of the cloud layer. Model studies, such as that by Browse et al. (2012), have assessed the impact of an increase in the surface emissions of water vapour and aerosol based on the projected decreased sea ice cover upon the occurrence and properties of cloud and their subsequent alteration to the surface energy budget. These model studies used current parameterisations that produce boundary layers that are too frequently turbulently coupled and as such the transport of the surface emissions to the cloud layer may be incorrectly estimated. Errors in the estimation of transport from the surface will impact the cloud properties and subsequent cloud occurrence and life time and impact upon the surface energy budget. A key area of work this thesis has identified a need for is LEM simulations of coupled and decoupled boundary layers with the addition of a tracer to simulate the transport of surface emitted quantities such as water vapour and aerosol to the cloud layer.

The addition of a tracer to the surface layer in the LEM simulation of decoupled a and coupled boundary layers will enable simulations of the transport from surface to cloud. The aim is to answer the question of how 'decoupled' decoupled clouds are from the surface. The simulations of surface tracers should cover a range of different mixed layer depths as well as coupled conditions and variations on the strength of the formed temperature inversion at the mixed layer depth base. The tracer work would be ideally placed to compliment further model work on parameterising the MLD and boundary layer coupling state by also parameterising the alteration, if any, decoupling has upon transport of surface emitted quantities throughout the boundary layer.

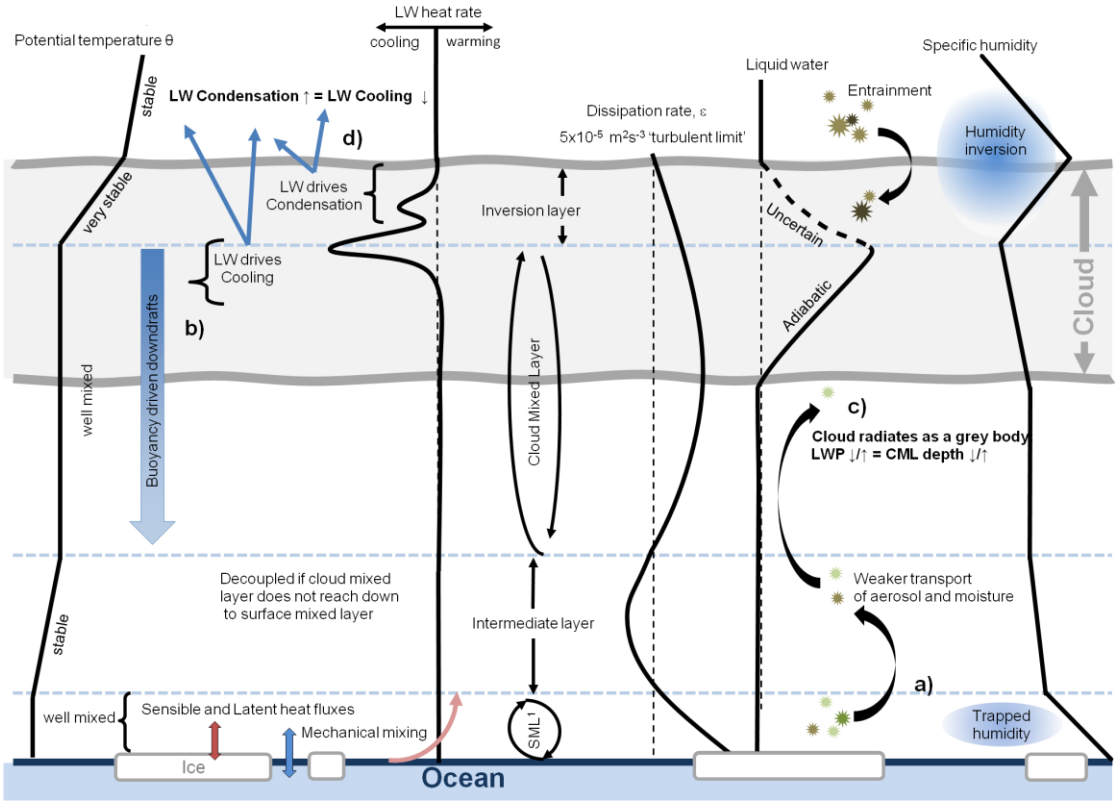

Figure 6.75 - Schematic of a decoupled Arctic mixed phase stratocumulus topped by a humidity inversion with cloud top extending up into the temperature inversion summarising the main findings from this thesis. The schematic illustrates the idealised profiles of potential humidity, LW radiative heating, dissipation rate, liquid water and specific humidity (left to right). The main features of each layer as identified by this thesis are highlighted, namely the difference in the result of LW cooling within the inversion (condensation) and beneath (cooling) and the importance of buoyancy driven mixing in determining the depth the cloud mixed layer reaches down into the boundary layer.[1] SML is the surface mixed layer.

It would also be of use to carry out simulations with a tracer added above cloud to assess the transport into the cloud layer from aloft. The entrainment from aloft being theorised to be of importance as aerosol from lower latitudes is transported into the Arctic at higher levels. Simulations with a tracer at the surface and above the cloud will enable investigation into how efficient is transport from aloft compared to that from the surface.

Specific questions to examine are:

- Is transport from the surface to the cloud layer altered by the coupling state of the boundary layer? If so to what extent is transport altered? Can the fraction of transport be parameterised?
- How does efficiency of transport from the surface to cloud vary from that of the transport from aloft? Does this alter with coupling state?

6.5 Overall summary

The surface mixed layer is shallow and primarily determined by mechanical mixing (Brooks et al., (2017)) as the surface fluxes are typically weak in the Arctic. When the cloud and surface layers are decoupled humidity is essentially trapped in the surface layer as mixing upwards is restricted. The hypothesis based upon the trapping of humidity in the surface layer is that the upward transport of aerosol is also restricted during decoupling. Restricted aerosol transport from the surface would limit the available CCN and IN in the cloud layer potentially altering the clouds characteristics with the subsequent impact upon radiative budgets and surface heating. Given the shallow nature of the surface mixed layer whether or not surface and cloud turbulent coupling occurs is determined by whether or not the turbulent cloud mixed layer reaches far enough down into the boundary layer to meet the surface mixed layer (Figure 6.75a).

The primary control over the cloud mixed layer depth buoyancy driven motions caused by LW cooling driven temperature change (Figure 6.75b). Analysis of the observational data from ASCOS revealed that the depth of the cloud mixed layer varies with LWP changes when the LWP is low enough that the cloud layer radiates as a grey-body. At LWP's where the cloud radiates as a grey-body changes in the LWP result in changes to the LW flux, and the resultant LW cooling amounts, altering the strength of any buoyancy driven motions, a key novel finding (Figure 6.75c). A basic parameterisation for the MLD, based upon the LWP, is outlined in section 6.3. The parameterisation outlined in this thesis is basic and does not take into account factors other than LWP that may alter the MLD. A key finding from this thesis not yet incorporated into a workable parameterisation is the impact the extension of

cloud top into the inversion has upon the MLD via modification of the amount of buoyancy driven turbulence.

The LW cooling that occurs at or under the base of the temperature inversion is the primary source of buoyancy driven turbulence. If cloud extends up into the temperature inversion rather than drive cooling the emission of LW radiation drives primarily drives condensation. In preferentially driving condensation within the temperature inversion, rather than cooling, the generation of buoyant motions is suppressed relative to the amount that would be expected of the same LW flux at or under the temperature inversion base. Within the temperature inversion the steep temperature gradient renders the layer very stable in terms of turbulence generation as any radiative cooling that is generated has to drop the temperature by a greater amount than cooling under the inversion for buoyancy driven motions to be generated. This thesis is the first to investigate the impact of the extension of cloud top into the temperature inversion on turbulence generation and cloud dynamics. One of the key takeaway points from this research is that the LW flux within the cloud layer has reduced impact upon driving cloud motions but increases the liquid water (Figure 6.75d).

List of References

ACIA, (2004). Impacts of a Warming Arctic: Arctic Climate Impact Assessment. ACIA Overview report. *Cambridge University Press*. 140 pp.

Albrecht, B. A. (1989), Aerosols, cloud microphysics, and fractional cloudiness, *Science*, *245*, 1227-1017.

Andreas, E. L., Jordan, R. R., & Makshatas, A. P. (2005). Parameterizing turbulent exchange over sea ice: The Ice Station Weddel results. Boundary-Layer Meteorology, 114, 439–460. https://doi.org/10.1007/s10546-004-1414-7

Bennartz, R., Shupe, M.D., Turner, D.D., Walden, V.P., Steffen, K., Cox, C.J., Kulie, M.S., Miller, N.B. and Pettersen, C., (2013). July 2012 Greenland melt extent enhanced by low-level liquid clouds. *Nature*, *496*(7443), p.83.

Bintanja, R., Graversen, R.G. and Hazeleger, W., (2011). Arctic winter warming amplified by the thermal inversion and consequent low infrared cooling to space. *Nature Geoscience*, *4*(11), p.758.

Birch, C. E., Brooks, I. M., Tjernström, M., Milton, S. F., Earnshaw, P., Söderberg, S., & Persson, P. O. G. (2009). The performance of a global and mesoscale model over the central Arctic Ocean during late summer. *Journal of Geophysical Research: Atmospheres*, *114*(D13).

Birch, C. E., Brooks, I. M., Tjernström, M., Shupe, M. D., Mauritsen, T., Sedlar, J., Lock, A. P., Earnshaw, P., Persson, P. O. G., Milton, S. F., and Leck, C. (2012) Modelling atmospheric structure, cloud and their response to CCN in the central Arctic: ASCOS case studies, *Atmos. Chem. Phys*., *12*, 3419-3435

Boé, J., A. Hall, and X. Qu (2009) September sea-ice cover in the Arctic Ocean projected to vanish by 2100, *Nat. Geosci., 2*, 341–343

Bretherton, C. S., & Wyant, M. C. (1997). Moisture transport, lower-tropospheric stability, and decoupling of cloud-topped boundary layers. *Journal of the atmospheric sciences*, 54(1), 148-167.

Brost, R., J. Wyngaard, and D. Lenschow, (1982) Marine stratocumulus layers. Part II: Turbulence budgets. *J. Atmos. Sci*., 39, 818-836.

Browse, J., Carslaw, K. S., Arnold, S. R., Pringle, K., and Boucher, O. (2012) The scavenging processes controlling the seasonal cycle in Arctic sulphate and black carbon aerosol, Atmos. Chem. Phys., 12, 6775-6798.

Corbett, J.J., Lack, D.A., Winebrake, J.J., Harder, S., Silberman, J.A. and Gold, M., 2010. Arctic shipping emissions inventories and future scenarios. *Atmospheric Chemistry and Physics*, *10*(19), pp.9689-9704.

Crawford, I., Bower, K. N., Choularton, T. W., Dearden, C., Crosier,J., Westbrook, C., Capes, G., Coe, H., Connolly, P. J., Dorsey,J. R., Gallagher, M. W., Williams, P., Trembath, J., Cui, Z., andBlyth, A.: Ice formation and development in aged, wintertime cu-mulus over the UK: observations and modelling, Atmos. Chem.Phys., 12, 4963–4985,doi:10.5194/acp-12-4963-2012, 2012.

Curry, J. A., W. B. Rossow, D. Randall, and J. L. Schramm, (1996) Overview of Arctic cloud and radiation characteristics. *J. Climate, 9*, 1731-1764.

Curry, J.A., Hobbs, P.V., King, M.D., Randall, D.A. & Minnis, P. (2000). FIRE Arctic clouds experiment. Bulletin of the American Meteorological Society, 81, 5{29. 16, 18, 21

Deardorff, J. W. (1981). On the distribution of mean radiative cooling at the top of a stratocumulus-capped mixed layer. *Quarterly Journal of the Royal Meteorological Society*, 107(451), 191-202.

Deardorff, J. W., (1980), Cloud Top Entrainment Instability. *J. Atmos. Sci.*, 37, 131-147.

DeMott, P., Prenni, A., Liu, X., Kreidenweis, S., Petters, M., Twohy, C.,Richardson, M., Eidhammer, T. & Rogers, D. (2010). Predicting global atmospheric ice nuclei distributions and their impacts on climate. Proceedings of the National Academy of Sciences of the United States of America, 107, 11217{11222. 23

Derocher, A. E., (2010) The prospects for polar bears, *Nature,* 468, 905-906.

Dong, X., Schwantes, A.C., Xi, B. and Wu, P., 2015. Investigation of the marine boundary layer cloud and CCN properties under coupled and decoupled conditions over the Azores. *Journal of Geophysical Research: Atmospheres*, *120*(12), pp.6179-6191.

Driedonks, A.G.M. & Tennekes, H. (1984). Entrainment effects in the well-mixed atmospheric boundary-layer. Boundary-Layer Meteorology, 30, 75{105. 10, 11, 102,111

Durran, D. R., & Klemp, J. B. (1982). On the effects of moisture on the Brunt-Väisälä frequency. Journal of the Atmospheric Sciences, 39,2152–2158. https://doi.org/10.1175/1520-0469(1982)039<2152:OTEOMO>2.0.CO;2

Edwards, J.M. and Slingo, A., (1996). Studies with a flexible new radiation code. I: Choosing a configuration for a large-scale model. *Quarterly Journal of the Royal Meteorological Society*, *122*(531), pp.689-719.

Francis, J. A., & Vavrus, S. J. (2012). Evidence linking Arctic amplification to extreme weather in mid-latitudes. *Geophysical Research Letters*, *39*(6).

Francis, J.A. and Hunter, E., (2006). New insight into the disappearing Arctic sea ice. *Eos, Transactions American Geophysical Union*, *87*(46), pp.509-511.

Garratt, J. (1992). The Atmospheric Boundary Layer. Cambridge University Press, UK. 34

Garrett, Timothy J., Lawrence F. Radke, Peter V. Hobbs, (2002) Aerosol Effects on Cloud Emissivity and Surface Longwave Heating in the Arctic. J. Atmos. Sci., 59, 769-778.

Graversen, R.G. and Wang, M., 2009. Polar amplification in a coupled climate model with locked albedo. *Climate Dynamics*, *33*(5), pp.629-643.

Gray, M. E. B., Petch, J., Derbyshire, S. H., Brown, A. R., Lock, A. P., Swann, H. A., & Brown, P. R. A. (2001). Version 2.3 of the Met. Office large eddy model. Met Office (APR) Turbulence and Diffusion Rep, 276.

Grosvenor, D.P.; Choularton, T.W.; Lachlan-Cope, T.; Gallagher, M.W.; Crosier, J.; Bower, K.N.; Ladkin, R.S.; Dorsey, J.R.. 2012 In-situ aircraft observations of ice concentrations within clouds over the Antarctic Peninsula and Larsen Ice Shelf. *Atmospheric Chemistry and Physics*, 12 (23). 11275-11294. https://doi.org/10.5194/acp-12-11275-2012

Hahn, C. J., and S. G. Warren, (2007) A gridded climatology of clouds over land (1971–96) and ocean (1954–97) from surface observations worldwide. Numeric Data Package NDP-026E ORNL/CDIAC-153, CDIAC, Department of Energy, Oak Ridge, TN.

Harrington, J.Y., Reisin, T., Cotton, W.R. and Kreidenweis, S.M., 1999. Cloud resolving simulations of Arctic stratus: Part II: Transition-season clouds. *Atmospheric Research*, *51*(1), pp.45-75.

Hermann, G., and R. Goody, (1976): Formation and persistence of summertime arctic stratus clouds. J. Atmos. Sci., 33, 1537–1553.

Hill, A. A., Field, P. R., Furtado, K., Korolev, A., & Shipway, B. J. (2014). Mixed-phase clouds in a turbulent environment. Part 1: Large-eddy simulation experiments. *Quarterly Journal of the Royal Meteorological Society*, *140*(680), 855-869.

Hines, K. M., & Bromwich, D. H. (2017). Simulation of late summer Arctic clouds during ASCOS with Polar WRF. *Monthly Weather Review*, *145*(2), 521-541.

Holland, Marika M., and Cecilia M. Bitz. (2003) Polar amplification of climate change in coupled models. *Climate Dynamics,* 21.3-4: 221-232.

Ingram, W. J., Woodward, S., & Edwards, J. M. (1997), Radiation. UM Documentation Paper No 23. UK Met Office, Exeter, UK.

Intrieri, J. M., C. W. Fairall, M. D. Shupe, P. O. G. Persson, E. L. Andreas, P. Guest, and R.M. Moritz (2002), An annual cycle of Arctic surface cloud forcing at SHEBA, *J. Geophys. Res., 107(C10)*, 8039

Intrieri, J. M., C. W. Fairall, M. D. Shupe, P. O. G. Persson, E. L. Andreas, P. Guest, and R.M. Moritz (2002), An annual cycle of Arctic surface cloud forcing at SHEBA, *J. Geophys. Res., 107(C10)*, 8039

Intrieri, J. M., C. W. Fairall, M. D. Shupe, P. O. G. Persson, E. L. Andreas, P. Guest, and R.M. Moritz (2002), An annual cycle of Arctic surface cloud forcing at SHEBA, *J. Geophys. Res., 107(C10)*, 8039

IPCC, (2013), Climate Change 2013: The Physical Science Basis. Contribution of Working Group I to the Fifth Assessment Report of the Intergovernmental Panel on Climate Change [Stocker, T.F., D. Qin, G.-K. Plattner, M. Tignor, S.K. Allen, J. Boschung, A. Nauels, Y. Xia, V. Bex and P.M. Midgley (eds.)]. *Cambridge University Press*, Cambridge, United Kingdom and New York, NY, USA, 1535 pp, doi:10.1017/CBO9781107415324.

Iverson SA, Gilchrist HG,Smith PA, Gaston AJ, Forbes MR. (2014) Longer ice-free seasons increase the risk of nest depredation by polar bears for colonial breeding birds in the Canadian Arctic. Proc. R. Soc. B 281: 20133128.

Jahn, A., J. E. Kay, M. M. Holland, and D. M. Hall (2016), How predictable is the timing of a summer ice-free Arctic?, *Geophys. Res. Lett.*, *43*, 9113–9120, doi:10.1002/2016GL070067.

Jiang, H., G. Feingold, W. R. Cotton, and P. G. Duynkerke (2001), Large-eddy simulations of entrainment of cloud condensation nuclei into the Arctic boundary layer: May 18, 1998, FIRE/SHEBA case study, *J. Geophys. Res*., 106(D14), 15113-15122

Johnson, B. T., Shine, K. P., & Forster, P. M. (2004). The semi-direct aerosol effect: Impact of absorbing aerosols on marine stratocumulus. *Quarterly Journal of the Royal Meteorological Society*, *130*(599), 1407-1422.

Jones, C. R., Bretherton, C. S., & Leon, D. (2011). Coupled vs. decoupled boundary layers in VOCALS-REx. *Atmospheric Chemistry and Physics*, 11(14), 7143-7153.

King, J.C., Gadian, A., Kirchgaessner, A., Kuipers Munneke, P., Lachlan-Cope, T.A., Orr, A., Reijmer, C., van den Broeke, M.R., Van Wessem, J.M. and Weeks, M., (2015). Validation of the summertime surface energy budget of Larsen C Ice Shelf (Antarctica) as represented in three high-resolution atmospheric models. *Journal of Geophysical Research: Atmospheres*, *120*(4), pp.1335

Laxon S. W., K. A. Giles, A. L. Ridout, D. J. Wingham, R. Willatt, R. Cullen, R. Kwok, A. Schweiger, J. Zhang, C. Haas, S. Hendricks, R. Krishfield, N. Kurtz, S. Farrell and M. Davidson (2013), CryoSat-2 estimates of Arctic sea ice thickness and volume, *Geophys Res Lett., 40*

Leck, C., and C. Persson (1996), Seasonal and short-term variability in dimethyl sulfide, sulfur dioxide and biogenic sulphur and sea salt aerosol particles in the arctic marine boundary layer, during summer and autumn, *Tellus 48B*, 272-299.

Lilly, D. K. (1968). Models of cloud-topped mixed layers under a strong inversion. *Quarterly Journal of the Royal Meteorological Society*, 94(401), 292-309.

Lohmann, U., (2002) A glaciation indirect aerosol effect caused by soot aerosols, *Geophys. Res. Lett*., 29(4), doi:10.1029/2001GL014357.

Lothon, M., Lenschow, D. H., Leon, D., and Vali, G., Turbulence measurements in marine stratocumulus with airborne Doppler radar, Q. J. Roy. Meter. Soc., 131, 2063–2080, 2005.

Lu, D., Park, G.K., Choi, K. and Oh, S., 2014. An economic analysis of container shipping through Canadian Northwest Passage. *International Journal of e-Navigation and Maritime Economy*, *1*, pp.60-72.

Marsham, J. H., & Dobbie, S. (2005). The effects of wind shear on cirrus: A large-eddy model and radar case-study. Quarterly Journal of the Royal Meteorological Society: A journal of the atmospheric sciences, applied meteorology and physical oceanography, 131(611), 2937-2955.

Marsham, J. H., Dobbie, S., & Hogan, R. J. (2006). Evaluation of a large-eddy model simulation of a mixed-phase altocumulus cloud using microwave radiometer, lidar and Doppler radar data. *Quarterly Journal of the Royal Meteorological Society: A journal of the atmospheric sciences, applied meteorology and physical oceanography*, *132*(618), 1693-1715.

Mauritsen, T., Sedlar, J., Tjernström, M., Leck, C., Martin, M., Shupe, M., Sjogren, S., Sierau, B., Persson, P. O. G., Brooks, I. M., and Swietlicki, E. (2011) An Arctic CCN-limited cloud-aerosol regime, *Atmos. Chem. Phys*., 11, 165-173, doi:10.5194/acp-11-165-2011.

Meillier, Y. (2004), Periodic modulation of fine-scale turbulence by gravity waves above the nocturnal boundary layer: Experimental validation using in situ measurements, PhD Thesis, 145 pp, Univ. of Colorado, Boulder, Colorado.

Meillier, Y. (2008). Modulation of small-scale turbulence by gravity waves in the nocturnal boundary layer. Journal of the Atmospheric Sciences, 65, 1414–1427. https://doi.org/10.1175/2007JAS2359.1

Moeng, C.H., Cotton, W.R., Bretherton, C., Chlond, A., Khairoutdi-nov, M., Krueger, S., Lewellen, W.S., MacVean, M.K., Pasquier, J.R.M.,Rand, H.A., Siebesma, A.P., Stevens, B. & Sykes, R.I. (1996). Simulation of a stratocumulus-topped planetary boundary layer: Intercomparison among different numerical codes. Bulletin of the American Meteorological Society, 77, 261{278. 130,134

Morrison, H., Curry, J.A. & Khvorostyanov, V.I. (2005). A new double-moment microphysics parameterization for application in cloud and climate models. Part i:Description. Journal of the Atmospheric Sciences, 62, 1665{1677. 39, 40, 45, 47, 48,54, 80, 91

Morrison, H., de Boer, G., Feingold, G., Harrington, J., Shupe, M. D., & Sulia, K. (2012). Resilience of persistent Arctic mixed-phase clouds. Nature Geoscience, 5(1), 11-17.

Morrison, H., Pinto, J. O., Curry, J. A., & McFarquhar, G. M. (2008). Sensitivity of modelled arctic mixed-phase stratocumulus to cloud condensation and ice nuclei over regionally varying surface conditions. *Journal of Geophysical Research*, 113(D5), D05203.

Nicholls, S. & Leighton, J. (1986). An observational study of the structure of stratiform cloud sheets: Part i. structure. Quarterly Journal of the Royal Meteorological Society, 112, 431{460. 102

Nicholls, S. (1984). The dynamics of stratocumulus: Aircraft observations and comparisons with a mixed layer model. *Quarterly Journal of the Royal Meteorological Society*, 110(466), 783-820.

Nilsson, E. D., Ü. Rannik, E. Swietlicki, C. Leck, P. P. Aalto, J. Zhou, and M. Norman (2001), Turbulent aerosol fluxes over the Arctic Ocean: 2. Wind-driven sources from the sea, J. Geophys. Res., 106(D23), 32139?32154

NSIDC, (2018), *Arctic Map* [ONLINE]. Available at: https://nsidc.org/sites/nsidc.org/files/images//arctic_map_small.gif [Accessed 7 June 2018].

Orellana, M. V., Matrai, P. A., Leck, C., Rauschenberg, C. D., Lee, A. M., & Coz, E. (2011). Marine microgels as a source of cloud condensation nuclei in the high Arctic*. Proceedings of the National Academy of Sciences, 108(33),* 13612-13617.

Ovchinnikov, M., Korolev, A., & Fan, J. (2011). Effects of ice number concentration on dynamics of a shallow mixed

Palm, S. P., Strey, S. T., Spinhirne, J., & Markus, T. (2010). Influence of Arctic sea ice extent on polar cloud fraction and vertical structure and implications for regional climate. *Journal of Geophysical Research: Atmospheres* (1984-2012), 115(D21).

Petch, J. C., P. N. Blossey, and C. S. Bretherton (2008), Differences in the lower troposphere in two- and three-dimensional cloud-resolving model simulations of deep convection*,* Q. J. R. Meteorol. Soc., 134(636), 1941–1946.

Petters, J. L., Harrington, J. Y., & Clothiaux, E. E. (2012). Radiative-dynamical Feedbacks in Low Liquid Water Path Stratiform Clouds. *Journal of the Atmospheric Sciences*, 69(5), 1498-1512.

Pithan, F. and Mauritsen, T., 2014. Arctic amplification dominated by temperature feedbacks in contemporary climate models. *Nature Geoscience*, *7*(3), p.181.

Plevin, T. D, (2013), Large eddy simulations of Arctic stratus clouds', Doctor of Philosophy, Leeds University, Leeds U.K..

Pruppacher, H.R. & Klett, J.D. (1997). Microphysics of Clouds and Precipitation.

Raes, F., Van Dingenen, R., Vignati, E., Wilson, J., Putaud, J.P., Seinfeld, J.H. & Adams, P. (2000). Formation and cycling of aerosols in the global troposphere. Atmospheric Environment, 34, 4215{4240. 9, 80

Richter-Menge, J., J. E. Overland, J. T. Mathis, and E. Osborne, Eds., (2017) Arctic Report Card 2017 [ONLINE],Available at: http://www.arctic.noaa.gov/Report-Card. [Accessed 8 June 2018]

Rogers, D. P., and L. M. Olsen, (1990) The diurnal variability of marine stratocumulus clouds. *Conf. Cloud Physics, San Francisco, CA, Amer. Meteor. Soc.*, J51-J55.

Sandu, Irina, Jean-Louis Brenguier, Olivier Geoffroy, Odile Thouron, Valery Masson, (2008) Aerosol Impacts on the Diurnal Cycle of Marine Stratocumulus. J. Atmos. Sci., 65, 2705-2718.

Savre, J., Ekman, A.M., Svensson, G. and Tjernström, M., 2015. Large-eddy simulations of an Arctic mixed-phase stratiform cloud observed during ISDAC: sensitivity to moisture aloft, surface fluxes and large-scale forcing. *Quarterly Journal of the Royal Meteorological Society*, *141*(689), pp.1177-1190.

Schuur, E.A., McGuire, A.D., Schädel, C., Grosse, G., Harden, J.W., Hayes, D.J., Hugelius, G., Koven, C.D., Kuhry, P., Lawrence, D.M. and Natali, S.M., 2015. Climate change and the permafrost carbon feedback. *Nature*, *520*(7546), p.171.

Screen, J. A., & Simmonds, I. (2010). The central role of diminishing sea ice in recent Arctic temperature amplification. *Nature, 464(7293),* 1334-1337.

Sedlar, J., & Shupe, M. D. (2014). Characteristic nature of vertical motions observed in Arctic mixed-phase stratocumulus. Atmospheric Chemistry and Physics, 14, 3461–3478. https://doi.org/10.5194/acp-14-3461-2014

Sedlar, J., & Tjernström, M. (2009). Stratiform cloud—Inversion characterization during the Arctic melt season. *Boundary-layer meteorology*, *132*(3), 455-474.

Sedlar, J., 2014. Implications of limited liquid water path on static mixing within Arctic low-level clouds. *Journal of Applied Meteorology and Climatology*, *53*(12), pp.2775-2789.

Sedlar, J., Shupe, M. D., & Tjernström, M. (2012). On the relationship between thermodynamic structure and cloud top, and its climate significance in the Arctic. *Journal of Climate*, *25*(7), 2374-2393.

Sedlar, J., Tjernström, M., Mauritsen, T., Shupe, M. D., Brooks, I. M., Persson, P. O. G., ... & Nicolaus, M. (2011). A transitioning Arctic surface energy budget: the impacts of solar zenith angle, surface albedo and cloud radiative forcing. *Climate dynamics*, 37(7-8), 1643-1660.

Serreze, M. C., & Stroeve, J. (2015). Arctic sea ice trends, variability and implications for seasonal ice forecasting. *Phil. Trans. R. Soc. A*, *373*(2045), 20140159.

Serreze, M.C. and Francis, J.A., 2006. The Arctic amplification debate. *Climatic change*, *76*(3-4), pp.241-264.

Shupe, M. D (2007).: A ground-based multiple remote-sensor cloud phase classifier, Geophys. Res. Lett., 34, L2209,doi:10.1029/2007GL031008,

Shupe, M. D. (2007). A ground-based multiple remote-sensor cloud phase classifier. Geophysical Research Letters, 34, L22809. https://doi.org/10.1029/2007GL031008

Shupe, M. D., & Intrieri, J. M. (2004). Cloud radiative forcing of the Arctic surface: The influence of cloud properties, surface albedo, and solar zenith angle. Journal of Climate, 17, 616–628. https://doi.org/10.1175/1520-0442(2004)017<0616:CRFOTA>2.0.CO;2

Shupe, M. D., Brooks, I. M., & Canut, G. (2012). Evaluation of turbulent dissipation rate retrievals from Doppler cloud radar. Atmospheric Measurement Techniques, 5, 1375–1385. https://doi.org/10.5194/amt-5-1375-2012

Shupe, M. D., Kollias, P., Persson, P. O. G., and McFarquhar, G.M. (2008): Vertical motions in Arctic mixed-phase stratiform clouds, J.Atmos. Sci., 65, 1304–1322

Shupe, M. D., Persson, P. O. G., Brooks, I. M., Tjernström, M., Sedlar, J., Mauritsen, T.,…Sjogren, S. (2013). Cloud and boundary layer interactions over the Arctic sea-ice in late summer. Atmospheric Chemistry and Physics, 13, 9379–9400. https://doi.org/10.5194/acp-13-9379-2013

Slingo, A., Brown, R. and Wrench, C. L. (1982), A field study of nocturnal stratocumulus; III. High resolution radiative and microphysical observations. *Q.J.R. Meteorol. Soc*., 108: 145-165.

Solomon, A., Shupe, M. D., Persson, P. O. G., & Morrison, H. (2011). Moisture and dynamical interactions maintaining decoupled Arctic mixed-phase stratocumulus in the presence of a humidity inversion. *Atmospheric Chemistry and Physics*, 11(19), 10127-10148.

Solomon, A., Shupe, M.D., Persson, O., Morrison, H., Yamaguchi, T., Caldwell, P.M. and de Boer, G., (2014). The sensitivity of springtime Arctic mixed-phase stratocumulus clouds to surface-layer and cloud-top inversion-layer moisture sources. *Journal of the Atmospheric Sciences*, *71*(2), pp.574-595.

Sotiropoulou, G., Sedlar, J., Tjernström, M., Shupe, M. D., Brooks, I. M., and Persson, P. O. G.(2014) The thermodynamic structure of summer Arctic stratocumulus and the dynamic coupling to the surface, *Atmos. Chem. Phys*., 14, 12573–12592, doi:10.5194/acp-14-12573-2014,

Stephens, G.L., (1978). Radiation profiles in extended water clouds. I: Theory. *Journal of the Atmospheric Sciences*, *35*(11), pp.2111-2122.

Stirling, A. J., & Stratton, R. A. (2012). Entrainment processes in the diurnal cycle of deep convection over land. *Quarterly Journal of the Royal Meteorological Society*, *138*(666), 1135

Stroeve, J., M. M. Holland, W. Meier, T. Scambos, and M. Serreze (2007), Arctic sea ice decline: Faster than forecast, *Geophys. Res. Lett., 34*

Stull, R.B., 1988. *An Introduction to Boundary Layer Meteorology* (Vol. 13). Springer Science & Business Media.

Tjernström, M., Balsley, B. B., Svensson, G., & Nappo, C. J. (2009). The effects of critical layers on residual layer turbulence. Journal of the Atmospheric Sciences, 66, 468–480. https://doi.org/10.1175/2008JAS2729.1

Tjernström, M., Birch, C. E., Brooks, I. M., Shupe, M. D., Persson, P. O. G., Sedlar, J., Mauritsen, T., Leck, C., Paatero, J., Szczodrak, M., and Wheeler, C. R.(2012) Meteorological conditions in the central Arctic summer during the Arctic Summer Cloud Ocean Study (ASCOS), Atmos. Chem. Phys., 12, 6863-6889

Tjernström, M., Leck, C., Birch, C. E., Bottenheim, J. W., Brooks, B. J., Brooks, I. M., … Wheeler, C. R. (2014). The Arctic Summer Cloud-Ocean Study (ASCOS): Overview and experimental design. Atmospheric Chemistry and Physics, 14, 2823–2869. ttps://doi.org/10.5194/acp-14-2823-2014

Tjernström, M., Sedlar, J., & Shupe, M. D. (2008). How well do regional climate models reproduce radiation and clouds in the Arctic? An evaluation of ARCMIP simulations. *Journal of Applied Meteorology and Climatology*, *47*(9), 2405-2422.

Tjernström, Michael, (2007) Is There a Diurnal Cycle in the Summer Cloud-Capped Arctic Boundary Layer?. *J. Atmos. Sci*., 64, 3970-3986.

Tjernström, Michael, Joseph Sedlar, Matthew D. Shupe, (2008) How Well Do Regional Climate Models Reproduce Radiation and Clouds in the Arctic? An Evaluation of ARCMIP Simulations. *J. Appl. Meteor. Climatol*., 47, 2405-2422.

Turton, J. D., & Nicholls, S. (1987). A study of the diurnal variation of stratocumulus using a multiple mixed layer model. *Quarterly Journal of the Royal Meteorological Society*, 113(477), 969-1009.

Twomey, S. A. (1977) The influence of pollution on the shortwave albedo of clouds, J. Atmos. Sci., 34, 1149-1152.

Vavrus, S. (2004). The impact of cloud feedbacks on Arctic climate under greenhouse forcing. *Journal of Climate*, *17*(3), 603-615.

Wang, M., and J. E. Overland (2009), A sea ice free summer Arctic within 30 years?, *Geophys. Res. Lett.*, *36*, L07502, doi:10.1029/2009GL037820.

Westwater, E. R., Han, Y., Shupe, M. D., & Matrosov, S. Y. (2001). Analysis of integrated cloud liquid and precipitable water vapor retrievals from microwave radiometers during the Surface Heat Budget of the Arctic Ocean project. Journal of Geophysical Research, 106, 32,019–32,030.https://doi.org/10.1029/2000JD000055

Wood, R. and D. L. Hartmann, 2006: Spatial variability of liquid water path in marine boundary layer clouds: The importance of mesoscale cellular convection. J. Climate, 19, 1748–1764.

Zhang, W., Miller, P. A., Smith, B., Wania, R., Koenigk, T., & Döscher, R. (2013). Tundra shrubification and tree-line advance amplify arctic climate warming: results from an individual-based dynamic vegetation model. *Environmental Research Letters*, *8*(3), 034023.